

Modeling and Analysis of Off-Road Tire Cornering Characteristics

by

Fatemeh Gheshlaghi

A thesis submitted to the
School of Graduate and Postdoctoral Studies in partial
fulfillment of the requirements for the degree of

Master of Applied Science in Mechanical Engineering

Faculty of Engineering and Applied Science
University of Ontario Institute of Technology (Ontario Tech University)
Oshawa, Ontario, Canada
May 2022

© Fatemeh Gheshlaghi, 2022

THESIS EXAMINATION INFORMATION

Submitted by: **Fatemeh Gheshlaghi**

Master of Applied Science in Mechanical Engineering

Thesis title: Modeling and Analysis of Off-Road Tire Cornering Characteristics

An oral defense of this thesis took place on April 28, 2022 in front of the following examining committee:

Examining Committee:

Chair of Examining Committee Dr. Martin Agelin-Chaab

Research Supervisor Dr. Moustafa El-Gindy

Research Co-supervisor Dr. Subhash Rakheja

Examining Committee Member Dr. Zeinab El-Sayegh

Thesis Examiner Dr. Jaho Seo

The above committee determined that the thesis is acceptable in form and content and that a satisfactory knowledge of the field covered by the thesis was demonstrated by the candidate during an oral examination. A signed copy of the Certificate of Approval is available from the School of Graduate and Postdoctoral Studies.

ABSTRACT

Cornering performance characteristics of wheeled vehicles substantially rely on the forces/moment generated from interactions between pneumatic tires and terrains. Accurate models are thus required to predict these forces/moment to be employed in vehicle simulations for development and design. The goal of this dissertation research is to provide a virtual testing environment in Pam-Crash software as an alternative to actual tests for Finite Element Analysis (FEA) and Smoothed Particle Hydrodynamics (SPH) analysis of rolling tire interactions on deformable terrains. SPH method and hydrodynamics-elastic plastic material were used to simulate different soil types that are often utilized in vehicle-terrain interactions. Two pressure-sinkage and shear-strength experiments were used to calibrate the terrains. The simulation findings were compared with the measured data that showed good agreements.

Furthermore, a detailed analysis of the rolling resistance coefficient and cornering properties of the tire over various terrains is presented, as well as the development of Genetic Algorithms (GA) to determine the mathematical relations for the cornering force, self-aligning moment, and overturning moment as functions of important operating factors. Cornering tests were performed for the RHD tire operating over the mud soil to examine the validity of the GA-based cornering force, self-aligning moment, and overturning moment relationships. It was concluded that the identified mathematical relations could provide very good estimations of the cornering characteristics under a broad range of operating conditions and soils.

Keywords: Tire modeling; Terrain calibration; Tire-terrain interaction; Smoothed-Particle Hydrodynamics; Finite Element Analysis; Cornering Characteristics; Rolling resistance

AUTHOR'S DECLARATION

I hereby declare that this thesis consists of original work of which I have authored. This is a true copy of the thesis, including any required final revisions, as accepted by my examiners.

I authorize the University of Ontario Institute of Technology to lend this thesis to other institutions or individuals for the purpose of scholarly research. I further authorize the University of Ontario Institute of Technology to reproduce this thesis by photocopying or by other means, in total or in part, at the request of other institutions or individuals for the purpose of scholarly research. I understand that my thesis will be made electronically available to the public.

FATEMEH GHESHLAGHI

STATEMENT OF CONTRIBUTIONS

Part of the work described in Chapter 2 will be submitted as:

Gheshlaghi, F., Rakheja, S., El-Gindy, M., "Tire-Terrain Interaction Modeling and Analysis: Literature Survey" Int. J. Vehicle Systems Modelling and Testing, (To be submitted).

Part of the work described in Chapter 3 has been published as:

Gheshlaghi F., El-Sayegh Z., El- Gindy M et al. 'Prediction and validation of terramechanics models for estimation of tire rolling resistance coefficient". Int. J. Vehicle Systems Modelling and Testing, 14, no. 3-4 (2020) 1-12.

Part of the work described in Chapter 4 has been published as:

Gheshlaghi, F., El-Sayegh, Z., El-Gindy, M., Oijer, F. et al., "Advanced Analytical Truck Tires-Terrain Interaction Model," SAE Technical Paper No. 2021-01-0329, April 13- 15, Detroit Michigan, USA, (2021), <https://doi.org/10.4271/2021-01-0329>.

Part of the work described in Chapters 5 and 6 has been published as:

Gheshlaghi, F., El-Sayegh, Z., El-Gindy, M., Oijer, F. et al., "Advanced Analytical Truck Tires-Terrain Interaction Model," SAE Technical Paper No. 2021-01-0329, April 13- 15, Detroit Michigan, USA, (2021), <https://doi.org/10.4271/2021-01-0329>.

Gheshlaghi, F., El-Sayegh, Z., El-Gindy, M., Oijer, F. et al., "Analysis of off-road tire cornering characteristics using advanced analytical techniques" Tire Society Journal, Oct 2021, USA, (Under review).

CONTENTS

ABSTRACT	ii
AUTHOR'S DECLARATION	iii
STATEMENT OF CONTRIBUTIONS	iv
CONTENTS	v
LIST OF FIGURES	ix
LIST OF TABLES	xvi
NOMENCLATURE.....	xvii
ACKNOWLEDGEMENTS	xix
CHAPTER 1 MOTIVATION AND OBJECTIVES.....	1
1.1 MOTIVATION	1
1.2 OBJECTIVES AND SCOPE	2
1.3 OUTLINE OF THESIS	3
CHAPTER 2 LITERATURE REVIEW.....	5
2.1 Tire modeling	6
2.1.1 FEA tire modeling.....	9
2.2 Tire model validations.....	14
2.2.1 Multi-axis stiffness tests	14
2.2.2 Dynamic validation tests.....	20
Drum-cleat test.....	21
Yaw Oscillation test:.....	22
Cornering test.....	23
2.3 Terrain modeling methods	24
2.4 Terrain models calibrations	29
2.4.1 Soil penetration tests	29

2.4.2	Pressure-sinkage tests.....	31
2.4.3	Shear strength test	32
2.5	Tire-terrain interaction modeling	33
2.5.1	Rolling resistance analysis.....	33
2.5.2	Cornering characteristic analysis	36
2.5.3	Soil behavior analysis	38
2.6	Summary	40
CHAPTER 3	TIRE MODELING AND MODEL VALIDATIONS	42
3.1	Tire model validations.....	45
3.1.1	Vertical stiffness test.....	45
3.1.2	Footprint test	47
3.1.3	Drum-cleat test.....	49
3.2	Summary	52
CHAPTER 4	SOIL MODELING.....	54
4.1	Experimental characterization of a clay loam soil	54
4.2	SPH soil modeling.....	56
4.3	SPH sensitivity analysis	57
	Displacement speed in the shear-strength test.....	57
	Equation of state coefficients	59
	Yield stress	60
	Tangent modulus	61
4.4	SPH soil model calibrations	62
4.4.1	Pressure-sinkage test	63
4.4.2	Shear strength test	64
4.5	Soil model characteristics.....	66

4.6	Summary	69
-----	---------------	----

CHAPTER 5 TIRE-TERRAIN INTERACTIONS ANALYSIS: ROLLING RESISTANCE70

5.1	Introduction	70
5.2	Simulation model setup for tire rolling resistance analyses	71
5.3	Rolling resistance analyses.....	74
5.3.1	Effect of vertical load.....	75
5.3.2	Effect of inflation pressure.....	76
5.3.3	Effect of soil compaction	80
5.3.4	Effect of speed	81
5.4	The development of rolling resistance relationship using genetic algorithm....	82
5.5	Summary	87

CHAPTER 6 TIRE-TERRAIN INTERACTIONS ANALYSIS: CORNERING CHARACTERISTICS.....89

6.1	Introduction	89
6.2	Simulation model setup.....	90
6.3	Cornering characteristics analyses	92
6.3.1	Effect of side-slip angle	92
6.3.2	Effect of vertical load.....	97
6.3.3	Effect of inflation pressure.....	102
6.3.4	Effect of rolling speed.....	107
6.3.5	Effect of soil internal friction angle	111
6.3.6	Effect of soil compaction	115
6.4	The development and validation of cornering characteristics relationships using genetic algorithm.....	119
6.5	Summary	123

CHAPTER 7: MAJOR CONCLUSIONS AND CONTRIBUTIONS	125
7.1 Major contributions of the thesis.....	125
7.2 Major conclusions	125
7.3 Future works.....	128
7.4 Publications	129
REFERENCES.....	130

LIST OF FIGURES

FIGURE 2.1. DYNAMICS TIRE MODELS	7
FIGURE 2.2. RIGID RING TIRE MODEL [SCHMEITZ, 2004]	8
FIGURE 2.3. TIRE MODEL WITH CONSTANT SHEAR STRESS IN RIM CONTACT REGION [ZHANG ET AL., 2001].....	10
FIGURE 2.4. TIRE COMPONENTS [ZHANG ET AL., 2001]	11
FIGURE 2.5. (A) CONSTITUENTS OF 295/75R22.5 TRUCK TIRE (GOODYEAR.COM); AND (B) FEA TRUCK TIRE MODEL [CHAE, 2006]	12
FIGURE 2.6. THE FEA MODEL OF AN AGRICULTURAL VEHICLE TIRE [EL-SAYEGH ET AL., 2019].....	13
FIGURE 2.7. FEA MODEL OF A HIGH-LUG FARM SERVICE VEHICLE TIRE [XU ET AL., 2020]	14
FIGURE 2.8. TIRE VERTICAL STIFFNESS TESTING MACHINE [JAFARI, 2018].	16
FIGURE 2.9. FEA HLFS TIRE SIZE 220/80-B16 VERTICAL STIFFNESS TEST [EL-SAYEGH ET AL., 2019].....	16
FIGURE 2.10. COMPARISONS OF VERTICAL FORCE-DEFLECTION CHARACTERISTICS OBTAINED FROM THE FEA MODEL OF A HLFS TIRE WITH THE MEASURED DATA [EL-SAYEGH ET AL., 2019].....	17
FIGURE 2.11. MEASURED TRUCK TIRE FOOTPRINT UNDER DIFFERENT VERTICAL LOADS AND INFLATION PRESSURES [XIONG ET AL., 2015]..	18
FIGURE 2.12. COMPARISON OF CONTACT AREA RESPONSES OF A HLFS TIRE MODEL WITH THE MEASURED DATA UNDER DIFFERENT TIRE LOADS [GHESHLAGHI, 2020]	19
FIGURE 2.13. LONGITUDINAL DISPLACEMENT ON FEA HLFS TIRE AT 1.5 KN AND 193 KPA (28PSI) INFLATION PRESSURE [EL-SAYEGH ET AL., 2019]	20
FIGURE 2.14. THE VERTICAL FIRST MODE OF VIBRATION OF FEA WIDE-BASED TIRE AT 45.4 KN VERTICAL LOAD AND 827 KPA (120 PSI) INFLATION PRESSURE [MARJANI, 2016]	22
FIGURE 2.15. (A) YAW OSCILLATION TESTING MACHINE; AND (B) FEA YAW OSCILLATION TEST MODEL [CHE, 2006].....	23
FIGURE 2.16. CORNERING FORCE VALIDATION USING EXPERIMENTAL DATA [CHAE, 2006]	24
FIGURE 2.17. SELF-ALIGNING MOMENT VALIDATION USING EXPERIMENTAL DATA [CHAE, 2006]	24
FIGURE 2.18. PARTICLE INTERPOLATION UTILIZING PARTICLES INSIDE THE SMOOTHING FUNCTIONS DOMAIN [BUI ET AL., 2007]	27
FIGURE 2.19. BEVAMETER SCHEMATIC [WONG, 2008]	31
FIGURE 2.20. THE FEA PRESSURE-SINKAGE TEST FOR 17% MOIST CLAY LOAM SOIL [GHESHLAGHI AND MARDANI, 2020].....	32
FIGURE 2.21. THE FEA SHEAR-STRENGTH TEST FOR 17% MOIST CLAY LOAM SOIL; AND [GHESHLAGHI AND MARDANI, 2020].....	33

FIGURE 2.22. (A) VERTICAL, (B) LONGITUDINAL, AND (C) TRANSVERSE CONTACT STRESS DISTRIBUTION OF A FREE-ROLLING TIRE WITH A 32.5 KN LOAD [GUO ET AL., 2020]	39
FIGURE 2.23. TERRAIN MAPPING DURING THE MULTI-PASS SIMULATION OF A DRIVEN TIRE (A) SOIL CONSECUTIVE LOADING-UNLOADING (B) CONTOUR OF TERRAIN SINKAGE [SANDU ET AL., 2019].....	40
FIGURE 3.1. FEA TIRE BASIC DIMENSIONS [CHAE, 2006].....	43
FIGURE 3.2. RHD TIRE SECTION [SLADE, 2009]	44
FIGURE 3.3. THE RAMP VERTICAL LOAD APPLIED TO THE RIM OF THE TIRE MODEL	46
FIGURE 3.4. VERTICAL STIFFNESS SIMULATION TEST OF THE TIRE MODEL	46
FIGURE 3.5. LOAD-DEFLECTION RESPONSES OF THE RHD TRUCK TIRE MODEL UNDER DIFFERENT INFLATION PRESSURES	47
FIGURE 3.6. VON MISES STRESS DISTRIBUTION OVER THE CONTACT AREA OF THE TIRE MODEL (40 KN VERTICAL LOAD AND 758 KPA (110 PSI) INFLATION PRESSURE)	48
FIGURE 3.7. COMPARISON OF CONTACT AREAS OBTAINED FROM THE TIRE MODEL WITH THOSE REPORTED FOR THE GOODYEAR TIRE (CHAE, 2006) FOR DIFFERENT VERTICAL LOADS (INFLATION PRESSURE:758 KPA (110 PSI)).....	49
FIGURE 3.8. FEA RHD TRUCK TIRE MODEL UNDER THE DRUM-CLEAT TEST	50
FIGURE 3.9. FREQUENCY SPECTRUM OF VERTICAL AND LONGITUDINAL FREE VIBRATION OF THE TIRE MODEL OBTAINED FROM THE DRUM-CLEAT TEST (TIRE LOAD: 40 KN; INFLATION PRESSURE: 586 KPA (85 PSI))	51
FIGURE 3.10. FREQUENCY SPECTRUM OF VERTICAL AND LONGITUDINAL FREE VIBRATION OF THE TIRE MODEL OBTAINED FROM THE DRUM-CLEAT TEST (TIRE LOAD: 40 KN; INFLATION PRESSURE: 758 KPA (110 PSI))	52
FIGURE 3.11. FREQUENCY SPECTRUM OF VERTICAL AND LONGITUDINAL FREE VIBRATION OF THE TIRE MODEL OBTAINED FROM THE DRUM-CLEAT TEST (TIRE LOAD: 40 KN; INFLATION PRESSURE: 896 KPA (130 PSI))	52
FIGURE 4.1. PLATE PENETRATION TESTER AND SHEAR TEST BOX USED FOR THE MEASUREMENT OF SOIL	56
FIGURE 4.2. CONVERTING FEA ELEMENTS TO SPH PARTICLES	57
FIGURE 4.3. SPH SOIL SHEAR-STRENGTH AT DIFFERENT SPEEDS VERSUS MEASUREMENTS FOR CLAY LOAM SOIL	58
FIGURE 4.4. SPH SOIL PRESSURE-SINKAGE AT DIFFERENT C ₁ COEFFICIENTS VERSUS MEASUREMENTS FOR CLAY LOAM SOIL	59
FIGURE 4.5. SPH SOIL SHEAR-STRENGTH AT DIFFERENT SPEEDS VERSUS MEASUREMENTS FOR CLAY LOAM SOIL.....	60

FIGURE 4.6. SPH SOIL PRESSURE-SINKAGE AT DIFFERENT YIELD STRESSES VERSUS MEASUREMENTS FOR CLAY LOAM SOIL	61
FIGURE 4.7. SPH SOIL SHEAR-STRENGTH AT DIFFERENT TANGENT MODULI VERSUS MEASUREMENTS FOR CLAY LOAM SOIL	62
FIGURE 4.8. SPH SOIL PRESSURE-SINKAGE TEST.....	63
FIGURE 4.9. SPH SOIL PRESSURE-SINKAGE VERSUS MEASUREMENTS FOR CLAY LOAM SOIL	64
FIGURE 4.10. SPH SOIL SHEAR STRENGTH TEST	65
FIGURE 4.11. SPH SOIL SHEAR-STRENGTH TEST VERSUS MEASUREMENTS FOR THE CLAY LOAM SOIL	66
FIGURE 4.12. SIMULATED PRESSURE-SINKAGE TESTS FOR DIFFERENT SOILS	68
FIGURE 5.1. SCHEMATIC OF THE VOLVO F-SERIES MEDIUM 8*4 TRUCK	71
FIGURE 5.2. MODEL USED TO SIMULATE TIRE'S INTERACTIONS WITH A SOFT SOIL (CLAY LOAM).....	73
FIGURE 5.3. MULTI-PASS TIRE-TERRAIN INTERACTION MODEL CONSIDERING THE FOUR TIRES OF A SINGLE VEHICLE TRACK	73
FIGURE 5.4. INFLUENCE OF VERTICAL LOAD ON ROLLING RESISTANCE COEFFICIENT OF THE TIRE ROLLING FREELY ON DIFFERENT SOILS: (A) CLAY LOAM; (B) DENSE SAND; AND (C) CLAYEY SOIL (FORWARD SPEED = 10KM/H)	76
FIGURE 5.5. EFFECT OF INFLATION PRESSURE ON ROLLING RESISTANCE COEFFICIENT OF A DRIVEN TIRE SUBJECT TO DIFFERENT DRIVE TORQUES OVER THE CLAY LOAM SOIL (FORWARD SPEED: 10 KM/H; WHEEL LOAD: 40 KN).	78
FIGURE 5.6. INFLUENCE OF INFLATION PRESSURE ON ROLLING RESISTANCE COEFFICIENT OF THE TIRE ROLLING FREELY ON DIFFERENT SOILS: (A) CLAY LOAM; (B) DENSE SAND; AND (C) CLAYEY SOIL (FORWARD SPEED = 10KM/H)	79
FIGURE 5.7. ROLLING RESISTANCE COEFFICIENT AS A FUNCTION OF SOIL DEPTH AT DIFFERENT SOILS.....	81
FIGURE 5.8. EFFECT OF FORWARD SPEED ON THE ROLLING RESISTANCE COEFFICIENT OF THE TIRE OPERATING ON THE CLAY SOIL FOR DIFFERENT VERTICAL LOADS (INFLATION PRESSURE: 758KPA (110 PSI))	82
FIGURE 5.9. THE FLOWCHART OF THE PROPOSED GENETIC ALGORITHM [ABE, 2004]	84
FIGURE 5.10. PREDICTED VERSUS SIMULATED ROLLING RESISTANCE COEFFICIENT	87
FIGURE 6.1. TIRE-TERRAIN INTERACTION MODEL CONSIDERING SIDE-SLIP OF TIRES OF A FOUR-AXLE TRUCK	91
FIGURE 6.2. FORCES AND MOMENTS ACTING ON A STEERED TIRE	91

FIGURE 6.3. SELF-ALIGNING MOMENT AS A FUNCTION OF SIDE-SLIP ANGLE FOR THE FREE-ROLLING TIRES OVER THE SANDY LOAM AT DIFFERENT AXLES (SPEED:15 KM/H; INFLATION PRESSURE: 758 KPA (110 PSI) ; VERTICAL LOAD: 40 KN)	93
FIGURE 6.4. CORNERING FORCE AS A FUNCTION OF SIDE-SLIP ANGLE FOR THE FREE-ROLLING TIRES OVER THE SANDY LOAM AT DIFFERENT AXLES (SPEED:15 KM/H; INFLATION PRESSURE: 758 KPA (110 PSI); VERTICAL LOAD: 40 KN)	94
FIGURE 6.5. SELF-ALIGNING MOMENT AS A FUNCTION OF SIDE-SLIP ANGLE FOR THE DRIVEN TIRES OVER THE SANDY LOAM AT DIFFERENT AXLES (SPEED:15 KM/H; INFLATION PRESSURE: 758 KPA (110 PSI); VERTICAL LOAD: 40 KN)	95
FIGURE 6.6. CORNERING FORCE AS A FUNCTION OF SIDE-SLIP ANGLE FOR THE DRIVEN TIRES OVER THE SANDY LOAM AT DIFFERENT AXLES (SPEED:15 KM/H; INFLATION PRESSURE: 758 KPA (110 PSI); VERTICAL LOAD: 40 KN)	96
FIGURE 6.7. OVERTURNING MOMENT AS A FUNCTION OF SIDE-SLIP ANGLE FOR THE FREE-ROLLING TIRES OVER THE SANDY LOAM AT DIFFERENT AXLES (SPEED:15 KM/H; INFLATION PRESSURE: 758 KPA (110 PSI); VERTICAL LOAD: 40 KN)	97
FIGURE 6.8. INFLUENCE OF VERTICAL WHEEL LOAD ON THE SELF-ALIGNING MOMENT OF THE FREE-ROLLING TIRE OPERATING ON 25% MOIST SANDY SOIL FOR DIFFERENT INFLATION PRESSURES (SLIP ANGLE: 6 DEG; SPEED: 15 KM/H).....	98
FIGURE 6.9. INFLUENCE OF VERTICAL WHEEL LOAD ON THE CORNERING FORCE OF THE FREE-ROLLING TIRE OPERATING ON 25% MOIST SANDY SOIL FOR DIFFERENT INFLATION PRESSURES (SLIP ANGLE: 6 DEG; SPEED: 15 KM/H)	99
FIGURE 6.10. INFLUENCE OF VERTICAL WHEEL LOAD ON THE SELF-ALIGNING MOMENT OF THE DRIVEN TIRE OPERATING ON 25% MOIST SANDY SOIL FOR DIFFERENT INFLATION PRESSURES (SLIP ANGLE: 6 DEG; SPEED: 15 KM/H)	100
FIGURE 6.11. INFLUENCE OF VERTICAL WHEEL LOAD ON THE CORNERING FORCE OF THE DRIVEN TIRE OPERATING ON 25% MOIST SANDY SOIL FOR DIFFERENT INFLATION PRESSURES (SLIP ANGLE: 6 DEG; SPEED: 15 KM/H)	101
FIGURE 6.12. INFLUENCE OF VERTICAL WHEEL LOAD ON THE OVERTURNING MOMENT OF THE FREE-ROLLING TIRE OPERATING ON 25% MOIST SANDY SOIL FOR DIFFERENT INFLATION PRESSURES (SLIP ANGLE: 6 DEG; SPEED: 15 KM/H).....	102
FIGURE 6.13. INFLUENCE OF INFLATION PRESSURE ON SELF-ALIGNING MOMENT OF THE TIRE ROLLING FREELY ON THE 25% MOIST SANDY	

SOIL FOR TWO DIFFERENT SLIP ANGLES (VERTICAL LOAD: 40 KN; SPEED: 15 KM/H)	103
FIGURE 6.14. INFLUENCE OF INFLATION PRESSURE ON CORNERING FORCE OF THE TIRE ROLLING FREELY ON THE 25% MOIST SANDY SOIL FOR TWO DIFFERENT SLIP ANGLES (VERTICAL LOAD: 40 KN; SPEED: 15 KM/H).....	104
FIGURE 6.15. INFLUENCE OF INFLATION PRESSURE ON SELF-ALIGNING MOMENT OF THE DRIVEN TIRE ON THE 25% MOIST SANDY SOIL FOR TWO DIFFERENT SLIP ANGLES (VERTICAL LOAD: 40 KN; SPEED: 15 KM/H).....	105
FIGURE 6.16. INFLUENCE OF INFLATION PRESSURE ON CORNERING FORCE OF THE DRIVEN TIRE ON THE 25% MOIST SANDY SOIL FOR TWO DIFFERENT SLIP ANGLES (VERTICAL LOAD: 40 KN; SPEED: 15 KM/H) 106	
FIGURE 6.17. INFLUENCE OF INFLATION PRESSURE ON OVERTURNING MOMENT OF THE TIRE ROLLING FREELY ON THE 25% MOIST SANDY SOIL FOR DIFFERENT SLIP ANGLES (VERTICAL LOAD: 40 KN; SPEED: 15 KM/H).....	106
FIGURE 6.18. INFLUENCE OF FORWARD SPEED ON THE SELF-ALIGNING MOMENT OF FREE-ROLLING TIRES OF THE FOUR-AXLE VEHICLE MODEL OPERATING ON THE DRY SANDY LOAM SOIL (SLIP ANGLE: 6 DEG; INFLATION PRESSURE: 758 KPA (110 PSI); VERTICAL LOAD: 40 KN	108
FIGURE 6.19. INFLUENCE OF FORWARD SPEED ON THE CORNERING FORCE OF FREE-ROLLING TIRES OF THE FOUR-AXLE VEHICLE MODEL OPERATING ON THE DRY SANDY LOAM SOIL (SLIP ANGLE: 6 DEG; INFLATION PRESSURE: 758 KPA (110 PSI); VERTICAL LOAD: 40 KN)....	108
FIGURE 6.20. INFLUENCE OF FORWARD SPEED ON THE OVERTURNING MOMENT OF FREE-ROLLING TIRES OF THE FOUR-AXLE VEHICLE MODEL OPERATING ON THE DRY SANDY LOAM SOIL (SLIP ANGLE: 6 DEG; INFLATION PRESSURE: 758 KPA (110 PSI); VERTICAL LOAD: 40 KN)	109
FIGURE 6.21. INFLUENCE OF FORWARD SPEED ON THE SELF-ALIGNING MOMENT OF DRIVEN TIRES OF THE FOUR-AXLE VEHICLE MODEL OPERATING ON THE DRY SANDY LOAM SOIL (SLIP ANGLE: 6 DEG; INFLATION PRESSURE: 758 KPA (110 PSI); VERTICAL LOAD: 40 KN)....	110
FIGURE 6.22. INFLUENCE OF FORWARD SPEED ON THE CORNERING FORCE OF DRIVEN TIRES OF THE FOUR-AXLE VEHICLE MODEL OPERATING ON THE DRY SANDY LOAM SOIL (SLIP ANGLE: 6 DEG; INFLATION PRESSURE: 758 KPA (110 PSI); VERTICAL LOAD: 40 KN)	111
FIGURE 6.23. INFLUENCE OF SOIL INTERNAL FRICTION ANGLE ON THE SELF-ALIGNING MOMENT DEVELOPED BY THE FREE-ROLLING TIRE FOR TWO DIFFERENT SLIP ANGLES (INFLATION PRESSURE: 758 KPA (110 PSI); VERTICAL LOAD: 40 KN; SPEED: 15 KM/H)	112

FIGURE 6.24. INFLUENCE OF SOIL INTERNAL FRICTION ANGLE ON THE CORNERING FORCE DEVELOPED BY THE FREE-ROLLING TIRE FOR TWO DIFFERENT SLIP ANGLES (INFLATION PRESSURE: 758 KPA (110 PSI); VERTICAL LOAD: 40 KN; SPEED: 15 KM/H).....	113
FIGURE 6.25. INFLUENCE OF SOIL INTERNAL FRICTION ANGLE ON THE OVERTURNING MOMENT DEVELOPED BY THE FREE-ROLLING TIRE FOR DIFFERENT SLIP ANGLES (INFLATION PRESSURE: 758 KPA (110 PSI); VERTICAL LOAD: 40 KN; SPEED: 15 KM/H).....	113
FIGURE 6.26. INFLUENCE OF SOIL INTERNAL FRICTION ANGLE ON THE SELF-ALIGNING MOMENT DEVELOPED BY THE DRIVEN TIRE FOR TWO DIFFERENT SLIP ANGLES (INFLATION PRESSURE: 758 KPA (110 PSI); VERTICAL LOAD: 40 KN; SPEED: 15 KM/H).....	114
FIGURE 6.27. INFLUENCE OF SOIL INTERNAL FRICTION ANGLE ON THE CORNERING FORCE DEVELOPED BY THE DRIVEN TIRE FOR TWO DIFFERENT SLIP ANGLES (INFLATION PRESSURE: 758 KPA (110 PSI); VERTICAL LOAD: 40 KN; SPEED: 15 KM/H).....	115
FIGURE 6.28. INFLUENCE OF SOIL SINKAGE ON THE SELF-ALIGNING MOMENT OF THE FREE-ROLLING TIRE OPERATING ON THE DRY SANDY LOAM SOIL AT 15 KM/H SPEED, 758 KPA (110 PSI) INFLATION PRESSURE, AND 40 KN VERTICAL LOAD	116
FIGURE 6.29. INFLUENCE OF SOIL SINKAGE ON THE SELF-ALIGNING MOMENT OF THE DRIVEN TIRE OPERATING ON THE DRY SANDY LOAM SOIL AT 15 KM/H SPEED, 758 KPA (110 PSI) INFLATION PRESSURE, AND 40 KN VERTICAL LOAD	116
FIGURE 6.30. INFLUENCE OF SOIL SINKAGE ON THE CORNERING FORCE OF THE FREE-ROLLING TIRE OPERATING ON THE DRY SANDY LOAM SOIL AT 15 KM/H SPEED, 758 KPA (110 PSI) INFLATION PRESSURE, AND 40 KN VERTICAL LOAD	117
FIGURE 6.31. INFLUENCE OF SOIL SINKAGE ON THE CORNERING FORCE OF THE DRIVEN TIRE OPERATING ON THE DRY SANDY LOAM SOIL AT 15 KM/H SPEED, 758 KPA (110 PSI) INFLATION PRESSURE, AND 40 KN VERTICAL LOAD	118
FIGURE 6.32. INFLUENCE OF SOIL SINKAGE ON THE OVERTURNING MOMENT OF THE FREE-ROLLING TIRE OPERATING ON THE DRY SANDY LOAM SOIL AT 15 KM/H SPEED, 758 KPA (110 PSI) INFLATION PRESSURE, AND 40 KN VERTICAL LOAD	118
FIGURE 6.33. CORRELATIONS OF THE CORNERING FORCE PREDICTED FROM THE IDENTIFIED MATHEMATICAL RELATIONS WITH THOSE PREDICTED FROM THE FE-SPH SIMULATION MODEL	122
FIGURE 6.34. CORRELATIONS OF THE SELF-ALIGNING MOMENT PREDICTED FROM THE IDENTIFIED MATHEMATICAL RELATIONS WITH THOSE PREDICTED FROM THE FE-SPH SIMULATION MODEL	123

FIGURE 6.35. CORRELATIONS OF THE OVERTURNING MOMENT PREDICTED
FROM THE IDENTIFIED MATHEMATICAL RELATIONS WITH THOSE
PREDICTED FROM THE FE-SPH SIMULATION MODEL 123

LIST OF TABLES

TABLE 3.1. RHD TIRE SPECIFICATIONS [CHAE, 2006]	43
TABLE 3.2. COMPARISONS OF MODEL-PREDICTED VERTICAL STIFFNESS OF THE TIRE MODEL WITH THE REPORTED DATA [HIROMA ET AL.,1997] FOR DIFFERENT INFLATION PRESSURES	47
TABLE 3.3. FUNDAMENTAL VERTICAL AND LONGITUDINAL MODE FREQUENCIES OF THE TIRE MODEL FOR DIFFERENT INFLATION PRESSURES (VERTICAL LOAD: 40KN)	52
TABLE 4.1. SHEAR-STRENGTH TEST PARAMETERS OF SPH SOILS AT DIFFERENT SPEEDS AND MEASUREMENTS	58
TABLE 4.2. MATERIAL PROPERTIES OF SPH SOILS [GHESHLAGHI ET AL., 2020; EL-SAYEGH, 2020].....	63
TABLE 4.3. PREDICTED AND MEASURED SHEAR PROPERTIES OF CLAY LOAM SOIL PARAMETERS	66
TABLE 4.4. MATERIAL PROPERTIES OF SPH MUD SOIL [COLLINGS ET AL., 2021]	68
TABLE 4.5. SIMULATED SOIL CHARACTERISTICS	68
TABLE 5.1. VEHICLE SPECIFICATIONS	72
TABLE 5.2. SENSITIVITY ANALYSIS OF GA EQUATION PARAMETERS ON THE ROLLING RESISTANCE COEFFICIENT	86
TABLE 6.1. SENSITIVITY ANALYSIS OF GA EQUATION PARAMETERS ON THE CORNERRING CHARACTERISTICS	121

NOMENCLATURE

Symbol	Parameter	Units
φ	Angle of internal shearing resistance	deg
E_t	Tangential modulus	MPa
τ_{max}	Maximum shear strength	MPa
τ	shear stress	MPa
b	Plate width	m
k_φ	Pressure-sinkage parameter	kN/m^{n+2}
k_c	Pressure-sinkage parameter	kN/m^{n+1}
ξ	Damping ratio	-
ω_y	Yaw oscillation frequency	Rad/s
G	Shear modulus of the terrain	MPa
P	Tire inflation pressure	kPa, Psi
k	Bulk modulus of the terrain	MPa
k_{cx}	Longitudinal tread stiffness	kN/m
k_f	Cornering stiffness	kN/rad
k_k	Longitudinal slip stiffness	KN/slip unit
k_l	Lateral slip stiffness	kN/m
k_M	Self-aligning moment stiffness	$kN.m/rad$
k_{tot}	Tire total vertical stiffness	kN/m
k_{vr}	Residual vertical stiffness	kN/m
m_a	Wheel rim mass	kg
m_b	Tire belt mass	kg
m_{tot}	Mass of the tire and rim ($m_a + m_b$)	kg
m_{tread}	Mass of the tread of the tire only	kg
M_x	Overturning moment	kN/m
M_y	Rolling resistance moment	kN/m
M_z	Vertical or aligning moment	kN/m
n	Exponent from terrain values	-
R	Radius of the inflated tire before loading	m
R_e	Effective rolling radius	m

R_{drum}	Drum radius	m
v, v_{tire}	Tire speed	m/s
v_{drum}	Drum speed	m/s
σ	Yield stress of the soil	MPa
z	Sinkage of disk in Bekker equation	m
α	Slip angle	rad
δ	Log decrement	-
γ	Amplitude ratio of the yaw oscillation output	-
θ_{ss}	Steady state angle value for rotation	rad
c	Cohesion constant of terrain	kPa
c_c	Critical damping constant	kNs/m
c_{vr}	Residual damping constant	kNs/m
d	Tire deflection due to loading	m
E	Youngs modulus of the terrain	MPa
f, RR	Rolling resistance coefficient	-
F_x	Longitudinal (tractive) force	kN
F_y	Lateral force	kN
F_z, F	Vertical force	kN
ρ	Density of terrain	Kg/m^3
ω	Wheel angular speed	Rad/s
h	Smoothing length	m
$C_i (i=0 \text{ to } 6)$	Material constants	-
μ	Density factor	-
n	Soil parameter	-

ACKNOWLEDGEMENTS

I would like to express my appreciation to my research supervisors, Dr. Moustafa El-Gindy and Dr. Subhash Rakheja, for their continuous guidance and valuable criticism throughout the course of my MSc. Their determination and passion for perfection always inspired me to work hard and I will be eternally grateful to them. I am also grateful to the financial support that provided to me during the course of my study from Dr. Subhash Rakheja of Concordia University. I extend thanks to Dr. El-Sayegh for providing me with requisite materials regarding my research.

I would also like to express my appreciation to NSERC Discovery Grant for their funding of this research work and allowing me to contribute to the state-of-the-art research for tire terrain interaction. I also wish to express my gratitude to Volvo Group Trucks Technology for providing me the opportunity to perform this research project and partially funding my research work.

I am extremely grateful to my parents and family for their endless support and abiding my ignorance during my abroad studies. Finally, I owe thanks to my dear husband, for his unconditional love, support and patience during my MSc studies.

CHAPTER 1

MOTIVATION AND OBJECTIVES

1.1 MOTIVATION

The tire is one of the most important components affecting nearly all aspects of vehicle dynamics. In particular, tire's cornering characteristics have a key role in determining vehicle handling, directional control and stability. Cornering force developed by a tire is related to many design and operating factors such as slip angle, inflation pressure, vertical load, speed, driving condition, tire construction, tread pattern and more, in a highly complex manner. Apart from these, the tire's interactions with deformable soils in an off-road environment constitutes another complexity. The cornering characteristics of an off-road tire thus also depend on soil-related factors such as cohesion, internal friction angle, and moisture content.

The cornering properties of tires have been widely investigated using phenomenological and semi-empirical models [Choi and GIM, 2000; Svendenius, J. and Gäfvert, M., 2004], which are mostly applicable to non-deformable terrains. A vast number of multi-layer structural models employing numerical approaches such as the Finite Element (FE) methods have also been developed for design and development of pneumatic tires [El-Sayegh et al., 2019; Marjani, 2016]. The cornering properties of tires operating on deformable terrains, however, have been investigated in relatively fewer studies. The soil models formulated based on pressure-sinkage and shear tests, are integrated to the FE tire models to evaluate their cornering properties [Tang et al., 2019]. Unlike the phenomenological models, these permit accurate modeling of tire-soil interactions with a focus on physical properties of both the pneumatic tire and the soil as deformable structures. The FE methods, however, have shown limitations for modeling soft soils, which are mostly due to the mesh-based nature of the FE method [Tagar et al., 2015; Carbonell et al., 2022]. Alternatively, mesh-less methods such as the Smoothed Particle Hydrodynamics (SPH) techniques have been used to overcome the mesh-related limitations of the FE methods [Gheshlaghi et al, 2020a; 2021; Lardner, 2017]. The mesh-less SPH methods can provide more realistic soil flow behavior than the traditional FE

methods, particularly when large deformations and fragmentations of soil materials are encountered [Niroumand et al., 2016]. The SPH methods could thus enable more realistic analyses of tires' interactions with deformable terrains and help limit the need for physical testing of the tires over different terrains. The SPH methods, however, have been implemented in a relatively fewer studies for investigating cornering properties of tires operating on soft soils. Moreover, these have been applied to a limited number of soil- and tire-design factors and operating conditions.

This study is primarily motivated to seek an efficient simulation method for accurate analysis of off-road tire cornering characteristics on deformable terrains considering important operation conditions. An off-road tire is modeled using the Finite Element Analysis (FEA) technique considering tire's interactions with deformable terrain and its validity is examined using the available measured data that were obtained from physical tests. Smoothed-Particle Hydrodynamic (SPH) technique is subsequently used to model different soils. The SPH models are calibrated for a number of soils, such as clay, moist sand, and sandy loam using the pressure-sinkage and shear stress data. A relatively large sample of terrains is considered to determine the mesh size, plot size and edge constraints to achieve improved simulation efficiency and convergence. The key motivation of the present study arises from the desire for a reliable tire cornering force model coupled with the SPH soil with reasonable computing demand for relatively higher speed operations in the off-road sectors.

1.2 OBJECTIVES AND SCOPE

The primary objective of the thesis research is to develop a simulation model for predicting cornering characteristics of off-road tires running over different types of deformable terrains. The specific goals of the study include:

- Develop a reliable tire cornering force model coupled with the SPH models of different soils such as such as clayey soil, dry sand, dense sand, moist sand, and sandy loam.
- Conduct soil models' calibrations and examine validity of the tire-soil models using the available measured data.

- Investigate influences of important operating parameters on the cornering properties of the tire.
- Develop novel relationships for predicting cornering characteristics tires under different soils and operating conditions for implementation in the full vehicle models using advanced algorithms involving testing, training and validations.

The development of a cornering force relationship with the operating conditions constitutes the novel goal of this study. These relations will permit simulations of directional analyses of full vehicle models coupled with deformable soils in a computationally efficient manner. The relationships are formulated considering different operating conditions, namely, speed, inflation pressure, traffic, drive torque, vertical load, longitudinal and lateral slip and steering angle in addition to the soil characteristics such as cohesion and angle of resistance. Such relations are intended for possible implementation in the Volvo Transportation Model (VTM) by replacing the rigid ring tire model.

1.3 OUTLINE OF THESIS

This dissertation is organized into 7 chapters describing the systematic developments in the simulation model, parametrization, validations and cornering force analyses. Chapter 2 presents a review of recent studies focused on off-road tire-terrain interactions. The reported studies are systematically grouped with regard to tire, terrain and tire-terrain interaction modeling techniques. Moreover, the studies reporting applications of tire-terrain interaction simulations for analyzing the rolling resistance, cornering characteristics, and soil behavior under different operating conditions are reviewed and discussed.

The FEA technique used for tire modeling is presented in Chapter 3 together with the validation techniques. The tire model validation techniques are further described in terms of the vertical stiffness, footprint and drum-cleat tests. The soil modeling and calibration methodologies are subsequently presented in Chapter 4. Pressure-sinkage and shear strength tests as calibration methods for the soil model are explained in details. The terrain calibration results are presented and compared with experimental and/or terramechanics data.

The rolling resistance coefficient of an off-road truck tire is evaluated in Chapter 5 considering different operating conditions. The simulation model for evaluating tire rolling resistance is presented and the simulation results are discussed to illustrate the effects of vertical load, inflation pressure, speed and terrain properties. The chapter further explores the relationship for the rolling resistance with the operating conditions using the genetic algorithm. The chapter presents the genetic algorithm modeling technique in addition to the development of the relationship for the rolling resistance coefficient. The validation process of the relationship derived using the GA algorithm for a different soil model is then described.

The cornering characteristics of off-road truck tires running over different terrains are analyzed in Chapter 6. After illustrating the simulation model for the tire cornering, the effects of different parameters such as vertical load, inflation pressure, speed, soil friction angle, soil cohesion and soil compaction on the cornering characteristics are discussed. The chapter further explores the relationship for the cornering characteristics with the operating conditions using the genetic algorithm. The chapter presents the genetic algorithm modeling technique in addition to the development of the relationship for the cornering force, self-aligning moment and overturning moment. The validation process of the relationship derived using the GA algorithm for a different soil model is then described.

The major conclusions of the research work along with major contributions are summarized in Chapter 7 together with some suggestions for further works.

CHAPTER 2

LITERATURE REVIEW

The study of tire-terrain interactions is vital for the design and performance analyses of off-road vehicles. The study of tire-ground interaction encompasses many complex challenges and it involves highly nonlinear dependence on a wide range of parameters such as soil compaction, soil stresses, traction, rolling resistance and cornering characteristics. The development of an accurate analysis method for tire-terrain interactions can facilitate understanding of the tire performance under different operating conditions and the design of a suitable powertrain for different terrain conditions.

The reported studies on wheel-soil interactions can be classified into three groups based on their methodology, namely, experimental, semi-analytical and analytical/numerical. Experimental methods are generally based on the dimensionless parameter of wheel number, which depends on the soil penetration resistance, vertical load and geometric features of the tire [Taheri et al., 2015]. The semi-analytical methods involve measurements of mechanical properties of soils such as cohesion and internal friction [Bekker, 1969]. Both, the experimental and semi-analytical methods, however, tend to oversimplify the dynamic interactions of the tire with the soils, and cannot accurately capture the tire performance with varying soil properties. The analytical or numerical methods such as finite element and discrete element methods can accurately simulate the tire-terrain interactions without relying on numerous simplifying assumptions, while considering impenetrability and dynamic traction conditions at the contact surface. These methods describe the tire as a flexible body using a finite strain hyperplastic material model.

In this chapter, the reported analyses methods are reviewed to gain essential knowledge and to formulate the scope of the thesis research. The study of tire-terrain interactions encompasses modeling of the tire and the soils, and models' refinements and validations. The reported studies are thus organized to describe these aspects systematically. Section 2.1 describes different methods of tire modeling, while section 2.2 reviews different techniques used for model validations. Terrain modeling and validation techniques are

reviewed in sections 2.3 and 2.4, respectively. Applications of analytical tire-terrain interaction models for analyzing rolling resistance, cornering characteristics, soil stress, and soil compaction under different operating conditions such as inflation pressure, vertical load, speed, multi-pass, and soil characteristics are presented in Section 2.5. A brief chapter summary is presented in section 2.6.

2.1 Tire modeling

Since the performance of a vehicle strongly relies on the forces and moments developed at the tire-terrain interface, several tire models have been developed for predicting tire forces /moments as functions of various design and operating parameters. The developments in advanced electronic stability and directional control systems, and autonomous vehicles have emphasized the need for more efficient and accurate tire models. Reported tire models range from physics-based simplistic models to highly complex finite element models capable of predicting tire behavior accurately. Tire models may be categorized into steady-state, transient, and dynamic models based on the rate of loading of the tire.

Steady-state tire models may yield considerable errors in the presence of transient loads such as those encountered during lane shift maneuvers on rough road surfaces or the oscillatory cycling effects of ABS braking and steering conditions [Lugner et al., 2005]. This is because the force generated in the tire contact area does not follow slip variations in real-time. The transient tire models can yield more accurate predictions of tire forces under transient maneuvers but are limited to lower frequencies [Lugner et al., 2005]. The dynamic tire models, on the other hand, incorporate the inertial effects under high-speed maneuvers. Figure 2.1 shows some of the reported lumped-parameter, semi-analytical, and finite element dynamic tire models [Wakui, 2011; Nakajima et al, 1986; Schmeitz, 2004]. The lumped parameter and semi-analytical tire models effectively reduce the complexity and the computational demand, while sacrificing the transient responses as well as local deformation characteristics. FEA models, on the other hand, can capture local transient responses accurately but impose substantial computational demand. The FE method enables considerations of the real tire profile together with components' material properties, thereby allowing for a considerably more accurate simulation of the tire transient response characteristics.

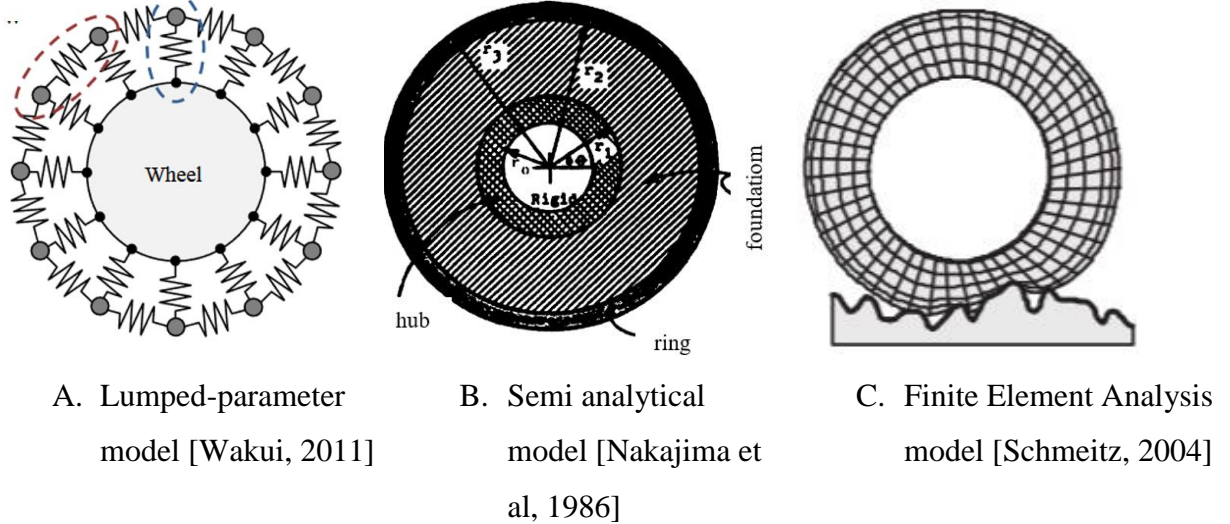


Figure 2.1. Dynamics tire models

Lumped parameter tire models such as rigid ring, flexible belt, and brush models have been widely used in vehicle dynamics simulations due to their simplistic formulations and superior computational efficiency. These models describe the global properties of a tire such as vertical stiffness, and cornering and braking force characteristics in the steady-state, under limited ranges of operating conditions. Moreover, such models cannot describe the highly complex mechanical behavior of the tire. As an example, Figure 2.2 illustrates a rigid band tire model, where the tread and the sidewalls are represented by uniformly distributed elastic or viscoelastic foundations [Schmeitz, 2004]. The tire belts are modeled as a ring that is coupled to the rim by a series of spring and damping elements. Rigid ring lumped parameter tire models were mainly used to investigate the tire belt vibrations. Taheri et al [2015] employed a lumped mass tire model to simulate the complex actions of tires on soft terrains. Compared to the rigid-ring models, the flexible ring model can predict the tire forces over a broader frequency range up to 200Hz [Taheri et al., 2015].

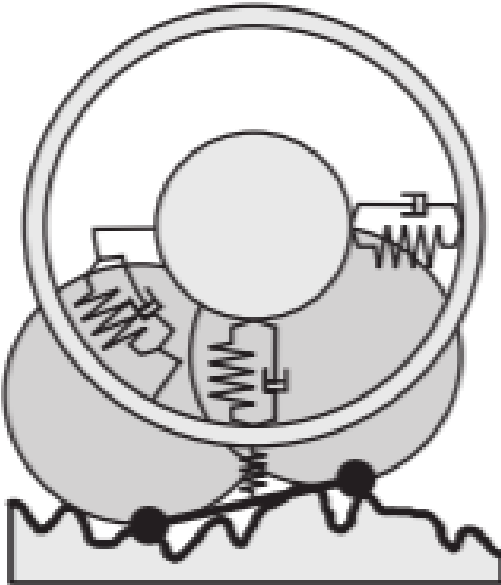


Figure 2.2. Rigid ring tire model [Schmeitz, 2004]

Semi-analytical models have been developed for predicting the forces developed at the tire-ground interface considering the physical phenomenon of tire-ground interactions. Such models can predict tire forces in the steady as well as transient states, while adequately considering mechanical properties of the tire, road friction, and operating conditions [Hirschberg et al., 2010]. Such models combine the lumped-parameter analytical methods to depict tire motion together with discrete element models to focus on individual areas or points of interest. Semi-analytical models, also termed as semi-FE or hybrid models, are considered to represent a compromise between the simplistic lumped-parameter and comprehensive FE models. These models, however, are also simplistic to investigate localized deformations of the tire constituents.

Mastinu et al. [1997] developed a semi-analytical tire model for enhanced vehicle dynamics simulations in the steady-state and transient conditions. The physical processes involved in tire-ground interactions were described using mathematical models of some tire components. The tire model yielded forces generated in the tire-terrain contact area in both steady and transient conditions, while considering the mechanical properties of the tire, friction coefficient, and a range of operating conditions. In another study, Chan and Sandu [2008] developed a semi-analytical technique to model a tire that could be applied to both on- and off-road conditions. The tractive force developed by the tire was evaluated

through the integration of the shear stresses developed at the tire contact interface. The experiments revealed that the tire model reverts to a rigid wheel when the soils deform much more than the tire.

2.1.1 FEA tire modeling

The Finite Element Analysis (FEA) techniques have been most widely used to develop, design, and analyze pneumatic tires [Chen et al., 2021; Zumrat et al., 2021; Jung et al., 2018]. In FEA methods, the element types used in the model and meshing constitute the most important aspects for achieving accurate results. The FEA tire models may employ one-, two- or three-dimensional elements with different aspect ratios. Padovan [1977] used a thin shell element model with an asymmetrical axial 2-D curve to investigate the energy dissipation and heat losses of steady-state rolling tires. The phase of the curve function was considered in this model and the simulation results were compared with the analytical results. Noor and Anderson [1982] stated that Padovan's thin shell element model ignored the crosswise shear stresses, and reported a FEA tire model using 2-D thick curved shell elements. The model enabled simulation of multilayer tire structure considering the anisotropic materials, crosswise shear stresses, inflation pressure, and response of the thermo-viscoelastic materials. Other studies [e.g., Crmn et al., 1988; Chen, 1988] have proposed novel approaches to model a two-dimensional tire. Young's modulus for the tire model was estimated from the readily accessible generalized deflection chart (GDC), while the Poisson's ratio was taken as 0.5. These tire models provided more accurate predictions of the tire-terrain contact geometry when compared to the previously reported approaches.

Later, Wang [1990] used a general-purpose FEA tool, referred to as ASGARD, to develop a three-dimensional tire model. The tire was modeled as a toroid filled with pressurized air, while the tire material was considered to be homogenous, and its Young's modulus was calculated from the load-deflection curve obtained from the tire manufacturer's GDC. The tire model could predict the load-deflection relationship accurately, while the relationships between the tire deflection and contact width, contact length or contact area showed significant deviations from the measured data provided by the tire manufacturer in the GDC. The observed discrepancies were attributed to the assumption of homogenous tire material. Nakashima and Wong [1993] reported an improved three-dimensional FEA tire

model considering different material properties for the tire tread and sidewall. Young's moduli for the sidewall and the tread were derived from the load-deflection and deflection-contact patch relationships provided in the GDC for a certain tire. The Poisson's ratios for the tread and sidewall were assumed to be close to 0.5, assuming that the volume of tire materials remains constant during deformation. Similarly, Zhang et al. [2001] designed a 3-D nonlinear FEA 12.5R22.5 truck tire model using hyper-elastic solid elements, shown in Figure 2.3, to predict tire contact pressure distribution on the terrain under different inflation pressures and vertical loads. The model considered four layers of steel belts under the treads, as shown in Figure 2.4, and a linear combination of alternating rubber and belt layers. This model assumed clamped boundary constraints at the rim contact regions, thereby no-slip condition, while neglecting the beads. The pressure distributions obtained under different vertical loads agreed well with the measured data.

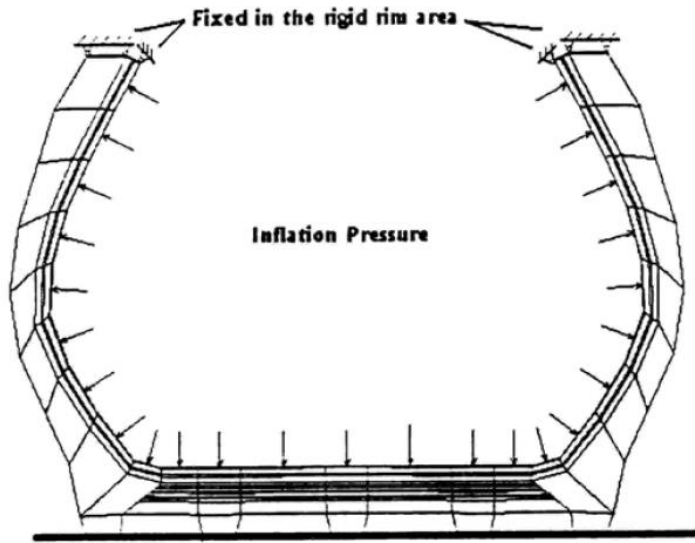


Figure 2.3. Tire model with constant shear stress in rim contact region [Zhang et al., 2001]

A number of studies have reported FEA models of the rolling tires. For instance, Yan [2003] reported a 9.00R20 truck tire model using the FEA technique to study the maximum contact area and reaction force under different speeds and vertical loads. Tire materials were handled as incompressible solid components using the Lagrangian multiplier approach. The Mooney-Rivlin material model was used to simulate the non-linear mechanical characteristics of elastomers, while the model constants were identified from

the experimental data. The carcass, belts and beads were modeled using an equivalent orthotropic material parameter, and the effective moduli were calculated using Halpin-Tsai equations based on the specific material characteristics of the rubber compound and the cords. The study concluded a decrease in maximum sectional width with increasing speed, which was attributed to sidewall materials' centrifugal force. A few other studies have reported higher vertical contact forces between the tire and the rigid surface with increasing rolling speed [Chae et al., 2001; Chang et al., 2002]. Olatunbosun and Bolarinwa [2004] developed a FEA rolling tire model in the ABAQUS platform using three-dimensional solid elements to analyze tire cornering characteristics. The reported tire model, however, lacked precise knowledge of tire composite and viscoelastic material features.

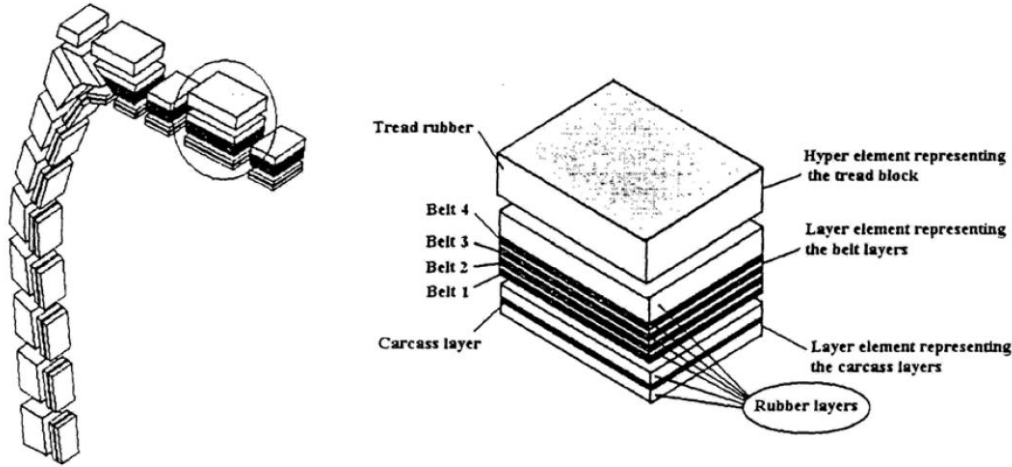


Figure 2.4. Tire components [Zhang et al., 2001]

Chae et al. [2005] developed a comprehensive FEA truck tire model using the PAM-Crash platform (Figure 2.5) to analyze static and dynamic forces developed by the tire while running over different surfaces such as a flat road, a drum with a cleat and a ditched road. The belts and the carcass were represented by multi-layer composite membrane components composed of an isotropic matrix layer and two cords layers governed in two directions. The 295/75R22.5 radial-ply tire model comprised 1680 layered membrane elements, 4200 solid elements and 120 beam elements. The model results showed good agreement with the experimental data. Ragheb et al. [2013] developed an 8×8 combat vehicle tire model using the PAM-Crash software to study its static and dynamic responses. The tire model included only the essential parts to reduce its design complexity and

simulation time. The lugs and grooves were replaced by straight edges, while the tread was modeled using solid tetrahedron elements with Mooney-Rivlin material characteristics.

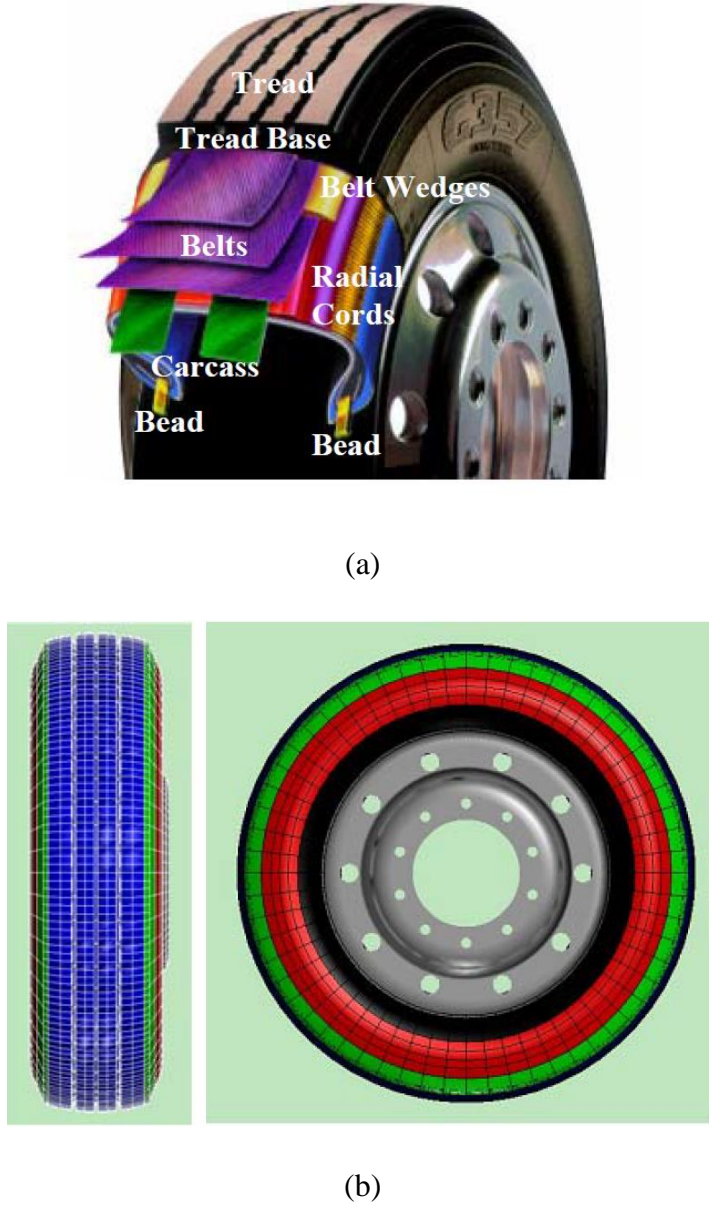


Figure 2.5. (a) Constituents of 295/75R22.5 truck tire (Goodyear.com); and (b) FEA truck tire model [Chae, 2006]

Shokouhfar et al. [2015, 2016a] developed a three-dimensional FAE model of a radial-ply truck tire in the LS-DYNA simulation platform to predict its vertical and cornering characteristics. The tire model was validated using the experimental data obtained from static and dynamic tests in terms of vertical stiffness, cornering force and free vertical

vibration response [Shokouhfar et al., 2016b]. The FEA tire model behaved well up to 100 km/h rolling speeds. The validated tire model was subsequently used to investigate the influences of multiple operational factors on tires' vertical and cornering characteristics. The study suggested that the detailed model could serve as a virtual tool for investigating the impacts of multiple operating and design factors on tire dynamic properties. Owing to the high computational demand of the model, the authors further developed a reduced model using the Part-Composite approach, where the multiple structural layers were represented by a single composite element with a layered arrangement [Shokouhfar et al., 2016c]. This approach resulted in a considerable decrease in the total number of elements in the model with a significant increase in computing efficiency.

El-Sayegh et al. [2019] developed a high lug farm service (HLFS) vehicle off-road tire (220/70B16) model using the FEA technique in PAM-Crash to study tire interactions with a SPH model of the clayey loam soil. The model, shown in Figure 2.6, employed hyperelastic Mooney-Rivlin material elements with 42 lugs for the tread pattern. The HLFS tire model comprised 21 parts including the rim, tread, under the tread, sidewalls, and belts. Quad shell elements were used to model the rim, while solid elements were chosen to represent the lugs, the shoulder and under treads. Lastly, beam elements were used to model the beads. The cross-section of the HLFS tire was constructed using these materials and then rotated about the tire axis to develop the full tire model. The tire model was used to predict the tire's interactions with the soil in terms of rolling resistance force under different inflation pressures and vertical loads, which agreed well with the measured data.

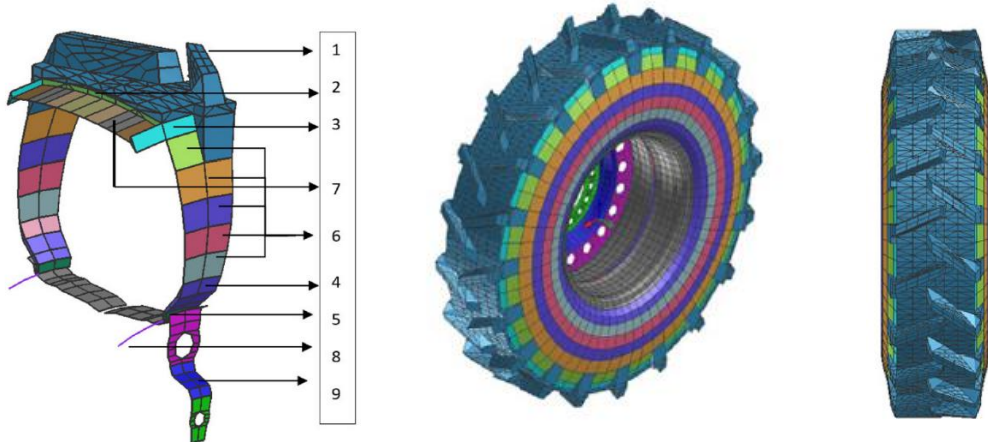


Figure 2.6. The FEA model of an agricultural vehicle tire [El-Sayegh et al., 2019]

(1: Tread, 2: Under tread, 3: Shoulder, 4, 5, 6: Sidewall, 7: Plies, 8: Beads, 9: Rim)

Xu et al. [2020] modeled a 37×12.5R16.5LT off-road tire using the FEA technique to investigate the tire performance on a gravel road. The modeling process employed in the study is illustrated in Figure 2.7. The model considered an asymmetric tread pattern with the tire centerline in addition to uneven anti-skid depth. A contact algorithm (*CONTACT TIED NODES TO_ SURVICE) was designed to connect tread pattern elements and tire body elements, and two belt layers and three cord ply layers were modeled using composite shells in order to seek more accurate prediction of the mechanical behavior of the cord–rubber composite elements.

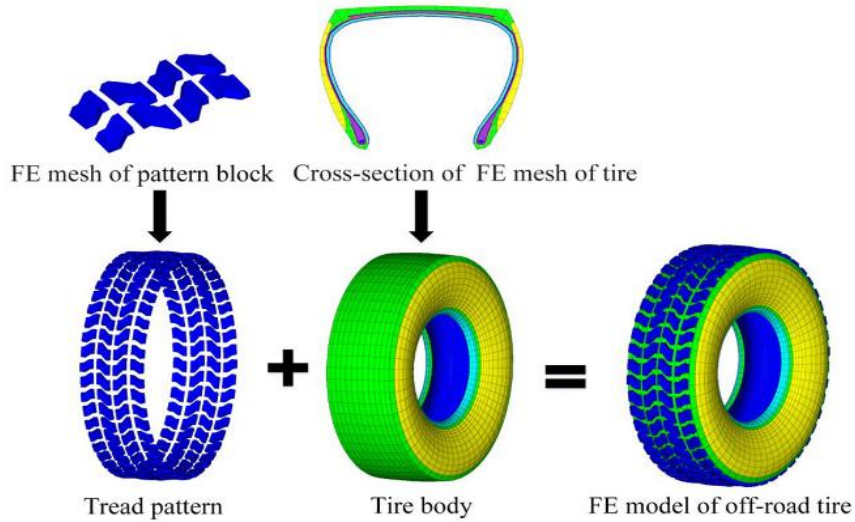


Figure 2.7. FEA model of a high-lug farm service vehicle tire [Xu et al., 2020]

2.2 Tire model validations

Studies reporting FEA tire models have used different static and dynamic tests to examine validity of the models. The static validation tests generally involve the multi-axis force-deflection or stiffness tests and the footprint tests. The dynamic validation tests, on the other hand, consider the drum-cleat, yaw oscillations and cornering tests. These tests are briefly described in the following subsections.

2.2.1 Multi-axis stiffness tests

The multi-axis stiffness tests provide measurements of global force-deflection properties of the tire along multiple axis in a relatively convenient manner. The stiffness of a tire is

affected by a number of tire design factors apart from the normal load and inflation pressure. Although the tire stiffness is generally characterized along the vertical or radial, lateral, longitudinal and torsional axis under different normal loads, the vertical stiffness tests have been most widely used to examine validity of FEA tire models. Figure 2.8 shows a vertical stiffness tester used to characterize the vertical force-deflection properties of a tire. The tire vertical stiffness is defined as the rate of change of normal force with respect to overall vertical deflection of the tire. The vertical stiffness of a tire is an important measure that directly affects the tire deflection, load-carrying capacity and vehicle ride property. The force-deflection properties of a tire can be conveniently evaluated from the FEA tire model by applying vertical load or deflection in an incremental manner. As an example, Figure 2.9 shows the vertical stiffness test simulation results obtained from a FEA tire model in PAM-Crash visual environment [El-Sayegh et al., 2019]. The results were obtained for a HLFS 220/80-B16 tire subject to an increasing normal load in a ramp manner. In the simulation, the FEA tire model, positioned on a rigid surface, was inflated to the desired internal pressure. The vertical load is applied to the rim center in a ramp manner, as shown in Figure 2.9. The figure illustrates variation in the applied force with the resulting vertical deflection of the tire. Figure 2.10 shows the vertical force versus deflection of the HLFS tire during the vertical stiffness test. It can be noticed that there is a good agreement between measurements and simulations up to about 6 mm deflection. The simulation model shows highly nonlinear stiffness characteristics beyond 6 mm deflection, while the measured data is nearly linear since the measured vertical force is plotted approximately versus deflection using limited number of points provided by the tire manufacturer. Although the FEA tire model showed good behavior under regular operating settings, the authors suggested further investigations under different working conditions. Marjani [Marjani, 2016], Chae [Chae, 2006], and Slade [Slade, 2009] used the same FEA technique to validate the tire models statically.



Figure 2.8. Tire vertical stiffness testing machine [Jafari, 2018]

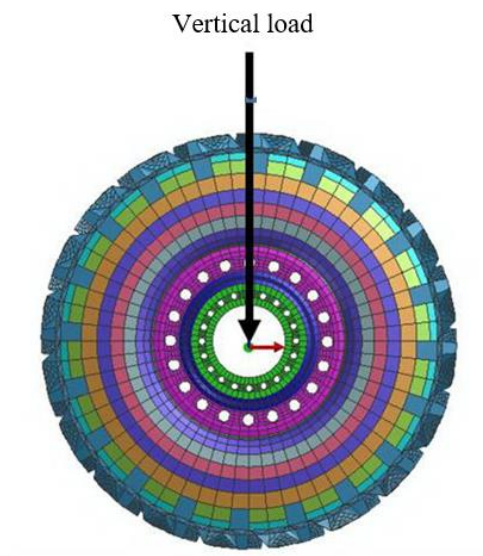


Figure 2.9. FEA HLFS tire size 220/80-B16 vertical stiffness test [El-Sayegh et al., 2019]

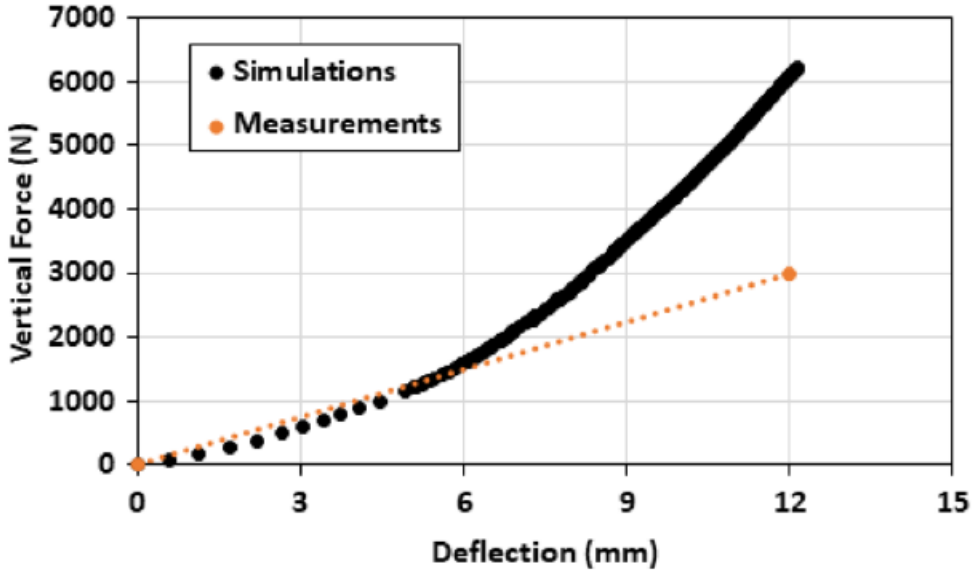


Figure 2.10. Comparisons of vertical force-deflection characteristics obtained from the FEA model of a HLFS tire with the measured data [El-Sayegh et al., 2019]

The vertical loading of the tire also yields its static footprint, which is further affected by characteristics of the road as well as the friction forces between the tire and the road surface. Owing to the vertical and longitudinal forces developed at the tire-ground interface, the tire adheres to the road surface. The tire, however, exhibits partial slippage during rolling depending on the available friction and geometry of the road surface, the maximum friction force, and the tire type. For the footprint tests, a null material road surface is generally considered such that the tire cannot penetrate the road surface. The vertical stiffness test available in Pam-Crash is used to simulate the tire's footprint under both non-rolling and rolling conditions. Stress contour in the Von-Mises direction is used to estimate the footprint area. Since both the inflation pressure and vertical load directly affect the footprint, the tests are generally repeated under different operating conditions [Chae, 2006]. As an example, Figure 2.11 shows the impact of vertical load and inflation pressure on the footprint of a commercial truck tire (385/55 R22.5) with 11.5 mm groove depth. An increase in vertical load causes greater deformations in the shoulder region, while the deformations in the crown region decrease [Xiong et al., 2014; Beer et al., 2012]. This is partly due to side walls flexibility and in part due to the load transfer influence in the lateral direction. Similar trends have also been reported in the tread deformation of passenger car tires [Ivanov, 2010; Sabri and Abda, 2018].

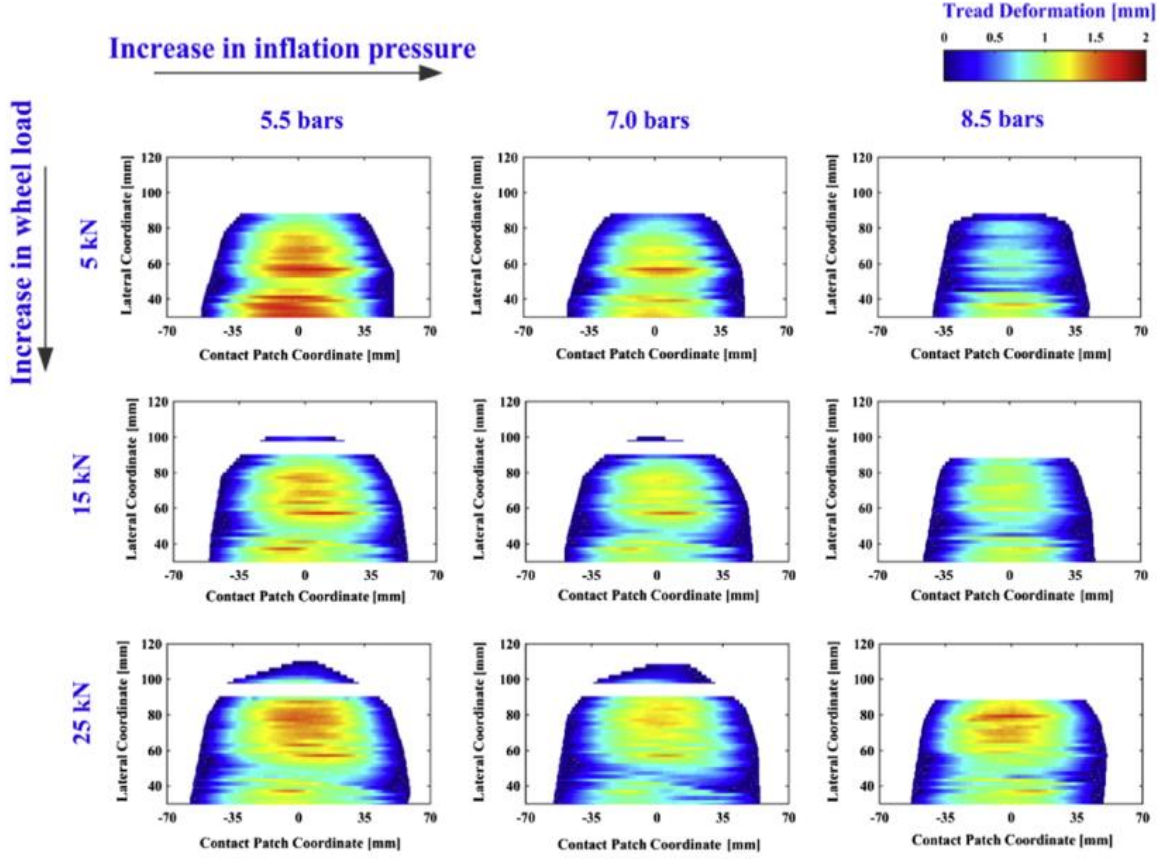


Figure 2.11. Measured truck tire footprint under different vertical loads and inflation pressures [Xiong et al., 2015]

A few studies have also investigated the influence of tire inflation pressure on tire tread deformation and footprint or tire-ground contact area. Xing et al. [2015] investigated the contact area of a tire considering three different inflation pressures (5.5 bar, 7.0 bar, and 8.5 bar) and showed an important effect of pressure on the deformation pattern of the tread. At relatively high inflation pressure of 8.5 bar, the study observed a Hertz contact-like deformation under 5 kN vertical load. This was attributed to reduced crown radius under the higher inflation pressure and light tire load, causing the road to deform the tire crown first. Gheshlaghi [2020] used the measured contact area to examine validity of the FEA model of a HLFS tire considering different tire loads. The comparisons, shown in Figure 2.12, exhibit similar trends with notable deviations between the simulation results and the measured data. Notable differences in the contact area results in Figure 2.12 is because of the resolution of tire model which is sliced in 60 pieces circumferentially. If the tire model is sliced in finer solid tread elements, less differences will be detected.

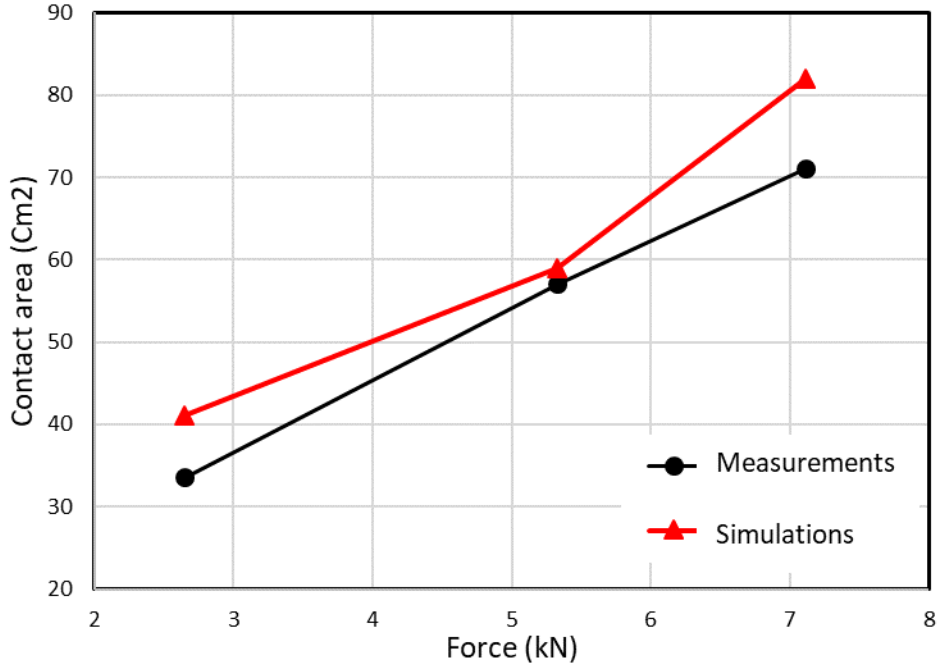


Figure 2.12. Comparison of contact area responses of a HLFS tire model with the measured data under different tire loads [Gheshlaghi, 2020]

The longitudinal stiffness of a tire is also evaluated in a similar manner, which directly relates to the braking and acceleration properties of the tire and its effectiveness in transmitting forces to the ground in the direction of movement. The tire longitudinal stiffness is generally defined as the ratio of the tire's longitudinal force to its longitudinal deformation. In the longitudinal stiffness test, the tire is first inflated to the desired inflation pressure, followed by the application of a fixed vertical load to the center of the tire. A longitudinal force is subsequently applied to the wheel center and the resulting longitudinal displacement is recorded in the steady-state. The model could predict longitudinal stiffness accurately within 1% error [El-Sayegh et al., 2019]. Figure 2.13 shows the longitudinal displacement of the FEA HLFS tire under 1.5 kN load and 193 kPa (28 psi) inflation pressure [El-Sayegh et al., 2019].

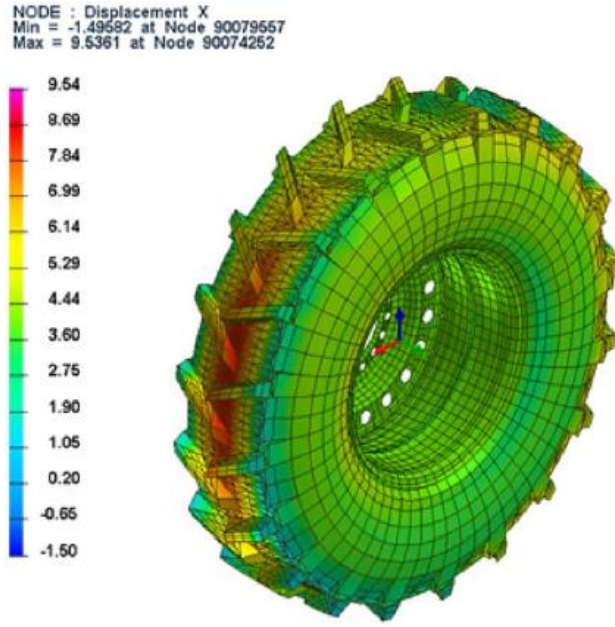


Figure 2.13. Longitudinal displacement on FEA HLFS tire at 1.5 kN and 193 kPa (28psi) inflation pressure [El-Sayegh et al., 2019]

Lateral stiffness, defined as the ratio of lateral force to lateral deformation, relates to the out-of-plane flexibility of the tire [Loeb et al., 1990]. It also relates to the tire's ability to transmit lateral forces from the vehicle to the road, which is vital for timely steering and control of the vehicle. As the lateral force increases, individual tread components lose adherence to the surface. The elastic characteristics of a tire in the transverse direction is also assessed in terms of its lateral stiffness [Luty, 2012]. In FEA model simulations, the tire is initially inflated to a desired pressure while subject to a constant vertical load applied to the center of the tire. Following the contact, a specific lateral force is delivered to the tire's center of gravity which causes the tire to deflect laterally. The lateral tire stiffness is calculated using the lateral displacement derived from the simulations. Reid [2015] used the same simulation technique in PAM-Crash to validate a Michelin XONE XDA 445/50R22.5 wide base tire model in the lateral stiffness test. The simulation results showed a good agreement with the measurements.

2.2.2 Dynamic validation tests

The dynamic validation tests involve characterizations of tire's resonant frequencies under pre-defined excitations and cornering force characteristics, although some studies have also

employed longitudinal force-slip characteristics of tires. The experimental and simulation methods employed for dynamic validations tests are briefly described below.

Drum-cleat test:

The drum-cleat test is performed to identify dominant natural frequencies of a tire rolling on a drum, where a semicircular cleat serves as an excitation to the tire. This test generally focuses on the fundamental mode of vertical vibration of the tire [El-Sayegh, 2019]. The FEA tire models also employ similar excitation to examine models' validity in terms of the fundamental frequency, which is strongly affected by material features, inflation pressure and normal load of the tire. In FEA models' simulations, the tire is loaded to a desired level after applying the target inflation pressure. An angular velocity is subsequently applied and the tire is permitted to roll freely, while the tire spindle is constrained in all translational directions. The drum center is also constrained in all translational directions with the exception of the rotational degree-of-freedom. The cleat located on the rolling drum surface excites the tire vertically. The vertical and longitudinal force responses at the tire center are extracted and a frequency spectrum of vibration is obtained using the Fast Fourier Transformation (FFT) algorithm. The spectra of vibration permit identifications of fundamental frequencies of vertical and longitudinal vibrations of the tire under different operating conditions. As an example, Figure 2.14 shows the frequency spectrum of vertical vibration response of a wide-based truck tire, which exhibits a distinct peak near 74 Hz, considered as the fundamental mode of vertical vibration. The spectrum also exhibits a dominant peak near 2 Hz, which corresponds to rolling speed of the drum. The Fourier spectrum of contact force suggests force magnitude of 500 N at 0 Hz. Since the mean of the force has been adjusted to zero prior to performing the FFT, the large magnitude at zero frequency is related to the vibrations that happen at 0 Hz because of inflating and loading the tire to the specific values. The measured data have also been used to estimate tire sidewall damping factor α [Chae, 2006; Marjani, 2016]:

$$\alpha = 2\xi\omega = 2\xi(2\pi f) \quad (2.1)$$

Where ω is the fundamental mode frequency in rad/s and ξ is the damping ratio, which is generally considered to be 5% [Chae, 2006]. El-Sayegh [2019], Chae [2006], and Slade

[2009] used the same technique in PAM-Crash to validate the FEA tire model in the dynamic domain.

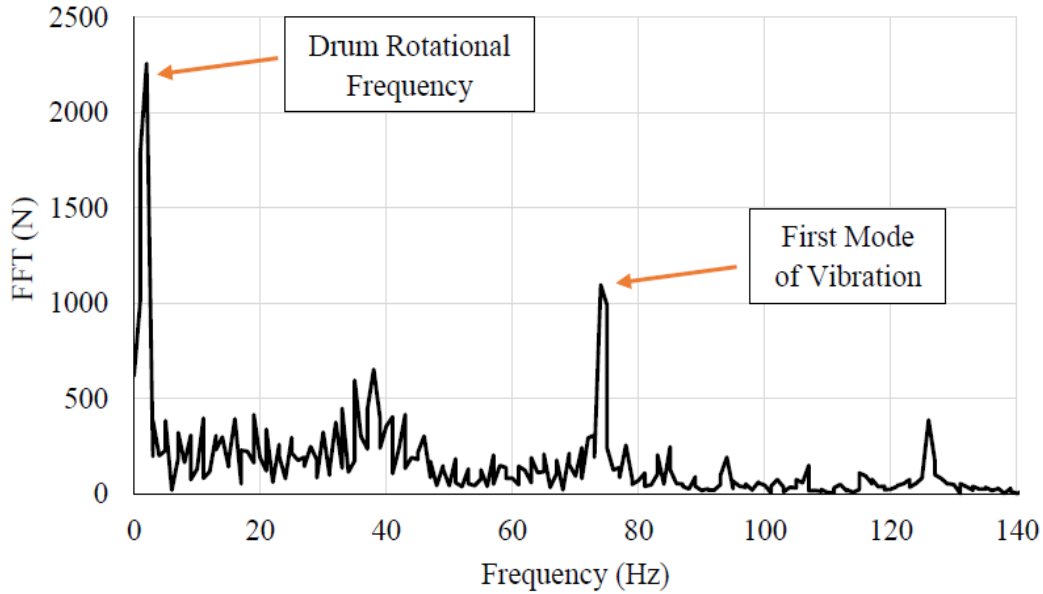


Figure 2.14. The vertical first mode of vibration of FEA wide-based tire at 45.4 kN vertical load and 827 kPa (120 psi) inflation pressure [Marjani, 2016]

Yaw Oscillation test:

The dynamic tire reaction to time-variant steering angle input differs significantly from that found under constant steering conditions [Schuring, 1976]. The dynamic tire reactions to sinusoidal steering inputs have been investigated using the yaw oscillation test. Figure 2.15(a) shows a yaw oscillation test comprising the tire, drum, trapezoid, and a hydraulic actuator. Chae [2006] presented a virtual yaw oscillation tire test in the FEA environment, shown in Fig. 2.15(b), to determine the dynamic lateral force and the time delay resulting from a steering input. In Figure 2.15(b), v and ω_y represent the drum speed and yaw oscillation test frequency, respectively. The study derived the frequency response in terms of amplitude ratio and phase angle as a function of the steering frequency. The estimated dynamic tire responses as a function of frequency showed good agreements with the measurements.

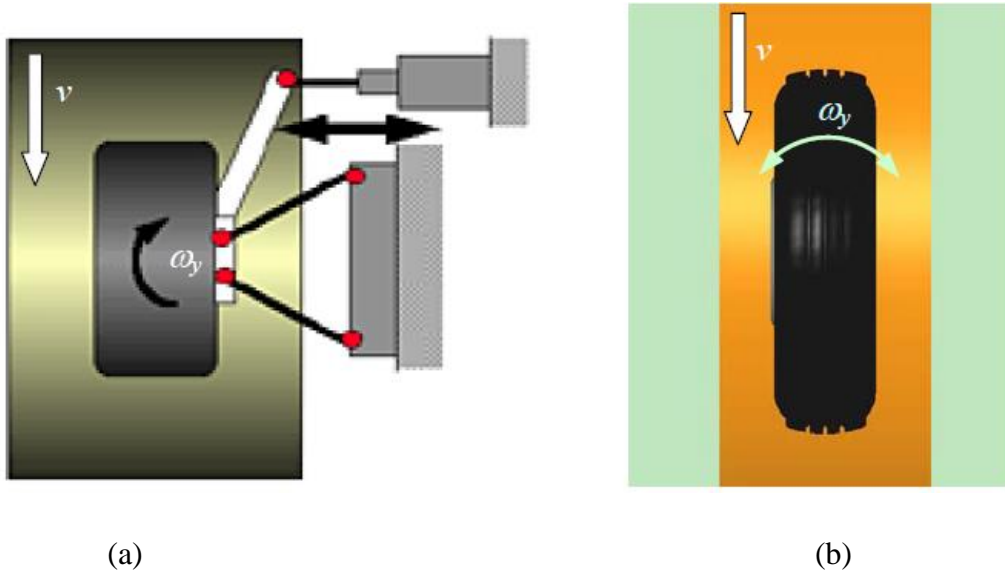


Figure 2.15. (a) Yaw oscillation testing machine; and (b) FEA yaw oscillation test model [Che, 2006]

Cornering test:

The out-of-plane dynamic responses of tire models have also been verified using the cornering test data. In virtual cornering tests, the tire is driven to a steady rolling speed and a side velocity is applied to achieve desired slip angle. The cornering force and self-aligning moment responses of the tire model, obtained at various slip angles, are compared with the measured data to demonstrate model validity. Chae [2008] performed cornering tests to examine validity of a FEA truck tire model (inflation pressure: 758 kPa (110 psi); normal load: 3.63 kN). The tire was rotated to achieve a steady forward speed of 5 km/h. Figures 2.16 and 2.17 illustrate the resulting comparisons of the model-predicted cornering force and aligning moment responses as a function of the slip angle under different vertical loads with the experimental data. The comparisons suggested good agreements between the simulation and experimental data for lighter loads and lower slip angles, while notable deviations are evident for the higher tire loads. Significant inconsistencies are also seen in the aligning moment responses at slip angles greater than 4°. The observed differences between the model and measured results, especially under a higher tire load, were attributed to differences in the cross-sectional forms, contact area and tread patterns.

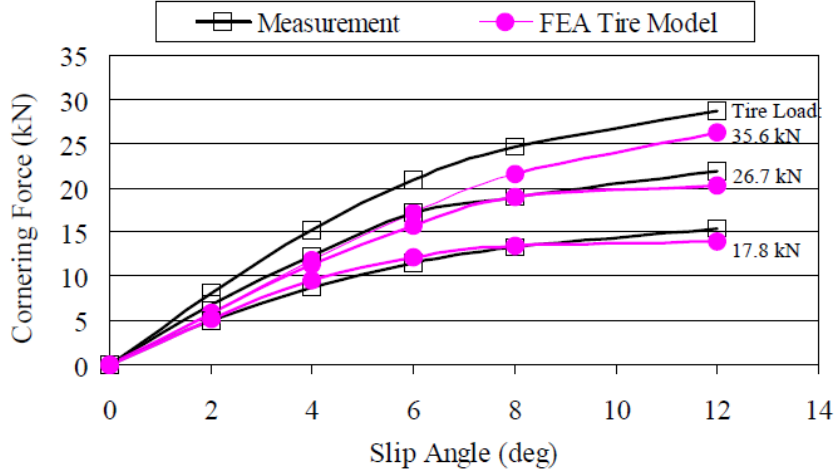


Figure 2.16. Cornering force validation using experimental data [Chae, 2006]

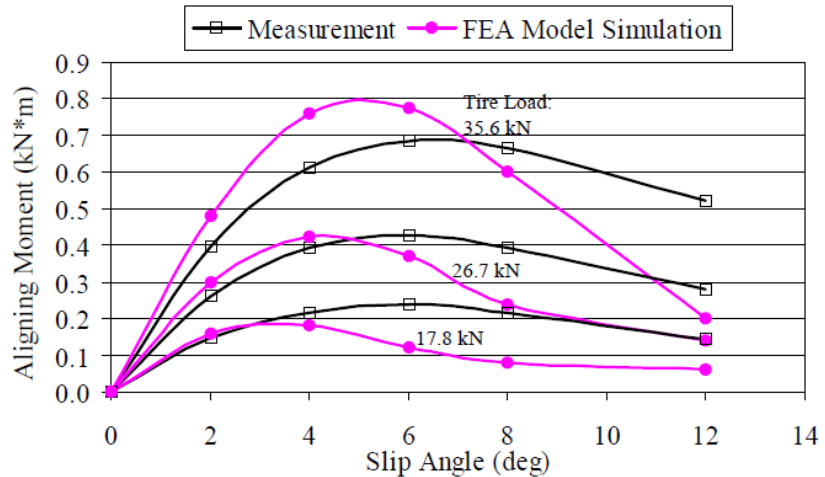


Figure 2.17. Self-aligning moment validation using experimental data [Chae, 2006]

2.3 Terrain modeling methods

The long-standing aim and fundamental issue in soil research have been the short overview of physical, chemical, and biological interactions. The first mathematical models in soil science date back to the 19th century, which was primarily used to simulate fluid flow [Keulen et al., 1971; Rubinet et al., 1963]. Comprehensive soil models, however, have evolved in recent years, which permit simulations of different soil types and their shear properties [Gheshlaghi et al., 2020; Gheshlaghi et al., 2021]. Soil behavior under the action of a tire is significantly affected by the applied external load, moisture content, contact area, and soil type in highly complex manners. Although a vast number of modeling techniques have been developed for different types of soils, the review in the following

sub-section is limited to two most important soil modeling techniques, mesh-based and meshless, for study of tire-terrain interactions.

The mesh-based techniques, such as finite element analysis (FEA) methods, are widely utilized to model soil structures [Nujid et el., 2014]. In the mesh-based FEA techniques, the soil is split into elements and the mesh size is extremely important as it directly relates to the accuracy of the analyses. The numerical results are strongly influenced by the model's complexity and the number of elements included in the analysis, although the computational demand increases significantly with increasing number of elements [Bindu et al., 2008]. The soil models based on this technique, however, may fail under large deformations leading to significant distortion of the mesh. Islam et al. [2019] presented a FEA modeling technique for soils using arbitrary LaGrange mechanics. The proposed technique also could not provide accurate soil behaviour under large deformations. Similarly, the soil models using finite difference methods (FDM) have shown the ability to capture the complete soil deformation process due to large deformation, movable frames, and unrestricted surface flow [Liu et al., 2003].

Alternatively, meshless methods such as discrete element method (DEM), material point method (MPM), and smoothed particle hydrodynamics (SPH) method have been proposed to overcome the limitations of the mesh-based methods [Liu et al., 2003]. Among these, the DEM is known to exhibit various flaws in terms of structuring the linked analysis, apart from its excessive computational demand [Cundall and Strack, 1979; Bui et al., 2008]. Furthermore, the DEM involves many complexities due to the lack of guidance with regard to model parameters identifications. The MPM, on the other hand, is a meshless numerical method that employs a background grid behind the soil particles. The MPM can reproduce a variety of geotechnical designs using single- as well as multi-phase materials [Abe et al., 2013; Soga et al., 2017]. It has been suggested that the method may yield considerable errors in soil modeling due to deformations of the background grid [Islam et al., 2019]. The finite volume (FVM) and the moving particle semi-implicit (MPS) techniques have also been developed as the meshless methods for modeling the soil flows [Islam et al., 2019; Kaneda and Sawada, 2019]. The reported studies, however, have shown inconsistent simulation results.

The smoothed particle hydrodynamics (SPH) technique has been employed in recent years to capture the soil flows more accurately. The SPH technique was developed in the 1970s to address astrophysical modeling challenges [Gingold et al., 1977]. The SPH method is considered superior over the other meshless methods since it permits consideration of the real particle structure with no connection, while it involves relatively simpler formulations and solution methods [Rahman and Konagai, 2017; Gholami et al., 2018]. The resolution of this approach can be adjusted for different application domains such as solid mechanics and fluid flow because of its capacity to handle boundary particles and its Lagrangian character in addition to the essential soil factors such as density [Akbari, 2017; Ran et al., 2015; Ghaitanellis et al., 2018]. In the SPH method, each particle is considered with its unique features, such as mass, density, and velocity, which are adjusted using a smoothing kernel from those of the nearby particles within a defined domain. The simulation process is continued until the required time or velocity is attained, followed by numerical integration to adjust each particle's location [Islam et al., 2019]. The basic step in SPH is the integral form of a function, which describes the function at a location r , such that:

$$A(r) = \int A(r')W(r - r', h)dr' \quad (2.2)$$

Where, h is the smoothing length defining the influence domain A , r and r' are covered in the integration domain $A(r')$ [Larry et al., 1993]. Function W , commonly known as the smoothing function, is an interpolating kernel that must meet three characteristics. The first characteristic relates to normalization condition of W , which must satisfy:

$$\int W(r - r', h)dr' = 1 \quad (2.3)$$

$$\lim_{h \rightarrow 0} \int W(r - r', h)dr' = \delta(r - r') \quad (2.4)$$

$$W(r - r', h) = 0 \quad \text{when } |r - r'| > kh \quad (2.5)$$

Where k describes the domain of $A(r)$ and is a constant associated with the smoothing function for a point at r , as shown in Figure 2.18. The second characteristic represents smoothing function ($W(r - r', h)$), when h approaches zero. The third characteristic

represents the compact conditions that define the range of $A(r)$ and relate to the smoothing function at position r , as illustrated in Figure 2.18.

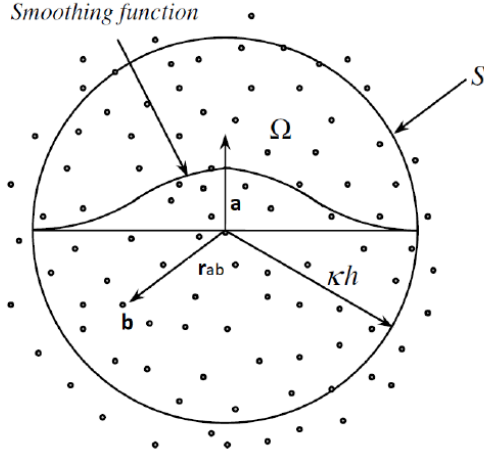


Figure 2.18. Particle interpolation utilizing particles inside the smoothing functions domain [Bui et al., 2007]

The cubic spline has been widely employed among the kernel functions since it is comparable to a Gaussian function, which is regarded as an ideal choice owing to its simplicity [Islam et al., 2019]. Such a function, however, is associated with high computational demand compared to other functions. Jaseph et al. [1985] employed the following cubic spline function, which offers the advantages of the Gaussian feature apart from being compact:

$$w(q, h) = \alpha_d \begin{cases} 1.5 - q^2 + 0.5q^3 & 0 \leq q < 1 \\ \frac{(2 - q)^3}{6} & 1 \leq q < 2 \\ 0 & q \geq 2 \end{cases} \quad (2.6)$$

Where $q=|r - r'|/h$ and α_d is described by $\frac{1}{h}$, $\frac{15}{7\pi h^2}$ and $\frac{3}{2\pi h^3}$ in one, two, and three-dimensional space, respectively.

The total stress tensor $\sigma_i^{\alpha\beta}$ is related to the isotropic pressure (P), the Kronecker's delta ($\delta^{\alpha\beta}$), which is taken as 1 if $\alpha=\beta$ and 0 otherwise, and the shear stress ($\tau^{\alpha\beta}$), as:

$$\sigma^{\alpha\beta} = -P\delta^{\alpha\beta} + \tau^{\alpha\beta} \quad (2.7)$$

The pressure P in the above formulation is obtained from the “equation of state” considering the material density and internal energy [ESI group, 2014]:

$$P = C_0 + C_1\mu + C_2\mu^2 + C_3\mu^3 + (C_4 + C_5\mu + C_6\mu^2)E_i \quad (2.8)$$

The above formulation has been used for hydrodynamic elastic-plastic materials, where C_i ($i=0$ to 6) are material constants, $\mu = \rho/\rho_0 - 1$ is the density factor, and E_i is the internal energy. The shear stress rate, $\dot{\tau}^{\alpha\beta}$, is subsequently obtained as a function of the rate of the strain tensor $\dot{\epsilon}$, as:

$$\dot{\tau}^{\alpha\beta} = 2G \left(\dot{\epsilon}^{\alpha\beta} - \frac{1}{3} \delta^{\alpha\beta} \dot{\epsilon}^{\gamma\gamma} \right) \quad (2.9)$$

Where G is the shear modulus. The shear stress factors should be restricted to the surface failure that occurs when plastic flow begins. The plastic flow area is estimated using the Mohr-Coulomb relation [Wong, 2008].

$$\tau_{max} = c + P \tan \varphi \quad (2.10)$$

Where c is soil cohesion constant, P is applied pressure, and φ is the internal friction angle. El-Gindy et al. [2011] used FEA and SPH techniques to model the soil and investigate the tire-soil interaction process. The soil was modeled as an elastic-plastic material in both the techniques and the results showed that the SPH soil deforms like the real soil in the shear-strength test. Dhillon [2013] studied the sensitivity analysis of the SPH technique in the PAM-Crash environment for modeling different soils. The impact of soil model characteristics such as geometry and contact model on the behavior of soft soil was investigated. The predicted soil parameters were compared to the experimental data to verify the models [Dhillon, 2013].

Marjani [2017] used SPH and FEA techniques to model dry sand and investigate the computational efficiency of the tire-soil interaction process using different types of soil models such as full FEA, full SPH, hybrid half SPH/FEA, and hybrid quarter SPH/FEA. Pressure-sinkage and shear strength tests were used for the soil model calibration, which ensured more accurate representation of dry sand. In terms of the pressure-sinkage test, the simulation results obtained from both modeling methods agreed reasonably with the measurements. Due to a lack of penetration in the FEA model, a sponge-like effect was

detected, which was accomplished using the SPH modeling method. The shear strength test was found to be applicable only for the SPH soil model. Using a rigid tire-soil interaction model, the computational efficiency of each soil model was investigated and compared. It was discovered that the quarter SPH soil model is the most efficient soil model under the same operating conditions. Compared to full SPH, the hybrid quarter SPH soil model reduced computation time by 45.67 percent.

Zhao et al [2022] studied slope collapse under large deformations using the SIMSAND critical state sand model in conjunction with the smoothed particle hydrodynamics (SPH) method and discrete element method (DEM). As benchmarks, a series of slope collapse studies utilizing the discrete element method (DEM) with different particle forms (spherical, tetrahedral, and elongated) and different initial densities (dense and loose) were used. Comparisons showed that the SIMSAND-SPH technique could recreate the main characteristics of slope collapse, qualitatively and quantitatively, such as the free surface, final deposit configurations, and final runout distance. In comparison to DEM, the proposed SIMSAND-SPH technique showed better computing efficiency while keeping the same computational accuracy.

2.4 Terrain models' calibrations

The soil models are generally calibrated by identifying essential model parameters using the measured data. The studies have reported different test techniques to measure soil strength and shear properties. These include the bevameter, the cone penetrometer, the triaxial instrument, and classic civil engineering procedures, which are briefly discussed in the following sub-sections.

2.4.1 Soil penetration tests

Soil penetration tests are performed to characterize soil strength and pressure-sinkage relationship using the bevameter and cone penetrometer. The measured data have been used to predict off-road vehicle mobility and tire traction and provide guidance on the tillage tools designs [Taghavifar and Mardani, 2017; Ogbeche and Idowu, 2016]. The apex angle and the penetration rate are the significant factors that impact the penetration force. Studies reporting empirical and DEM soil models have shown that model calibrations on

the basis of a basic penetration test, such as a cone penetrometer test, necessitate a deeper understanding of the particle size to cone penetrometer ratio apart from the geometry scaling ratio [Syed et al., 2017]. The level of cone penetration resistance is affected by the size of the virtual container in which the cone penetrometer test is done. Bolton and Gui [1993] showed that cone penetration resistance is insensitive to the soil box diameter when it is more than 80 times the cone base diameter. Bolton [1993] suggested a DEM virtual container with a radius of 250.6 mm for the cone penetrometer simulation. The box size effects, however, are strongly related to the DEM particle size, stiffness, and friction. Another study suggested that the minimum number of DEM particles contacting the cone should be 13 or more [Jiang and Yu, 2006].

Although the cone penetrometer is easy to use on-site, the measurements differ considerably depending on the operators' skill level [Kim et al., 2021]. The cone index also represents the link between compression and shear characteristics, which cannot be separated. As a result, Kim et al. [2021] suggested some limitations of this method for the study of tire-terrain interactions focusing on developments in off-road vehicles.

Alternatively, the bevameter test was proposed to overcome limitations of cone penetrometers. The bevameters have been used to perform pressure-sinkage and shear strength tests for characterizing mechanical properties of soils [Bekker, 1969]. Figure 2.19 illustrates a soil test system using bevameter. Wong [2010] performed penetration tests for different soils and concluded that the bevameter is the most accurate representation of interactions between the soil and a tire, although the measurement method is more difficult and time-consuming than the cone penetrometer. Massah and Noorolahi [2010] constructed a tractor-mounted bevameter for analyzing the characteristics of snow using circular, elliptical, and rectangular plates, and found that the form of the plate had an important effect on the measured properties. Kim et al. [2021] introduced a new bevameter to determine parameters that influence the bevameter's performance. The pressure-sinkage test was carried out using circular plates of various sizes, and the findings revealed reduced pressure-sinkage parameters with increasing plate size. The study also considered a normal pressure via a dead load applied to the shear-test equipment in order to prevent normal-pressure changes with displacement and speed. In addition, a spline was added to top of

the shaft attached to the shear ring to evaluate slide sinkage during the shear tests. The pressure–sinkage and shear stress–slip displacement relationships, rather than the pressure–sinkage alone was found to be more accurate predictors of sinkage.

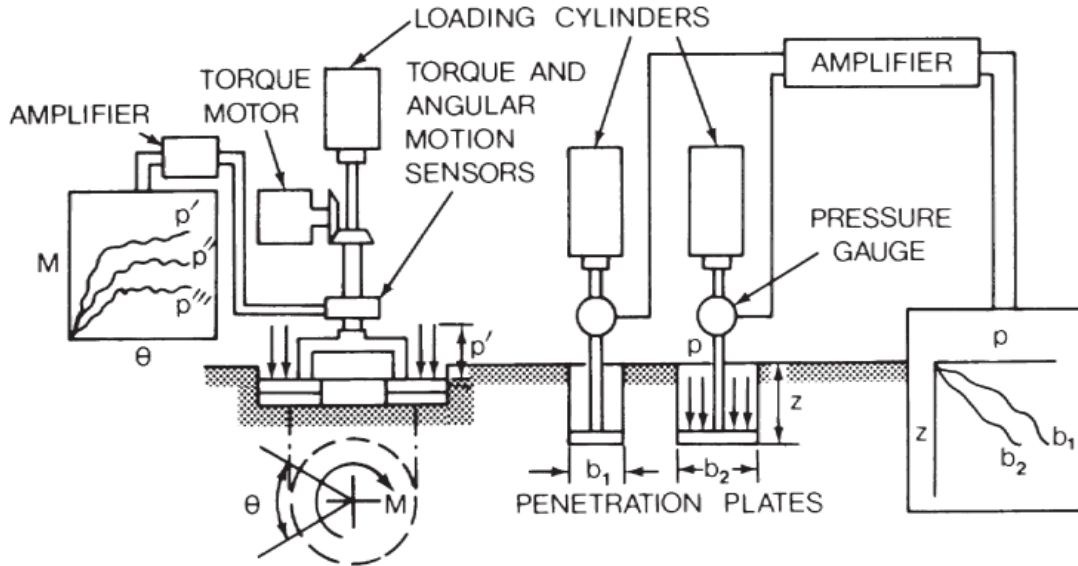


Figure 2.19. Bevameter schematic [Wong, 2008]

2.4.2 Pressure-sinkage tests

The pressure-sinkage testing of a soil is performed by placing a penetrating plate on the soil surface, while measuring the resulting normal tension. This test is used to measure soil sinkage under different vertical loads and the data is used to identify parameters of the pressure-sinkage relationship [Wong, 2008]:

$$P = \left(\frac{k_c}{b} + k_\phi \right) Z^n \quad (2.11)$$

Where K_c , K_ϕ , and n are soil parameters and b is smaller dimension of the penetrating plate.

The FEA methods have also been used to obtain the pressure-sinkage behaviours of soils in a virtual manner. As an example, Figure 2.20 shows a FEA test box filled with SPH soil and water particles [Gheshlaghi and Mardani, 2020]. In the virtual test, the plate沉降 is measured and compared to the experimental data under different normal pressures in order

to calibrate the soil models. Marjani [2015] and Slade [2009] used a similar FEA technique to calibrate different soil models.

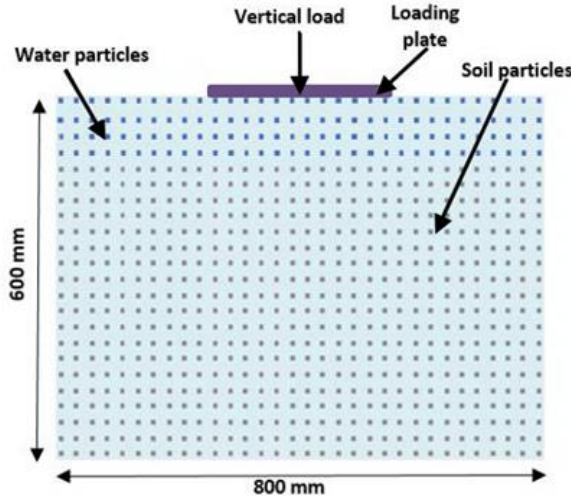


Figure 2.20. The FEA pressure-sinkage test for 17% moist clay loam soil [Gheshlaghi and Mardani, 2020]

2.4.3 Shear strength test

The shear-strength test is performed by twisting a toothed plate into the soil while measuring the resulting shear stress [Chu et al., 2005]. Figure 2.21(b) illustrates a typical shear test setup for soils. The test data are used to identify shear stress relationship constants such as cohesion coefficient c and internal friction angle φ [Wong, 2008]:

$$\tau = c + P \tan\varphi \quad (2.12)$$

Figure 2.21 shows the FEA shear strength test setup for a moist clay loam soil. The test is done using a box made up of three parts. The top and middle plates are subjected to a vertical load and horizontal velocity of 10mm/s, respectively, while the lower plate is fixed. The shear stress values are then extracted after 100 mm displacement. The shear stress response obtained from the model is compared with the measured data for calibrating the soil model [Gheshlaghi and Mardani, 2020]. El-Gindy et al. [2011] and Marjani [2016] used a similar shear-strength test method to evaluate relative effectiveness of FEA and SPH soil models.

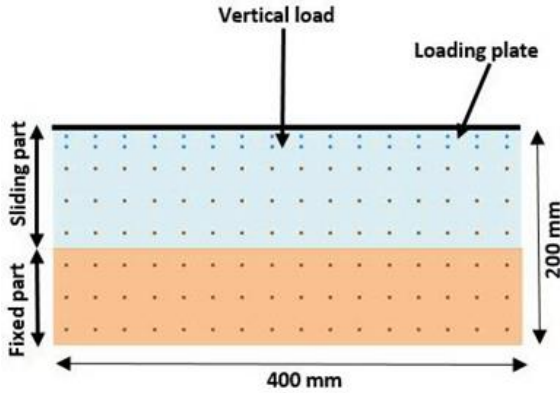


Figure 2.21. The FEA shear-strength test for 17% moist clay loam soil; and [Gheshlaghi and Mardani, 2020]

2.5 Tire-terrain interaction modeling

The performance of off-road tires on soft terrains is increasingly being investigated using FEA methods, where the continuum objects such as tire and soil models are idealized via the finite number of two-dimensional and three-dimensional elements. The FEA tire models in conjunction FEA or SPH soil models have been used to study tire-terrain interactions focusing on rolling resistance, traction forces and cornering properties of the tires in addition to the soil responses. The reported studies on these aspects are briefly summarized below.

2.5.1 Rolling resistance analysis

The rolling resistance of a pneumatic tire is affected by a variety of factors including the tire structure, materials, terrain features, inflation pressure, speed, vertical load, and temperature. Bias-ply tires exhibit considerably higher rolling resistance than the radial-ply tires for a given rated load and inflation pressure [Chae, 2006]. This is attributed to relatively higher hysteresis losses associated with the cross-ply structure of the bias-ply tires. The thicker treads and sidewalls together with a higher number of carcass plies also contribute to increased rolling resistance of the tire. The tires comprising synthetic rubber compounds also exhibit higher rolling resistance when compared to those made of natural rubber [Chae, 2006]. A number of studies have used FEA tire models to investigate rolling resistance of tires on rigid as well as deformable terrains under different operating

conditions. Some of these are summarized in Table 2.1 together with the operating conditions considered.

Table 2.1. Recent research on tire-soil interaction with FEA techniques to evaluate tire rolling resistance

Author	Model specification		Operating conditions	Modeling technique		Evaluation method	Model Features
	Tire	Terrain		Tire model	Terrain model		
Shoop, 2001	Truck	Snow, Sand	Terrain depth	3D FEA	FEA	Experiments	An accurate FEA tire model, new material for fresh snow, modal analysis tire model on snow
Grujicic et al, 2010	Goodyear Wrangler HT 235/75 R15	Sand	Inflation pressure, vertical load, slip	FEA with 8-node and rebar elements	FEA with 8-node solid elements	Published data (063,064)	Simulation of tire-sand interactions with FEA results and Pacejka magic formula combination
Li, 2013	Radial truck tire	soil	Load, inflation pressure	2D and 3D FEA	FEA	Measurements	An accurate 3-D non-linear tire model, pressure measurements with a 3D kinetic scanner in the lab, with experimental validation
Sandu et al, 2019	Michelin LTX 235/85R16	Rigid terrain	Vertical load, Slip ratio	lumped-mass discretized model using Kelvin-Voigt material elements	FEA	Published data (Pacejka and Bakker, 1992)	Minimizing the error between predictions and measurements using a 3D distributed brush model for contact algorithm and a LuGre friction model for maneuvers
Gheshlaghi et al, 2020	HLFS tire	Clay-loam	Vertical load- multi-pass	FEA	SPH	Measurements	The superiority of FEA technique over Bekker and Wismer-Luth model

The tire model reported by Yong and Fattah [1976] was among the first FEA-based models developed to predict subsoil response behavior and rolling resistance of tires running over uneven terrain. The tire was modeled as a semi-flexible ring with plane strain and the soil was modeled using the stress-strain test and the yield criterion. The tire-soil contact area and subsoil reaction have to be predicted as part of the method. The analytical model used in the study was designed to mimic the physical motion of the wheel as nearly as possible

by accounting for the loading/unloading soil response beneath the wheel. The particle path representing the soil displacement is determined considering the wheel geometry and degree of slip. Correlations with performance measures were used to validate the theoretical specification's applicability. Moreover, the FEA models have been used to evaluate tire-soil interactions in terms of tire deformation, energy losses, and contact area changes considering the wheel loading and slip, boundary conditions, and soil deformations [Yong et al., 1978]. The results showed superior ability of the analytical technique for the semi-flexible tire model operating on soft clay. The study however did not address the effects of variations in operating parameters such as speed, inflation pressure, multi-pass, and terrain characteristics.

Marjani et al. [2017] implemented the SPH technique to simulate dry sand together with a FEA truck tire model to investigate rolling resistance of a wide base tire operating on dry sand. The soil model was calibrated using pressure-sinkage and shear-displacement tests. The effects of load and inflation pressure variations on the tire rolling resistance were studied, which showed good agreements with the measured data. The study, however, did not address the effects of some of the important operating conditions such as rolling speed, multi-pass, slip, and terrain features. Farhadi et al. [2019] modeled the interaction between a treaded tire and moist clayey loam soil using the FEA technique to evaluate rolling resistance, contact area, and contact volume. The moist soil was modeled using the Drucker-Prager model in the Abaqus software considering three different levels of moisture contents and the tire was modeled using FEM. The simulation results for rolling resistance, contact volume, and the contact area showed a good agreement with the measurements. As in the case of above-mentioned studies, the important parameters affecting the tire-terrain interaction were not considered, namely, the tire speed, slip, and multi-pass. Guo et al. [2020] analyzed the rolling resistance of a truck tire under various operating conditions using a three-dimensional tire-pavement model. The results were used to formulate a rolling resistance relationship with the operating speed and inflation pressure, as:

$$RR = (0.13153 - 0.00211V + 0.00001V^2)F^{1.13258} \cdot P^{-0.28753} \quad (2.13)$$

Where RR refers to rolling resistance coefficient, V is forward speed, P is inflation pressure and F is the tire load. The applicability of the proposed relationship, however, is limited since the contributions of many important factors, such as multi-pass, terrain properties and slip were not considered.

2.5.2 Cornering characteristic analysis

Cornering force is a function of the tire characteristics such as side-slip angle, inflation pressure, vertical load, speed, driving condition in addition to the soil parameters such as cohesion, internal friction angle and moisture content. The cornering properties of tires, however, have been investigated in relatively fewer studies using experimental as well as numerical methods. The reported studies have used FEA models of tires together with terrain models to determine cornering properties under selected operating conditions. Table 2.2 summarizes some of the recent studies on analysis of cornering characteristics of off-road tires using FEA tire models. Gengenbach [1986] conducted an experimental investigation on the cornering performance of various tires operating over a wet surface. The study observed increase in the cornering force with increase in the inflation pressure under a given constant tire load. Grosch and Maycock [1968], however, reported a reduced cornering coefficient with increasing speed. Goran et al. [2013] determined cornering stiffness through integration of a mathematical model and real vehicle exploration parameters. The study involved the analysis of a tire mathematical model, identification of key real exploitation parameters, and integration of a mechatronic system for tire load monitoring. Measurements of tire load and subsequent integration of measured values into the developed software modules provided determination of cornering stiffness for the given vehicle and road contact patch conditions.

Table 2.2. Recent studies on tire-soil interactions for characterizing cornering properties using FEA tire models

Author	Model specification		Operating conditions	Modeling technique		Evaluation method	Advancements
	Tire	Terrain		Tire model	Terrain model		
Allen II et al, 2007	MSD 315/80R22.5	Sand, hard soil	Terrain characteristics	FEA	FEA	Published data	Evaluations of cornering characteristics
Kayacan et al, 2014	Tractor-trailer tire	-	Speed	Nonlinear dynamic model	-	Experiments	Introducing a new benchmark for evaluating the performance of many model-based control techniques
Wei et al, 2016	235/60 R18 tire	Rigid surface	Tire material and structure	3D FEA	FEA	Experiments	Parametric analysis using the Design of Experiment (DOE) matrix method
Sandu et al, 2019	Michelin LTX 235/85R16	Rigid terrain	Vertical load, Slip angle	lumped-mass discretized model using Kelvin-Voigt material elements	FEA	Published data (Pacejka and Bakker, 1992)	Minimizing the error in rigid terrain-tire interaction, minimizing the computational time for commercial purposes

Mashadi et al. [2015] proposed a method for relating the Magic Formula tire model's coefficients to the tire physical features under different operating conditions such as inflation pressure, vertical load, slip ratios and tire rim diameter. The lateral force output of this model was validated using the available tire data before being utilized to determine tire force properties. The study employed two different FEA models of P205/60R15 91H tires with different tread patterns in the ABAQUS platform and the lateral force was calculated for each scenario using approximated coefficients and simulations. The tire cross-section was initially modeled in two dimensions (2D) and a desired internal inflation pressure was applied. The radial tires' reinforcement belts were then distorted to achieve 3-

D representations. It was demonstrated that using this approach, the MF tire model coefficients could be estimated in terms of tire load and physical attributes. El-Sayegh and El-Gindy [2018] evaluated cornering characteristics of a wide base truck tire (445/50R22.5) operating on a wet surface considering variations in different operating conditions such as inflation pressure, wheel loads, and water depth. The water was modeled using smoothed-particle hydrodynamics, while the wide base truck tire was modeled using FEA. The lateral force, rolling resistance, cornering stiffness, and self-aligning moment were among the cornering parameters studied. The simulation results showed good agreements with the experimental data.

The reported studies have mostly neglected the important effects of operating speed, tire slip, inflation pressure and multi pass condition, which are known to strongly affect the tire-terrain interactions. Moreover, the studies were mostly limited to a particular tire and terrain such as water covered pavement or dry or moist sand or clay. The knowledge of tire interactions with different soils or soil properties thus remains limited.

2.5.3 Soil behavior analysis

Soil compaction due to rolling tire operation is an unavoidable event. The soil compaction due to contact pressure caused by the heavy vehicle mobility and loads strongly affects the off-road vehicle traction efficiency, although this raises many concerns with regard to soil erosion, runoffs, hardpan formations, energy loss, and environmental-related damages [Gheshlaghi and Mardani, 2021]. The soil compaction has been studied extensively using analytical and FEA tire models. Many analytical models have also been developed to describe the process of changes in the soil characteristics considering multiple tire passes.

Liu et al. [1996, 1999] analyzed sand-tire interactions using the finite element program MARC that included a modified Cam–Clay critical-state soil model as well as a nonlinear elastic law. The study included a soil model in a large strain framework considering substantial soil deformations resulting from plastic deformations and localized failures. Guo et al [2020] investigated soil compaction in terms of contact stress distributions under various operating conditions using a three-dimensional tire–pavement model. Figure 2.22 illustrates the contact stress distribution under the tire. The longitudinal contact stress was symmetrically distributed in the longitudinal direction, as shown in Figure 2.22b, while the

lateral contact stress was virtually anti-symmetrically distributed in longitudinal direction, as shown in Figure 2.22(c). The longitudinal contact stress was negative at the leading portion of the contact region and positive at the trailing end. The contact region with negative stress distribution, however, was considerably smaller than that of the positive stress distribution.

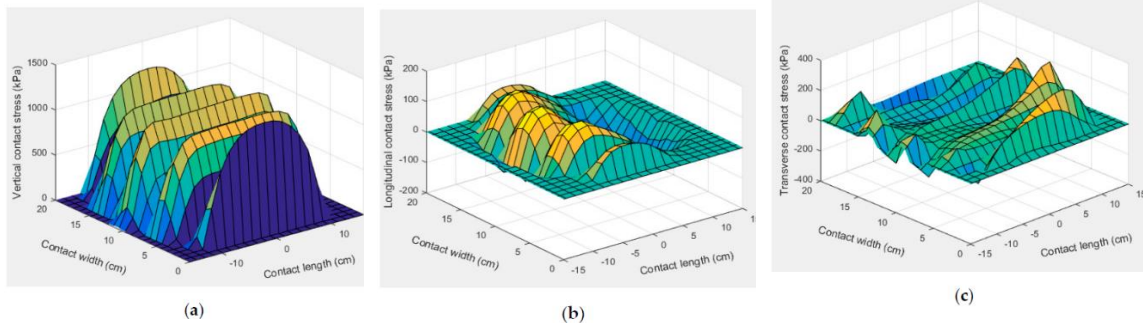


Figure 2.22. (a) vertical, (b) longitudinal, and (c) transverse contact stress distribution of a free-rolling tire with a 32.5 kN load [Guo et al., 2020]

Sandu et al. [2019] developed a Hybrid Soft Soil Tire Model (HSSTM) to evaluate the tire-terrain interactions. The main goal was to describe the soil deformations in the vertical and longitudinal directions under different operating conditions. A visualization environment was created to show the behavior of the user-defined terrain, such as plastic deformations and stress distributions. Figure 2.23 depicts snapshots of the terrain viewing environment under multi-pass conditions. Owing to the nonlinearities of the HSSTM, the study presented the responses under a variety of normal and tangential loads. The simulation results revealed unequal permanent plastic deformation of the ground following the tire passing. The study further revealed that positive shear forces continue to drive the tire forward when it is traveling on a deformable terrain under an applied torque, while the negative ground forces oppose the tire motion.

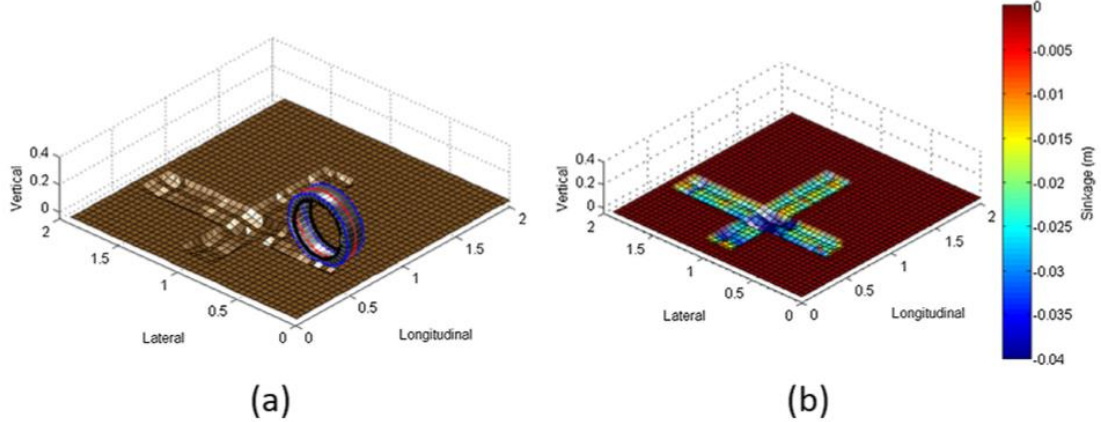


Figure 2.23. Terrain mapping during the multi-pass simulation of a driven tire (a) soil consecutive loading-unloading (b) Contour of terrain sinkage [Sandu et al., 2019]

Gheshlaghi et al. [2021] investigated the soil stress distribution under an off-road tire using the SPH-FEA model under different operating conditions. Tire-moist soil experiments were also conducted utilizing a single wheel tester in a large soil storage area. A bevameter and a shear-strength box were used to estimate soil model parameters. From the comparisons of simulation results with the experimental data, it was concluded that the FEA-SPH model could accurately predict the soil stress distribution. In another study, Gheshlaghi et al [2020a] used the same simulation technique to study soil density and sinkage effects that are directly related to changes in soil compaction. With a particular user-distinguished kernel function, the SPH technique predicted the local density reasonably well.

2.6 Summary

This chapter presented a review of available published works related to tire-terrain interaction modeling and testing. Depending on whether the vehicle is used off-road or on-road, the terrain on which it operates could range from a hard surface to deformable surfaces, such as soils and snow. It is well known that soft terrain characteristics have a significant impact on off-road vehicle performance, development of a reliable and robust tire-terrain interaction model is vital. The tire modeling techniques as well as the modeling and validation methods used for developing FEA) tire models were discussed in details. The techniques used for soil modeling and calibrations such as FEA and Smoothed Particle

Hydrodynamics (SPH) were also discussed. In addition, the tire-terrain contact algorithm, the tire performance analyses under different operating conditions were further discussed.

From the review of reported studies, it is concluded that the cornering characteristics of tires operating on soft soils have not been comprehensively studied. The effects of variations in important operating parameters, in particular, have not been adequately addressed. Considering that compressive FEA tire models and SPH modeling techniques for soils have been well developed, these could be applied to gain insight into the roles of important operating conditions and soil properties. These include the rolling speed, inflation pressure, wheel load, and tire slip angle, in addition to soil characteristics such as cohesion, angle of internal friction, and sinkage. The implementations of these models in total vehicle performance analyses, however, have been limited due to the associated excessive computational demands. It is thus desirable to formulate relationships for cornering force and rolling resistance as functions of the operating parameters, which would permit vehicle performance analyses considering tires' interactions with different soils. Formulations of such relationships constitutes the primary motivation for this study, which are developed using an advanced algorithm involving testing, training and validations. Moreover, the relations describing the important effects of many operating conditions such as free-rolling or driven, multi-pass, and soil compaction, would be highly desirable.

CHAPTER 3

TIRE MODELING AND MODEL VALIDATIONS

The studies reporting tire-terrain interactions generally focus on static and dynamic responses for limited ranges of design and operating factors. This is mostly due to the need for remodeling and in-part due to large computational demand. Furthermore, the performance assessments and designs of tires involve repeated field and/or laboratory tests, which are extremely costly and demanding on human resources. In recent years, the need to develop a virtual tire test platform has been broadly emphasized [El-Sayegh et al., 2019; Farhadi et al., 2019], which would permit performance assessments and initial stage designs in a cost-effective manner. Advancements in computing hardware and software have facilitated developments in a new generation of tire modeling techniques that could serve as the virtual test platform, and permit design and analyses of tire structure in a cost-effective manner. Furthermore, these would allow the effects of various structure- and material-related factors on static and dynamic properties of tires and the soils. The design of an effective virtual test platform tires operating on soft soils involves the development of a comprehensive FEA tire model and its integration with the SPH model of the soil.

This chapter describes the FEA model of a truck tire (Goodyear RHD 315/80R22.5), which is implemented to the SPH soil model (Chapter 5) to investigate tire-terrain interactions under varying operating conditions and soil types. A comprehensive FEA model of a truck tire, developed by Slade [2009] in the Pam-Crash visual environment, has been adopted in this study for its integration to the soil models. The model validity, however, is thoroughly examined prior to its integration. This chapter describes different static and dynamic tests used for model verification. These include the vertical stiffness, footprint, and drum-cleat tests. The model validity is demonstrated by comparing the static and dynamic responses of the model with the available measured data for the same tire under different inflation pressures and vertical loads.

3.1 FEA truck tire modeling

A truck tire (Goodyear RHD 315/80R22.5) is considered for developing the FEA model. This particular tire was selected for the study due to the fact that the experimental data were accessible for examining model validity. The tire model was developed using the essential geometric and material data obtained from the manufacturer, as reported in [Slade, 2009; Chae, 2006], which are presented in Figure 3.1 and Table 3.1.

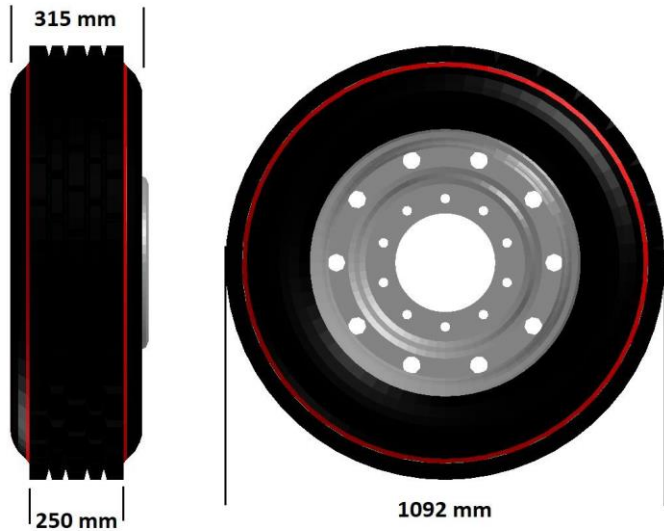


Figure 3.1. FEA tire basic dimensions [Chae, 2006]

Table 3.1. RHD tire specifications [Chae, 2006]

Tread Depth	27 mm
Rim Width	229 mm
Rim mass (m_a)	34.8 kg
Tire mass	72 kg
Mass of the wheel	106.8 kg
Mass of Belt (m_b)	43.4406 kg
Overall Width	315 mm
Overall Diameter	1092 mm
Static Loaded Radius	505 mm
Speed Rating	120 km/h
Rated Inflation Pressure	848 kPa (123 psi)

The tire is modeled in a visual environment called PAM-Crash that enables the modeling of complex geometry by offering different structural and continuum elements such as beams, shells, membranes and solids. Figure 3.2 shows half of the 3-dimensional tire cross-section that was generated in PATRAN. To produce a complete cross-section, this half model was mirrored about the tire's longitudinal axis. The cross-section was then rotated in 6 degree increments about the tire axle axis to form the entire tire with 60 identical sectors [Slade, 2009]. The tire carcass is made up of layered membrane components, while the bead fillers, shoulder region, tread, and under tread are made up of Mooney-Rivlin elements. Three separate layers of the layered membrane elements in the same component were considered that altered the material characteristics and orientations. The tire carcass structure in this case comprised rubber tire carcass as well as steel belts and steel wires, which extended radially from bead to bead within the carcass. The tire bead is represented as a circular beam element with a specific cross-sectional area and steel characteristics.

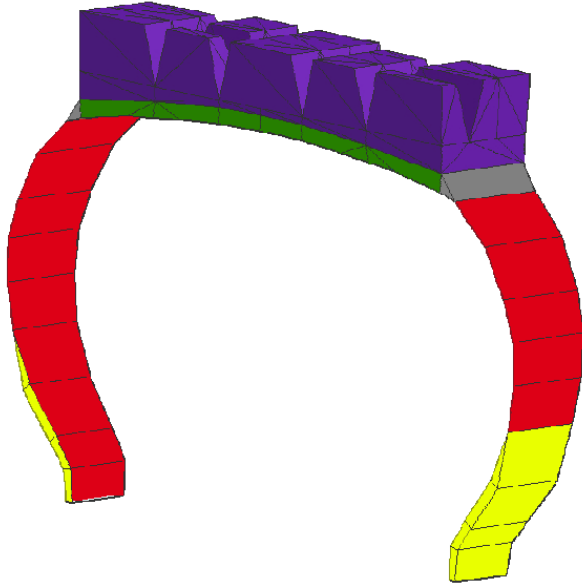


Figure 3.2. RHD tire section [Slade, 2009]

The RHD truck tire is made up of 21 parts, which are connected with each other and having 31 different material characteristics. The tire model has 4200 solid elements, 1680 membrane elements and 120 beam elements. The RHD tire has an asymmetric tread pattern that helps to keep gravel out of the tread. The tread design was reduced to include only the essential parts while reducing modeling complexities and computational demand.

The tread, under-tread, shoulders, and bead fillers are all represented as solid elements. Three-dimensional solid elements are used to represent these components since these are composed of rather thick rubber and are subjected to shear loads and abrupt changes in curvature during operation.

3.1 Tire model validations

There are several critical tire properties that must be precisely matched in order to produce the desired tire responses. The sidewall thickness (h), the modulus of elasticity (E) of the sidewalls and under-tread, and the Mooney-Rivlin coefficients of the rubber compounds of the tread and under-tread were all taken as reported by Slade [2009], which showed acceptable vertical stiffness compared to the published data [Lardner, 2017]. The vertical stiffness and contact patch area are among the static parameters utilized for calibration and validation in this case. The vertical and horizontal vibration mode frequencies are considered for validating the tire model in terms of its dynamic behaviour.

3.1.1 Vertical stiffness test

The vertical stiffness test is initially used to fine-tune the tire model to fit the measured load-deflection curves. The RHD tire model is positioned on a rigid surface and constrained along the lateral, longitudinal and all rotational directions. The tire is then inflated to a desired inflation pressure and a vertical load is applied to the rim in a ramp manner, as shown in Figures 3.3 and 3.4, until the target load of 40 kN is achieved. The tests were performed for three different inflation pressures, namely, 586, 758 and 896 kPa (85, 110 and 130 psi). Figure 3.5 shows the static load-deflection responses of the model for the three different inflation pressures. The results suggest linear vertical stiffness, defined as the slope of the force-deflection curve. Table 0.2 summarizes the vertical stiffness of the FEA tire model under the selected inflation pressures, which are also compared with those reported for a Goodyear truck tire by Hiroma et al. [1997]. The comparisons suggest reasonably good agreements between the model-predicted and reported vertical stiffness data. The peak difference between the two was observed to be in the order of 2.3% for 586 kPa (85 psi) inflation pressure and 3.1% for 758 kPa (110 psi) and 896 kPa (130 psi) inflation pressures.

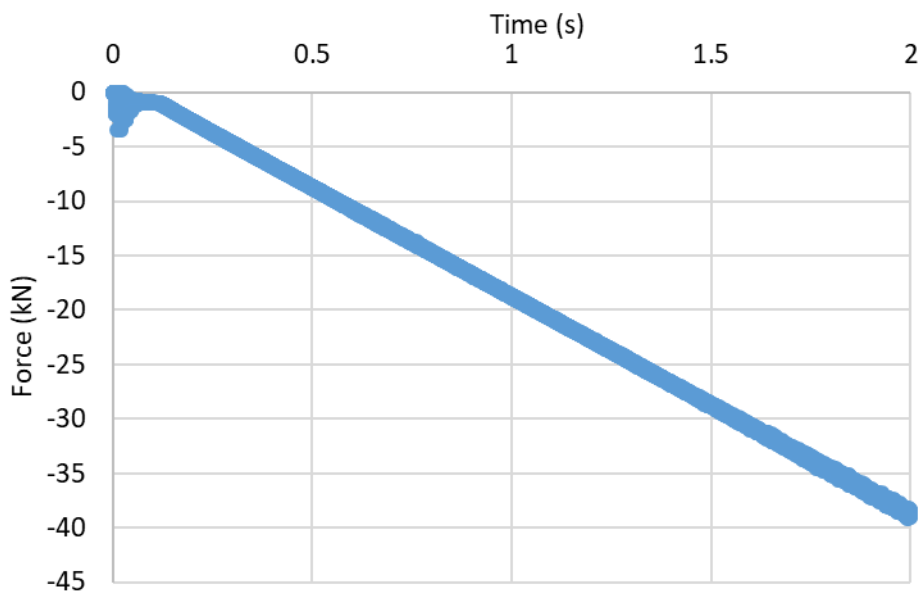


Figure 3.3. The ramp vertical load applied to the rim of the tire model

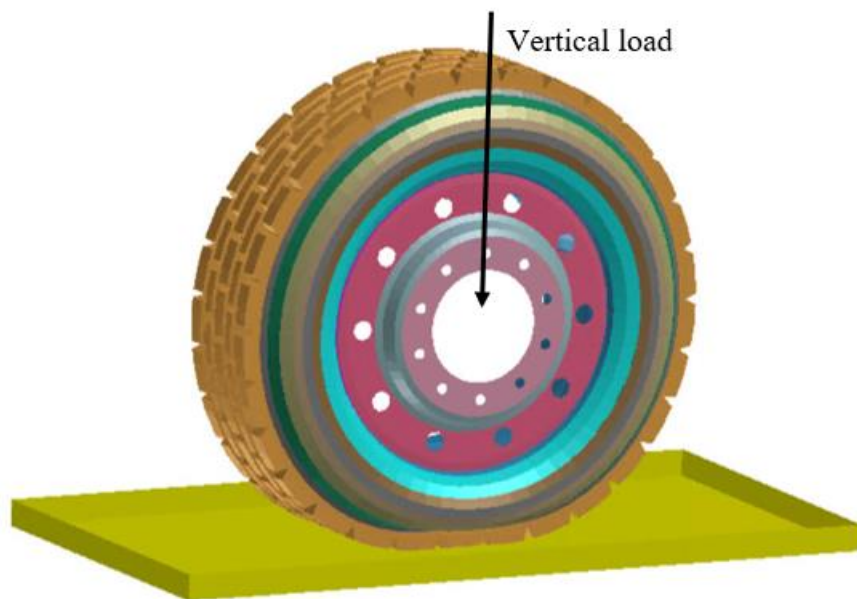


Figure 3.4. Vertical stiffness simulation test of the tire model

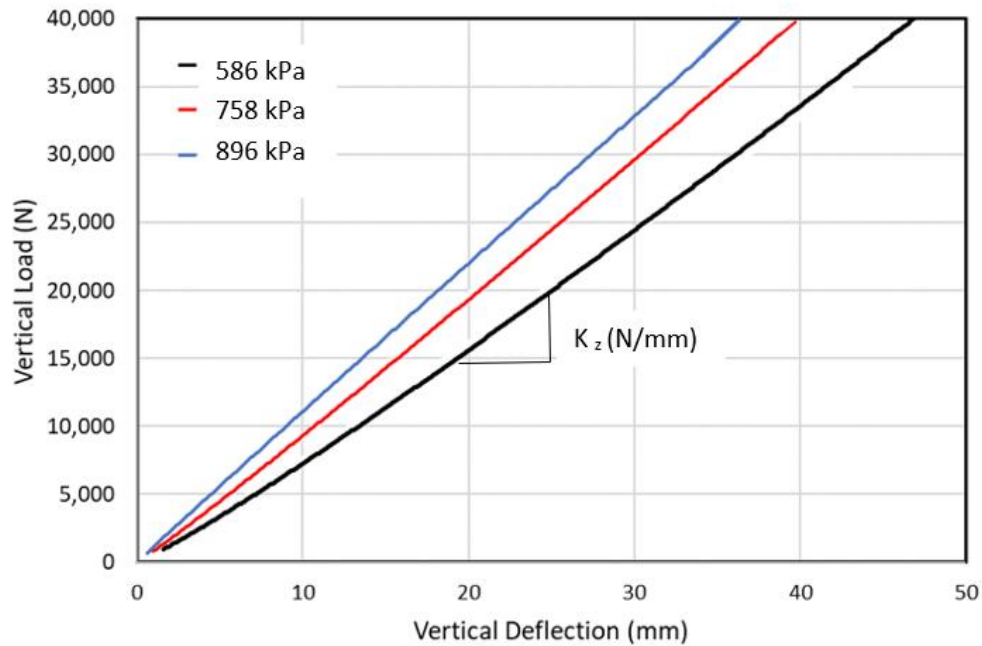


Figure 3.5. Load-deflection responses of the RHD truck tire model under different inflation pressures

Table 3.2. Comparisons of model-predicted vertical stiffness of the tire model with the reported data [Hiroma et al., 1997] for different inflation pressures

Inflation pressure	586 kPa (85 psi)	758 kPa (110 psi)	896 kPa (130 psi)
Model-predicted vertical stiffness (kN/m)	813	985	1120
Reported vertical stiffness of a Goodyear RHD tire	794	952	1085

3.1.2 Footprint test

The static footprint test is conducted to further examine the model validity considering three different tire loads (13, 27 and 40 kN). For this purpose, the tire model supported on a rigid surface is constrained in all rotational directions as well as lateral and longitudinal directions. A static vertical load is subsequently applied to the tire after it has been inflated to a desired inflation pressure. Stress contour in the Von-Mises direction is used to estimate the contact area, as shown in Figure 3.6. Figure 3.7 illustrates the variations in the footprint

area of the tire model for the three tire loads and constant inflation pressure of 758 kPa (110 psi). The model responses are also compared with the measured data obtained from the Goodyear Tire & Rubber Co. [Chae, 2006]. The results show comparable trends but notable differences between the simulation results and measured data. The peak difference between the model and measured results is observed for the higher tire load (40 kN). The model results revealed contact area of about 540 mm^2 under the 40kN, which is 7% lower than the measured contact area. This is likely due to low resolution of the model, which was realized considering 60 circumferential sectors. The prediction error could be reduced by formulating a more refined model with 120 or 180 circumferential sectors.

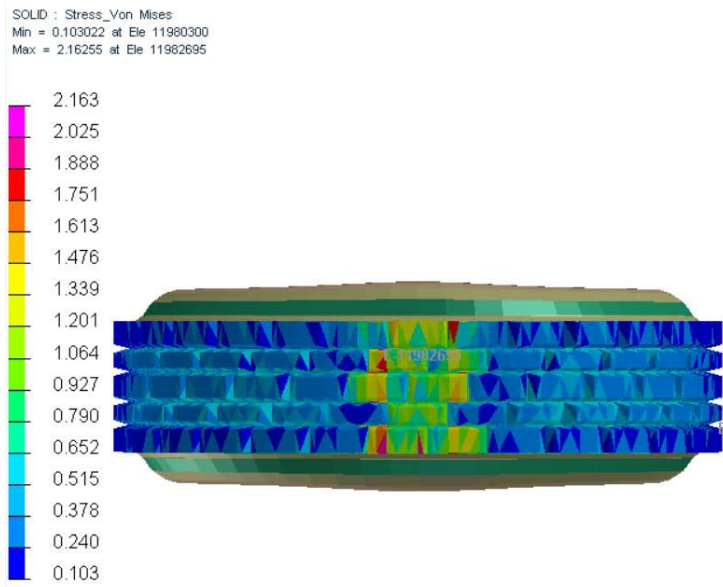


Figure 3.6. Von Mises stress distribution over the contact area of the tire model (40 kN vertical load and 758 kPa (110 psi) inflation pressure)

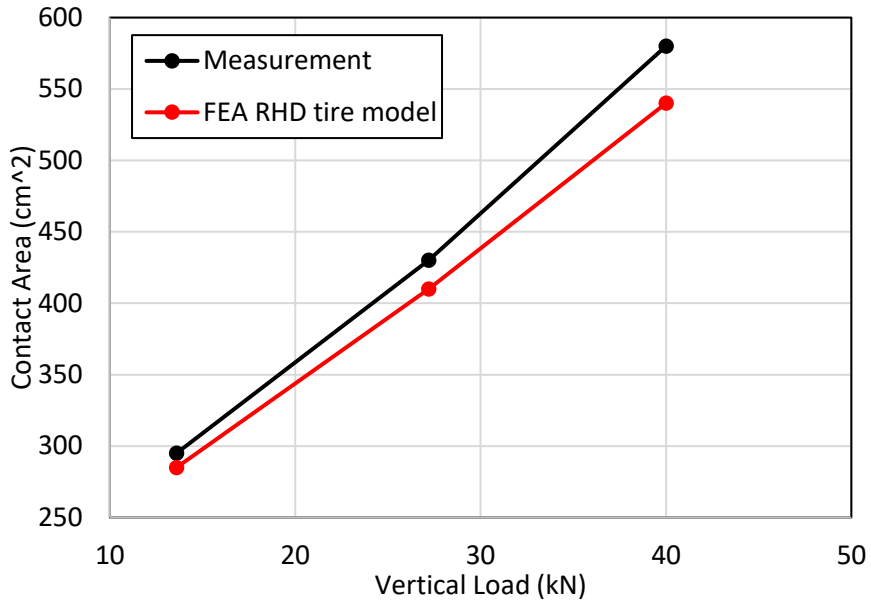


Figure 3.7. Comparison of contact areas obtained from the tire model with those reported for the Goodyear tire (Chae, 2006) for different vertical loads (inflation pressure: 758 kPa (110 psi))

3.1.3 Drum-cleat test

The dynamic drum-cleat test is performed to evaluate model validity in terms of fundamental vertical and horizontal vibration frequencies, which are considered critical dynamic features of the tire. In this test, the damping coefficient is taken as 5%, as reported by Chae (2006). Figure 3.8 shows the drum-cleat test for the RHD truck tire model subject to 40 kN vertical load and 586 kPa (85 psi) inflation pressure. The simulations were performed with a 2.5m diameter drum equipped with a 10mm-radius semicircular cleat, which serves as a vertical excitation leading to free vibration of the tire model. After inflating the tire to the desired inflation pressure, the tire is loaded by applying a vertical load to the rim. To detect the transmitted vertical force, the drum centre is constrained in all translational directions and is permitted to roll freely, while the tire spindle is also constrained in all translational directions. An angular velocity is applied to the drum's centre, allowing the tire to roll freely with equivalent forward speed of 50 km/h. The in-plane free vibration, and vertical and longitudinal force responses of the tire model are extracted for the given normal load and inflation pressure. The frequency spectra of force

responses, obtained using the Fast Fourier Transformation (FFT) technique, permitted the identifications of fundamental mode vibration frequencies.



Figure 3.8. FEA RHD truck tire model under the drum-cleat test

Figures 3.9 to 3.11 illustrate the spectra of free vibration responses of the tire model obtained from the drum-cleat tests for three different inflation pressures (586, 758 and 896 kPa), while the model is subjected to 40 kN vertical load. The vertical vibration spectra, invariably, exhibit a dominant peak near 2Hz, which corresponds to rolling speed of the drum. The second dominant peaks observed in the spectra correspond to the fundamental vertical and longitudinal mode frequencies. The fundamental mode frequencies tend to increase with increasing inflation pressure, as would be expected. The results suggest vertical mode frequencies near 53, 57 and 59 Hz, respectively, for tire inflation pressures of 586, 758 and 896 kPa (85, 110 and 130 psi). The corresponding longitudinal mode frequencies are observed near 52, 55 and 57 Hz. The spectra also exhibit second vertical mode frequencies near 64, 69 and 69 Hz, respectively, for the three inflation pressures. The observed fundamental mode frequencies of the FEA tire model are also summarized in Table 3.5 for different inflation pressures and given the vertical load of 40 kN, which fall within the range of frequencies reported for the radial-ply tires [Chae, 2006].

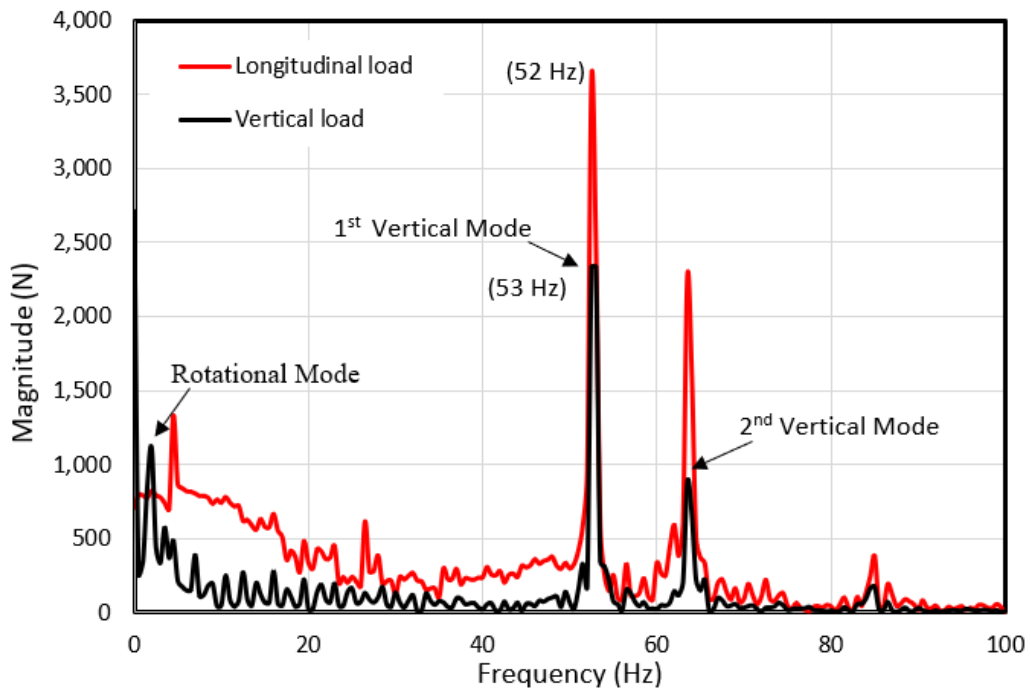


Figure 3.9. Frequency spectrum of vertical and longitudinal free vibration of the tire model obtained from the drum-cleat test (Tire load: 40 kN; inflation pressure: 586 kPa (85 psi))

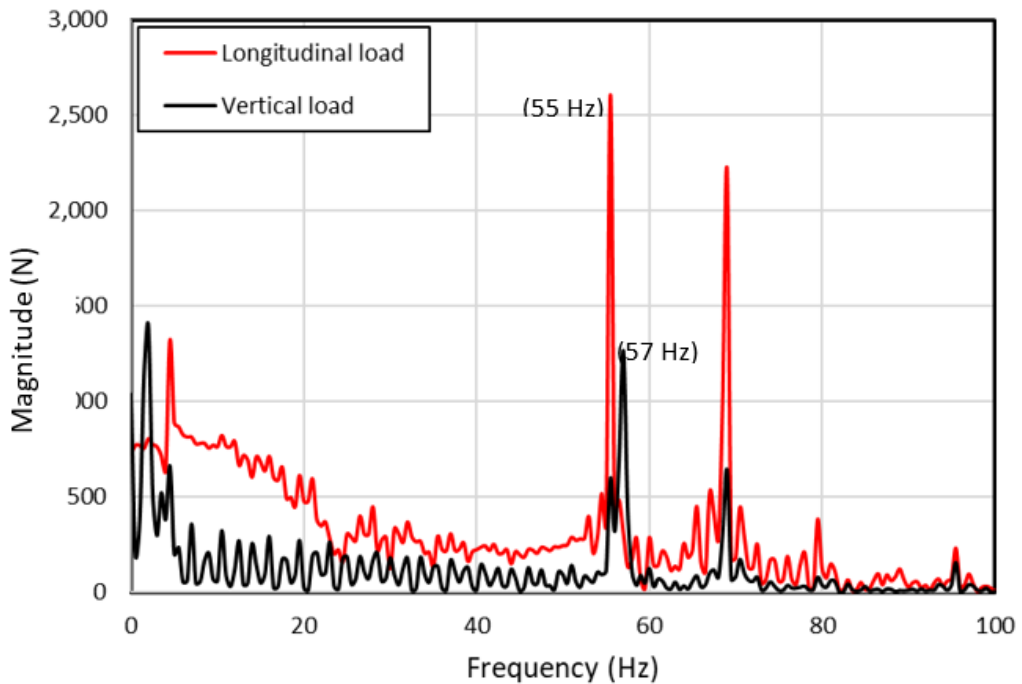


Figure 3.10. Frequency spectrum of vertical and longitudinal free vibration of the tire model obtained from the drum-cleat test (Tire load: 40 kN; inflation pressure: 758 kPa (110 psi))

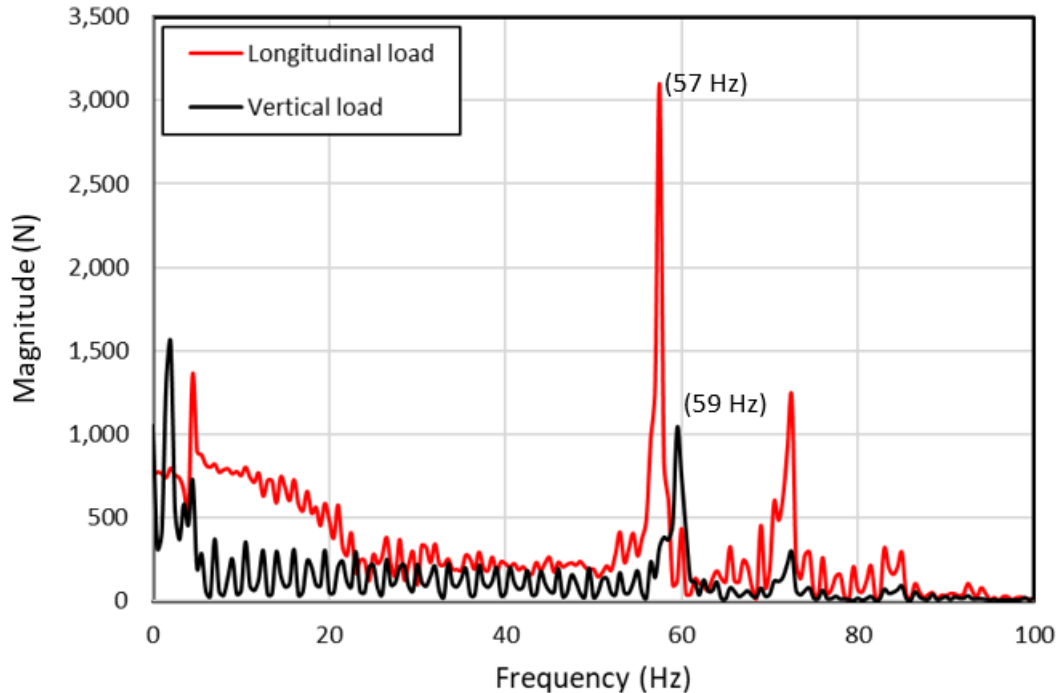


Figure 3.11. Frequency spectrum of vertical and longitudinal free vibration of the tire model obtained from the drum-cleat test (Tire load: 40 kN; inflation pressure: 896 kPa (130 psi))

Table 3.3. Fundamental vertical and longitudinal mode frequencies of the tire model for different inflation pressures (vertical load: 40kN)

Inflation pressure	586 kPa (85 psi)	758 kPa (110 psi)	896 kPa (130 psi)
Vertical mode frequency (Hz)	53	57	59
Longitudinal mode frequency (Hz)	52	55	57

3.2 Summary

- A FEA model of a truck tire is formulated and its validity is demonstrated through different static and dynamic tests, namely, the vertical stiffness, footprint and the drum-cleat tests. The static and dynamic responses obtained from the simulation

tests are compared with the available data of the same tire considering different inflation pressures and normal loads. It is shown that the model can predict the static and dynamic responses reasonably well for the ranges of inflation pressure and normal load considered. From the results, it is deduced that: the tire vertical stiffness increases as the inflation pressure increases. The vertical stiffness increased from 784 kN/m to 1244 kN/m, when the inflation pressure was varied from 586 kPa (85 psi) to 896 kPa (130 psi).

- The fundamental mode of vertical vibration of the tire model occurred in the 53-59 Hz frequency range with inflation pressure ranging from 586 (85 psi) to 896 kPa (130 psi).
- The fundamental mode of longitudinal vibration occurred at a slightly lower frequency and it increased from 52 and 57 Hz when inflation pressure was increased from 586 kPa (85 psi) to 896 kPa (130 psi).
- The fundamental vertical and longitudinal mode frequencies increased with the tire inflation pressure.

CHAPTER 4

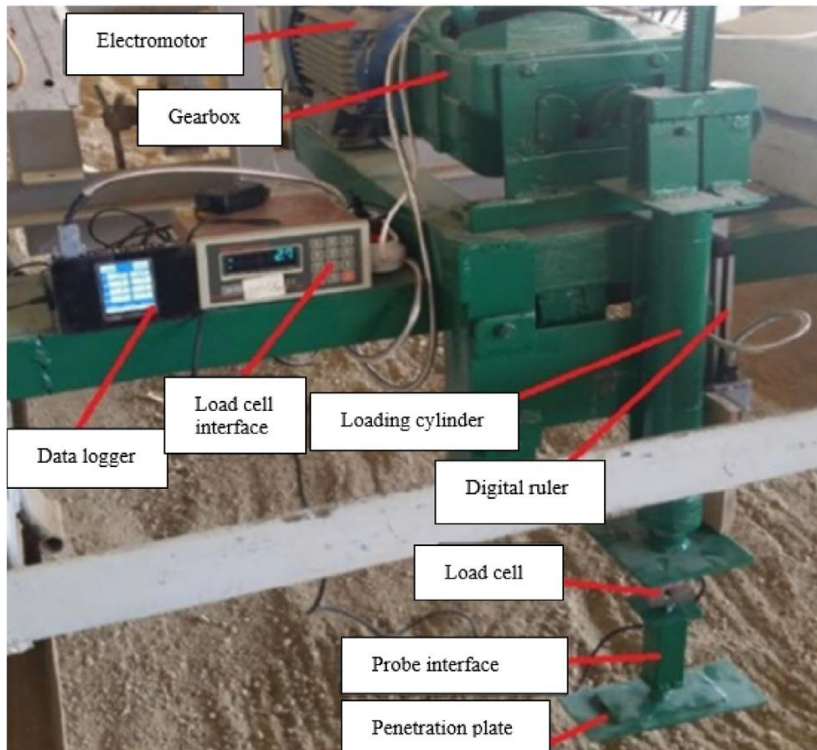
SOIL MODELING

This chapter describes the formulations of soft soil models using smoothed particles hydrodynamic (SPH) technique. The calibrations of the models are performed using the available data for different soils, namely, dry sand, moist sand, and sand loam soils. Experiments were performed to characterize the properties of new type of clay loam soil and the data are used to formulate a model for this soil. The chapter further presents test methods used for model calibrations and validations. The validated soil models are integrated with the FEA tire model to obtain virtual test platforms for predicting tires' interactions with soft soils considering different soils' properties and operating conditions.

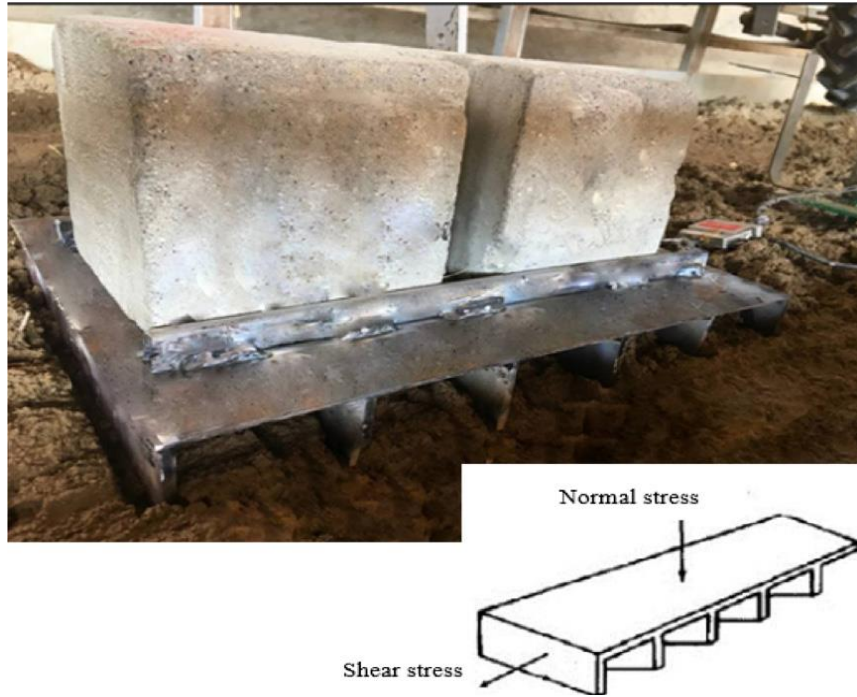
4.1 Experimental characterization of a clay loam soil

The experimental characterization of clay loam soil was undertaken using the plate penetration tester and shear strength box, as shown in Figure 4.1 [Bekker, 1969; Gheshlaghi et al., 2020c]. The soil tests were performed using a portable bevameter in a shear box in the spacious soil storage facility of the Therramechanics laboratory in Urmia University, Iran. The soil bin used for the experiments was 2 m wide, 23 m long, and 1 m in depth. The bin was equipped with rails that permitted guidance for the carrier and the tester. The portable plate penetration tester was mounted on the carrier, which could be moved along the soil bin width, as shown in Figure 4.1(a). The power required to penetrate the loading plate into the soil was provided by a 5.5-kW electric motor, gearbox, and the shoulder gear. A 300 mm × 100 mm rectangular plate was inserted into the probe interface at the location of the penetration plate, as in Figure 4.1(a). The rectangular plate size was chosen to represent the contact area between the tire and the ground. The test setup also permitted to measure the pressure-sinkage on compacted soil during subsequent passes. The aspect ratio of the rectangular plate was also selected according to the standards used in the Bekker model [Van et al., 2008]. The shear test box was designed and manufactured for the study to measure terrain strength parameters, as shown in Figure 4.1(b). The penetration force was measured through a 500 kg S-shaped load cell, which was acquired in the data acquisition system. The plate sinkage was measured using a digital ruler (model MLC320)

with a ± 1 -pulse reproducibility accuracy that was attached to the driven part of the device. The shear plate was pulled by the carrier at a constant speed of 0.2 m/s and the pulling force was measured by the load cell. The penetration force, the pull force and displacement signals were acquired in a data acquisition system. The vertical force acting on the shear box was varied by changing the weight and the shear strength parameters were subsequently using the Mohr-Coulomb criterion [Wong, 2008]. The experimental pressure-sinkage and shear-strength curves are shown in Figures 4.4 and 4.5.



a. Plate penetration tester [Gheshlaghi et al., 2020c]



b. Shear strength box [Bekker 1969, Gheshlaghi et al., 2020c]

Figure 4.1. Plate penetration tester and shear test box used for the measurement of soil parameters

4.2 SPH soil modeling

The SPH technique is used to model different types of soils. In this technique, the soil particles are modeled using the FEA elements that are defined as rigid bodies. The mesh size used in FEA analysis is 25 mm. The center of each FEA square represented one SPH particle. Each soil particle is described by its three features, namely, the center of mass, volume, and the region of influence. The particle smoothing length to radius ratio is set to 1.2 with the max smoothing length of 100 mm and the minimum smoothing length of 1 mm. The contact type for the clay loam particles and the box is non-symmetric node-to-segment with edge treatment and a thickness of 5 mm. Figure 4.2 shows the FEA element conversion to SPH in an FEA rigid body box. The FEA soil penetration constraints are solved in the SPH model. The advantage of SPH is that the elements do not share nodes and thereby eliminate the limits imposed by neighboring elements. The SPH model thus allows for free mobility of particles to capture the soil flow accurately. The sponge effect found in the FEA model is therefore eliminated by the freedom of SPH components. Since

SPH, unlike FEA, enables penetration, it yields a more accurate portrayal of soil behaviour under pressure.

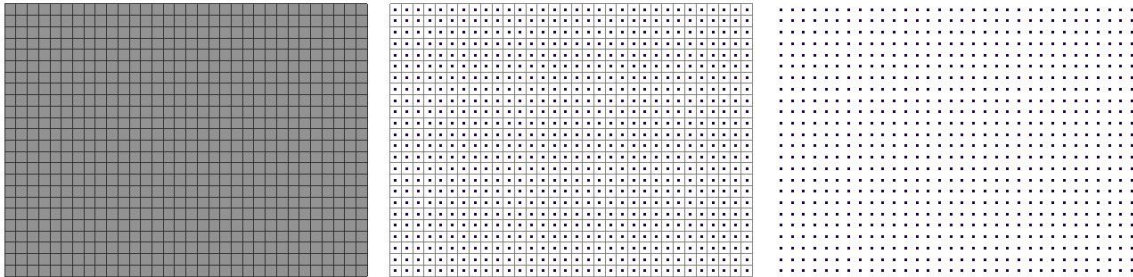


Figure 4.2. Converting FEA elements to SPH Particles

4.3 SPH sensitivity analysis

The SPH terrain behaviour is significantly impacted by the material characteristics employed. The material characteristics impact the property change in the pressure-sinkage and shear strength relationships. This section presents the sensitivity analysis performed for various parameters. The displacement speed in the shear-strength test, tangent modulus, yield stress, and the coefficient of the pressure-volume equation of state are among the parameters investigated.

Displacement speed in the shear-strength test

The displacement speed refers to how quickly the shear box is being dragged. It determines how rapidly the SPH particles move and react to a change in speed. Under constant material circumstances and SPH control parameters, three different speeds are examined to evaluate the effect of speed on soil behavior. To complete this test, a total movement of 10 mm is necessary. Thus, the box with a 10 mm/s speed moved for 1 second, the box with a 5 mm/s speed moved for 2 seconds, and the box with a 1 mm/s speed moved for 10 seconds.

Figure 4.3 shows the simulation results for the three boxes with three different speeds and measurements. Table 4.1 summarizes the parameters obtained from the simulation of the shear strength test at different speeds and experimental tests. The results show that the speed of the box has a minor impact on the shear strength relationship. Because the speed

increases by ten times between 10 mm/s and 1 mm/s, the cohesion changes by just 7% between 13.7 kPa (1.99 psi) and 14.86 kPa (2.15 psi).

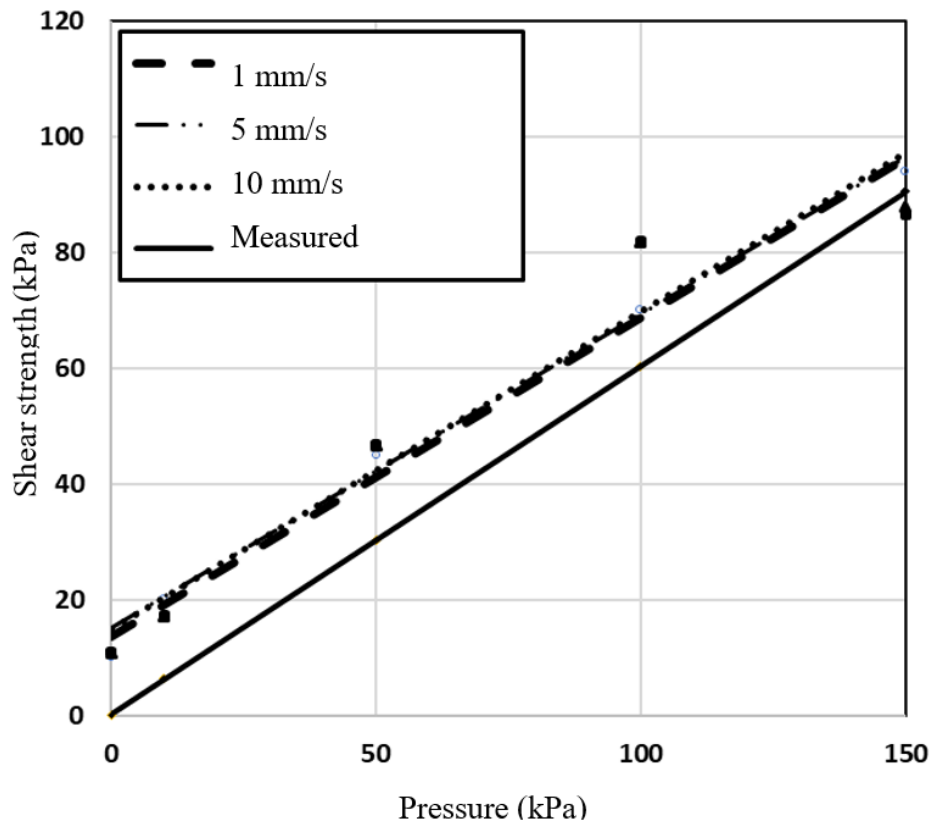


Figure 4.3. SPH soil shear-strength at different speeds versus measurements for clay loam soil

Table 4.1. Shear-strength test parameters of SPH soils at different speeds and measurements

	Measurements	1 mm/s	5 mm/s	10 mm/s
Cohesion (kPa)	0.3	13.71	15.1	14.86
Internal friction angle (deg)	30.51	28.76	28.36	30.51

Equation of state coefficients

Equation 4.1 shows the equation of state for a hydrodynamic elastic plastic material, which was employed in this study (Section 2.3).

$$P = C_0 + C_1\mu + C_2\mu^2 + C_3\mu^3 + (C_4 + C_5\mu + C_6\mu^2)E_i \quad (4.1)$$

The solution of equation 4.1 is based on the soil being modeled and calibrated. For the dry clay loam employed in this study, the parameter c_I is studied, with all other constants set to zero. Both the pressure-sinkage and shear-strength relationships are affected by this parameter. All soil parameters are maintained constant as in the prior test and only c_I is changed. The box moves at a speed of 5 mm/s for 10 seconds. For dry clay loam, three different c_I values were chosen: 2.5, 5, and 11 MPa. The results for pressure-sinkage and shear-strength are shown in Figures 4.4 and 4.5, respectively.

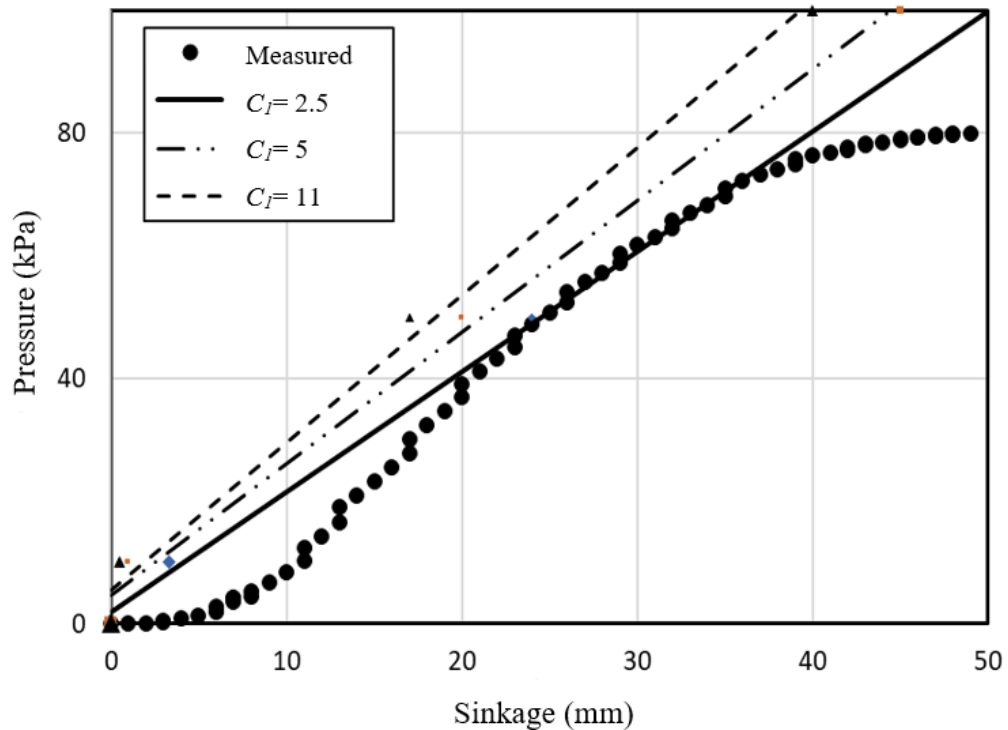


Figure 4.4. SPH soil pressure-sinkage at different c_I coefficients versus measurements for clay loam soil

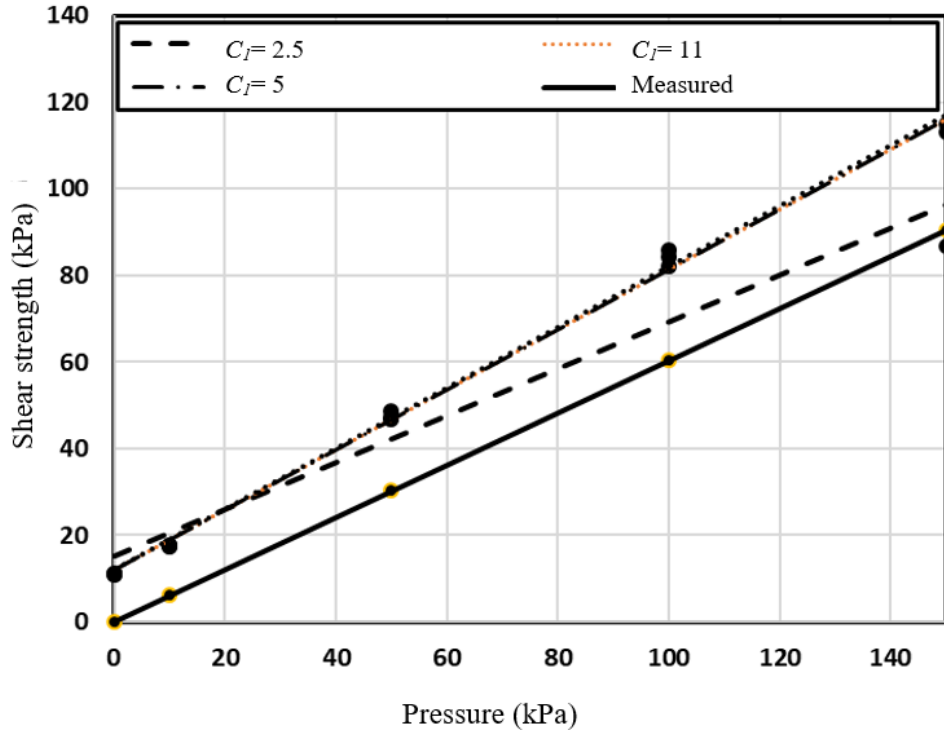


Figure 4.5. SPH soil shear-strength at different speeds versus measurements for clay loam soil

The results show that the value of c_1 has a significant impact on the sinkage of the soil. Sinkage reduces between 50 mm and 40 mm when c_1 increases from 2.5 MPa to 11 MPa. The internal friction angle increases between 28.36 and 34.1 degrees as c_1 increases between 2.5 and 11 MPa. c_1 affects the stiffness of the material. For example; a lower number of results in a softer material, which sinks more. 2.5 MPa is chosen as the optimal value of c_1 that results in pressure-sinkage and shear-strength curves near the measurement curves.

Yield stress

Yield stress is the stress that corresponds to the yield point at which the material begins to bend plastically. Since it reflects the top limit of forces that may be applied without causing permanent deformation, the yield stress is commonly employed to estimate the maximum permitted load in a mechanical component. The yield stress has a minor effect on the shear-strength relationship, according to many simulations performed using the shear box test. The pressure-sinkage relationship, however, is significantly affected. The yield stress was

varied to 0.02, 0.09, 0.15, and 0.2 MPa throughout this test, with all other parameters held constant. The pressure-sinkage relationship for various yield stresses is shown in Figure 4.6. The effect of yield stress is comparable to that of the equation of state coefficient. The sinkage reduces between 52 and 6 mm when the yield stress increases between 0.02 and 0.2 MPa. In another word, as the yield stress increases, the material becomes denser. In the dry clay loam, the optimal yield stress value is set to 0.02 MPa, which is the closest to the measurement.

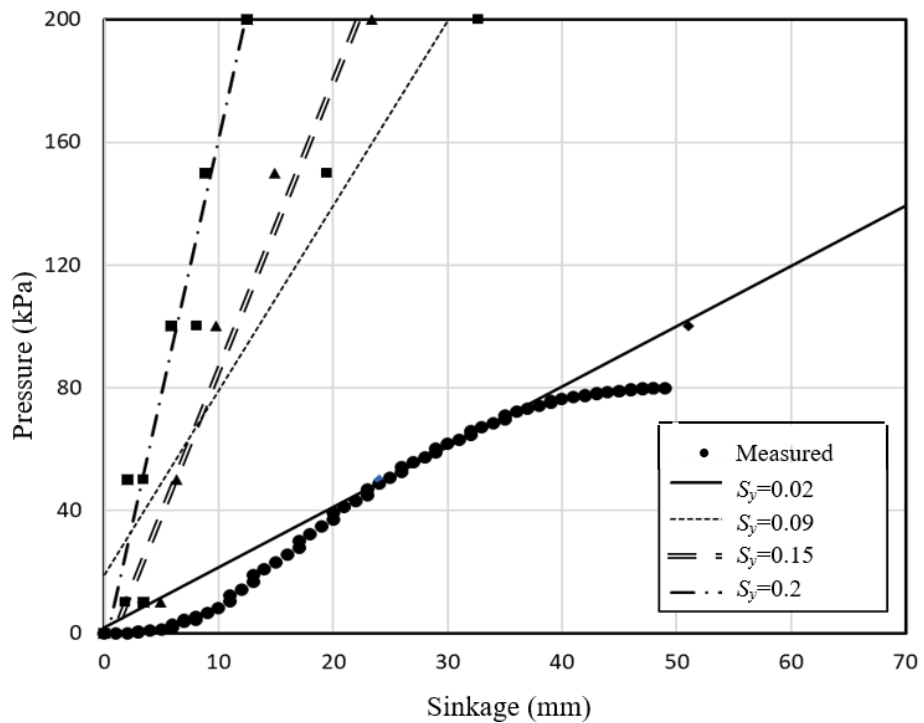


Figure 4.6. SPH soil pressure-sinkage at different yield stresses versus measurements for clay loam soil

Tangent modulus

The tangent modulus is the slope of the stress-strain curve at any specific point. The tangent modulus is equal to Young's modulus below the linear elastic regime. The tangent modulus can be used to describe the behaviour of materials that have been strained outside of their elastic range. In another word, the tangent modulus measures the material's "softening" or "hardening" when it begins to yield. In this test, the tangent modulus is adjusted while all other parameters are maintained constant. This test was performed on clay loam for 10 seconds at a constant displacement speed of 5 mm/s. Different tangent

moduli with magnitudes of 0.4, 0.35, 0.3, and 0.2 MPa are investigated. Figure 4.7 shows the results of the shear-strength tests for simulations and measurements. As the tangent modulus increases the shear strength increases at a constant pressure that results in an increase in internal friction angle. The most optimal tangent modulus according to the shear-strength simulations is 0.25 MPa

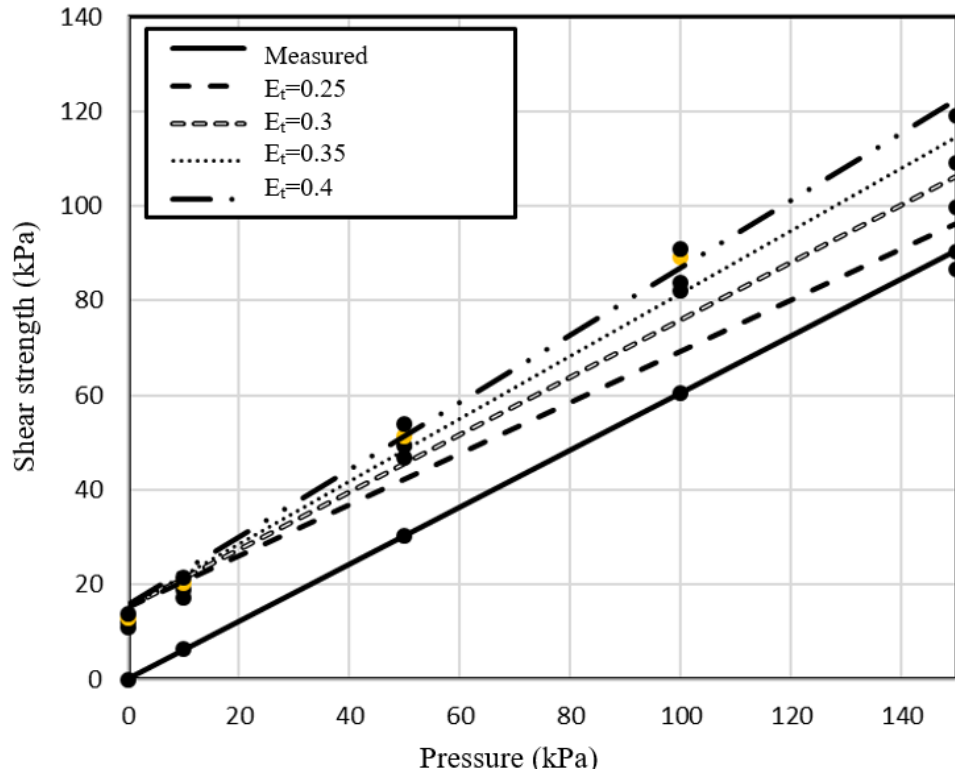


Figure 4.7. SPH soil shear-strength at different tangent moduli versus measurements for clay loam soil

4.4 SPH soil model calibrations

The SPH soil models are formulated considering isotropic-elastoplastic-hydrodynamic materials. The models are formulated for different soils, namely, clay loam, clayey soil, dry sandy loam, 10% moist sand, 25% moist sand, and 50% moist sand. Table 4.2 lists the material characteristics of clayey, clay loam and dry sandy loam soils, which were obtained from reported studies [Gheshlaghi et al., 2020; El-Sayegh, 2020]. These soil parameters are incorporated into the soil definition in order to calibrate the soil conditions. The pressure-sinkage and direct shear stress tests were performed using the SPH models in order to obtain the soil properties, which are described below.

Table 4.2. Material properties of SPH soils [Gheshlaghi et al., 2020; El-Sayegh, 2020]

Soil Type	Tangent modulus (MPa)	Mass density (ton/mm ³)	Shear modulus (MPa)	Yield stress (MPa)
Clayey	0.025	2E-9	23	0.04
Sandy-loam	0.3	1.696E-9	15	0.016
Clay loam	0.25	1.44E-9	7	0.02

4.4.1 Pressure-sinkage test

Figure 4.8 shows the pressure-sinkage test carried out by applying a known pressure (between 0 to 200 kPa) to a circular plate (150 mm radius) placed on the soil. The沉降 of the plate into the soil is subsequently evaluated to obtain the pressure-sinkage relationship for the soil. Bekker's formulation is used to express the pressure applied on the plate as a function of plate沉降 [Bekker, 1950].

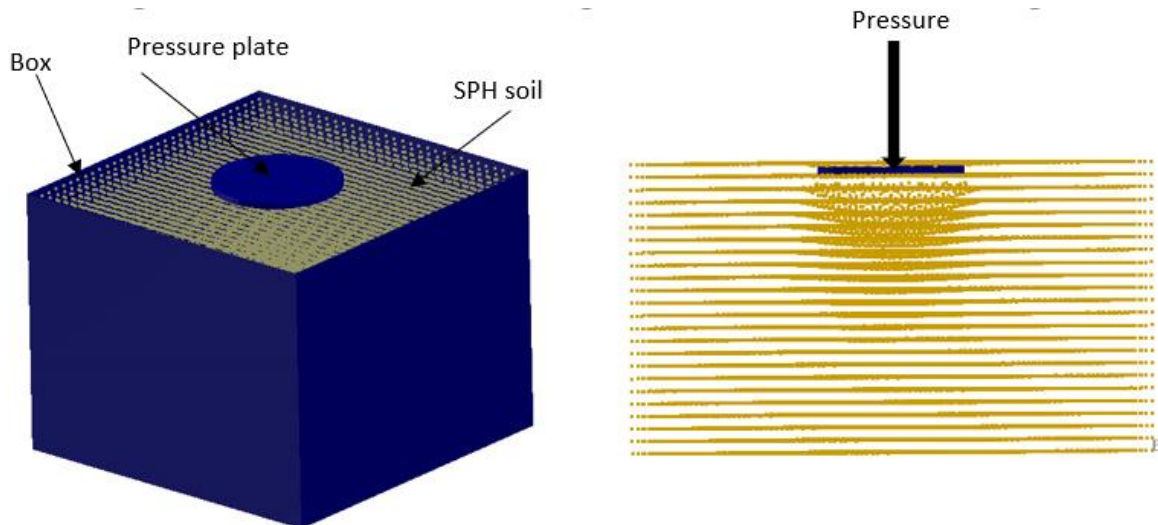


Figure 4.8. SPH soil pressure-sinkage test

$$p = \left(\frac{k_c}{b} + k_\phi \right) z^n \quad (4.2)$$

Where p is the pressure, b is the circular plate radius, z is plate沉降, and n , k_ϕ , and k_c are soil characteristics derived from published terramechanics data [Wong, 2001]. The pressure-sinkage relationship obtained from the soil model is compared with the measured

data to examine the validity of each soil model, as shown in Figure 4.9. The figure also presents the relationship obtained from Bekker's formulation. The results suggest that the SPH model can predict the plate sinkage reasonably well under plate pressure up to 80 kPa (12 psi). Under the 80 kPa (12 psi) pressure, the model predicts sinkage of 41.3 mm, which is approximately 10.8% smaller than that obtained from the experiments for the clay loam.

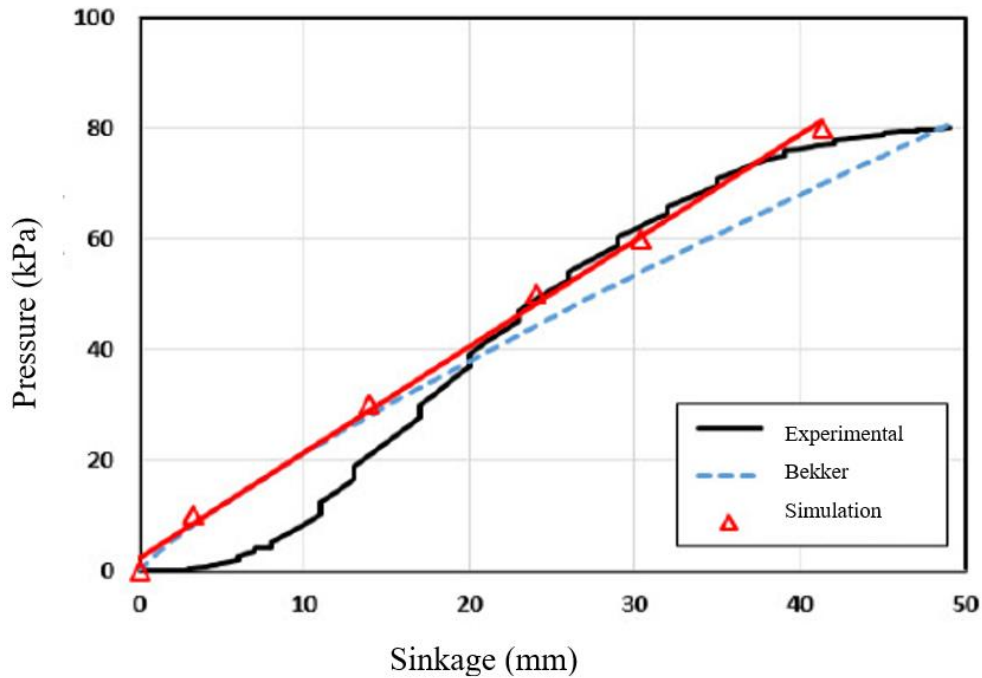


Figure 4.9. SPH soil pressure-sinkage versus measurements for clay loam soil

4.4.2 Shear strength test

The shear strength test is carried out by filling a soil domain within a rectangular box, as shown in Figure 4.10. The box is made up of three parts: a top pressure plate where pressure is applied, an upper box that can slide, and a fixed bottom box that is locked in all orientations. A continuous pressure is supplied to the top pressure plate's center, followed by a 10 m/s displacement of the upper box and top plate. The resulting shear force is used to derive the shear stress relationship.

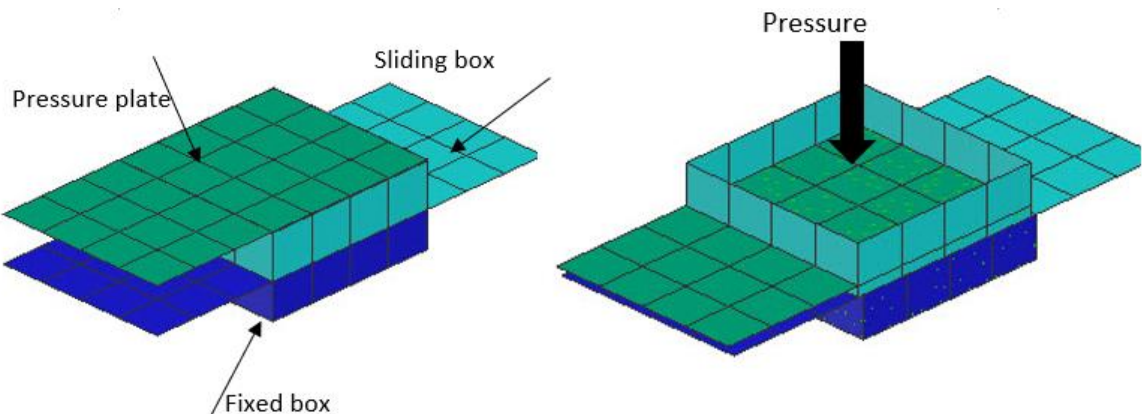


Figure 4.10. SPH soil shear strength test

The soil shear properties derived from the shear-stress relationship are calibrated against the Mohr-Coulomb failure relations, given by:

$$\tau = \tau_{\max} \left(1 - e^{-\frac{j}{k}} \right) = (c + p \tan \phi) \left(1 - e^{-\frac{j}{k}} \right) \quad (4.3)$$

$$\tau_{\max} = (c + p \tan \phi) \quad (4.4)$$

where, τ_{\max} is the maximum shear stress, ϕ is the internal friction angle of soil derived from reported measured data [Gheshlaghi et al., 2020; El-Sayegh, 2020], j is the shear deformation in mm, and k is the displacement modulus in kPa. The shear stress response obtained from the dry clay loam soil model is compared with the measured data to examine model validity. Figure 4.11 compares the model-predicted shear stress response as a function of applied pressure for the dry clay loam soil with the reported measured data. The angle of internal friction and soil cohesion is determined from the angle of the shear curve and the intersection of the curve with the shear strength axis, respectively. The model-predicted shear properties including the soil sinkage exponent for dry clay loam soil are compared with the reported measured values in Table 4.3. The simulation results obtained for the dry clay loam soil revealed an internal angle of 28.42, which is quite comparable with the report measured value of 30.51 degrees. The shear properties for other soil models that were previously modeled and calibrated [El-Sayegh, 2020] are shown in Table 4.5. The results showed that the predicted shear strength behaviours of the soils were in reasonably good agreements with the reported experimental data [Gheshlaghi et al., 2020; El-Sayegh, 2020].

In addition to the similarity of the behavior and characteristics of the tested soil and the calibrated soil shown in Figure 4.11, more detailed results in Table 4.3 demonstrate that the SPH technique holds the reasonable capacity to predict soil parameters.

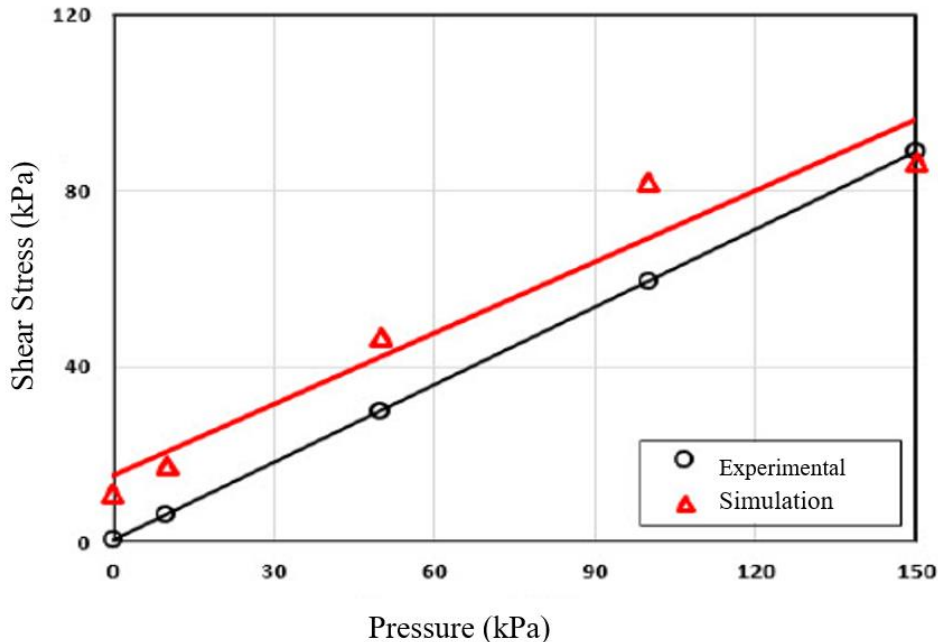


Figure 4.11. SPH soil shear-strength test versus measurements for the clay loam soil

Table 4.3. Predicted and measured shear properties of clay loam soil parameters

Clay loam soil		Cohesion (kPa)	Internal friction angle (deg)	Soil sinkage exponent
	Simulation	1.143	28.42	0.86
	Measured [Gheshlaghi et al., 2020]	0.3	30.51	0.84

4.5 Soil model characteristics

The calibrations were formed for the SPH models formulated for different soils. These included the models for relationships for the tire-soil interaction dry clay loam, clayey soil, dry sandy loam, 10% moist sand, 25% moist sand, and 50% moist sand. The soil models

are used to develop essential relationships describing the tire-soil interactions. The validity of the relationships for the tire-soil interaction, however, was conducted using mud soil (uplands sandy loam with 51% moisture content). The purpose of using mud was to test the proposed model with a soft soil whose mechanical characteristics are similar to those of the soils used to develop the model. The material characteristics of the mud soil, obtained from reported studies [Wong, 2001] and presented in Table 4.4, are incorporated into the soil definition to calibrate the soil conditions.

It should be noted that the sand used to model the moist sand is classified as poorly-graded non-plastic sand in accordance with the USCS classification system [ASTM D2487, 2005]. The maximum dry density and optimum moisture content of the soil were measured as 1850 kg/m³ and 10%, respectively, in accordance with the Standard Proctor test [ASTM D698, 2005]. The particle size distribution for the soil was determined in accordance with ASTM D422, [2005]. The soil contained approximately 5% very fine particles passing through 0.075 mm sieve. The soil parameters were subsequently obtained using the pressure-sinkage and shear-strength tests. Table 4.5 summarizes the soil shear resistance and cohesion coefficients obtained from the shear stress test for other soils used in this study that changes between 12 to 32.9 degrees and 0.7 to 15.7 kPa, respectively [El-Sayegh, 2020]. While the pressure-sinkage curves for the soils are presented in Figure 4.12. The soil sinkage increases with increasing applied pressure, however, the rate of increase in sinkage depends on the softness and hardness of the soil. Dry sand with a 160 mm sinkage and 10% moist sand with a 18 mm sinkage at 200 kPa (30 psi) is the softest and hardest soil, respectively used in this study. These soils were previously modeled and validated using experiments and published data [El-Sayegh, 2020]. The pressure-sinkage behaviour and shear stress characteristics for the modeled clay loam soil in this study were presented in sections 4.4.1 and 4.4.2, respectively.

Table 4.4. Material properties of SPH mud soil [Collings et al., 2021]

Soil Type	Tangent modulus (MPa)	Mass density (ton/mm ³)	Shear modulus (MPa)	Yield stress (MPa)
Mud	0.27	1.4 E-9	6	0.012

Table 4.5. Simulated soil characteristics.

Soil Type	Clayey loam	Sandy- loam	10% moist sand	25% moist sand	50% moist sand	Mud
Cohesion (kPa)	15.7	9.8	0.7	4	2.88	15
Internal friction angle (Deg)	12	29.4	21	21.36	30.19	32.9

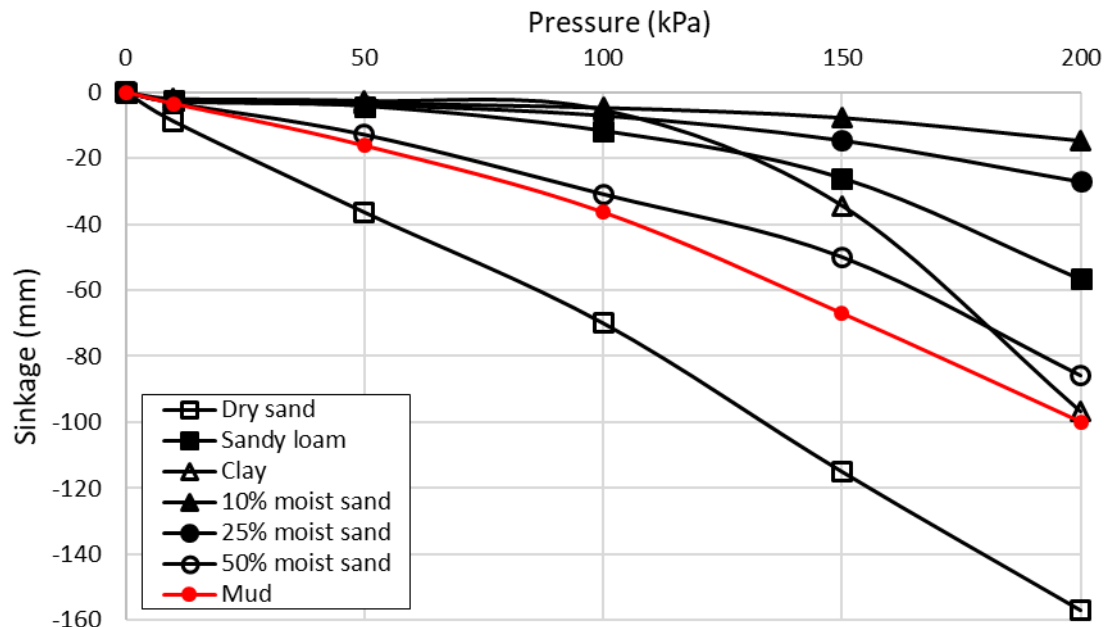


Figure 4.12. Simulated pressure-sinkage tests for different soils

4.6 Summary

This chapter described the primary features of soft terrain modeling and calibration techniques. Different soil types that are often utilized in the vehicle-terrain interactions were calibrated, which included clay loam, sand-loam, clayey soil, and moist sands. SPH method and hydrodynamics-elastic plastic material were used to simulate the soils. Two pressure-sinkage and shear-strength experiments were used to calibrate the terrains. The simulation findings were compared with the reported terramechanics measured data. Using Mohr-Columb failure criteria, the cohesion and angle of shear resistance were estimated and evaluated against published physical terramechanics parameters. The SPH soil models were found to be in good agreement with the measurements. The soil models are used to develop essential relationships for describing tire-soil interactions, while the mud soil is used to validate the developed relationships.

CHAPTER 5

TIRE-TERRAIN INTERACTIONS ANALYSIS: ROLLING RESISTANCE

5.1 Introduction

A rolling tire exhibits considerable rolling resistance, which contributes to substantial energy loss. Rolling resistance of a tire is primarily caused by hysteresis of the rubber tread and carcass that is encountered as the tire rolls through its footprint. The rolling resistance of a tire rolling on an undefeatable pavement is strongly affected by the material hysteresis and orientations of the high modulus cords in the layered carcass and belt structure, in addition to various operating factors such as rolling speed, normal load, inflation pressure and tread depth. Soil compression and shearing further contribute to the rolling resistance in a highly complex manner when the tire rolls on deformable terrains [Contreras et al., 2013]. For tires operating on non-deformable pavements, the tire's flexibility accounts for the majority of the rolling resistance. During soft soils operations, the soil deformations in both vertical and horizontal directions are the important contributory factors. The designs of tires and development operating practices leading to low rolling resistance have been widely emphasized for preserving the fuel economy of vehicles [Taghavifar and Mardani, 2013].

In this chapter, integrating the FEA tire model and the SPH soil model is used to evaluate rolling resistance of the tire. The results are employed to develop relationships for the rolling resistance using the genetic algorithm (GA), which is implemented to analyze rolling resistance of a vehicle. The first part of the chapter focuses on the analysis of rolling resistance under different operating conditions such as inflation pressure, vertical load, speed, torque, in addition to the soil characteristics. The second part of this chapter includes the development of a genetic algorithm model to derive a relationship describing the rolling resistance coefficient as a function of various operating conditions. These include the multi-pass, longitudinal speed, vertical load, inflation pressure, and soil characteristics. An experiment was designed to characterize rolling resistance of a RHD tire operating on mud soil. The tests were done with four different tires (one steered, two driven, and one push)

in an SPH soil bed at 10 and 15 km/h with different vertical loads (13 kN, 40 kN) and inflation pressures (379 kPa (55 psi), 758 kPa (110 psi)). The validity of the rolling resistance relationship is examined using the measured data for ranges of operating conditions.

5.2 Simulation model setup for tire rolling resistance analyses

Figure 5.1 shows the Volvo f-series medium 8*4 truck that is considered for the rolling resistance analyses. The vehicle is equipped with four axles, including a steered axle and two driven axles with air suspension. The vehicle specification is summarized in Table 5.1. The simulations are performed to assess the truck tire's traction in an off-road situation under different operating conditions. Considering the substantial computational demands of simulations involving 4 tires multi-pass models two different models were designed to predict the rolling resistance coefficient.

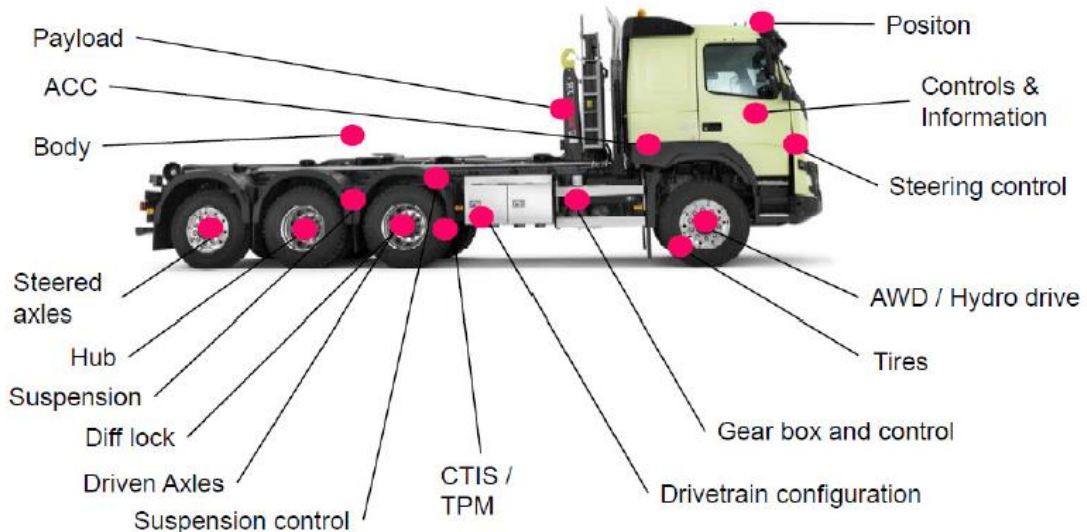


Figure 5.1. Schematic of the Volvo F-series medium 8*4 truck

Table 5.1. Vehicle specifications

Truck model	F-series medium 8*4 truck
Axles	2 driven, 1 steered, 1 tag
Suspension	Front: Lead mechanical; Rear: air
Gross combination weight	44 tonnes
Front axle load	8 tonnes
Rear axle load	27 tonnes
Power	450 HP

A tire-terrain interaction model is initially formulated to evaluate the rolling resistance coefficient (RRC) on soft soil, as shown in Figure 5.2. This model is designed solely to reduce the simulation time. The second model is subsequently formulated considering the 4 tire multi-pass interactions with the soil, as shown in Figure 5.3. The multi-pass model consists of two driven tires (tire-2 and tire-3) and two free-rolling tires (tire-1 and tire-4). The multi-pass model allows for the quantification of the effect of soil compaction on RRC. The rolling resistance simulations are performed under different operating and terrain conditions to determine their effects on the tire-terrain interactions. The tire-soil interaction contact algorithm employed the node symmetric node to segment with the edge treatment technique. Genetic Algorithm (GA) code is subsequently developed to derive a relationship between RRC and the operating parameters.

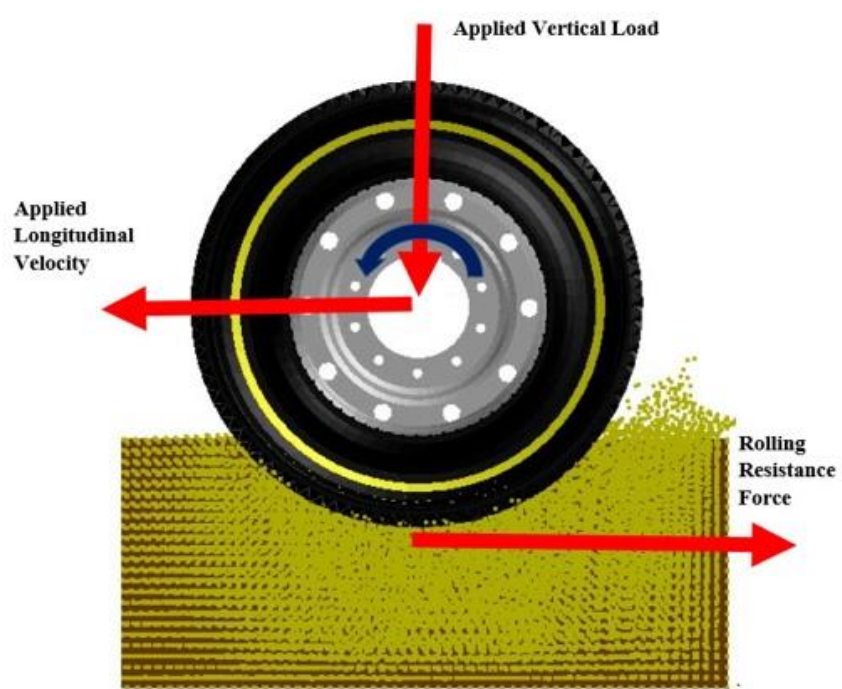


Figure 5.2. Model used to simulate tire's interactions with a soft soil (clay loam)

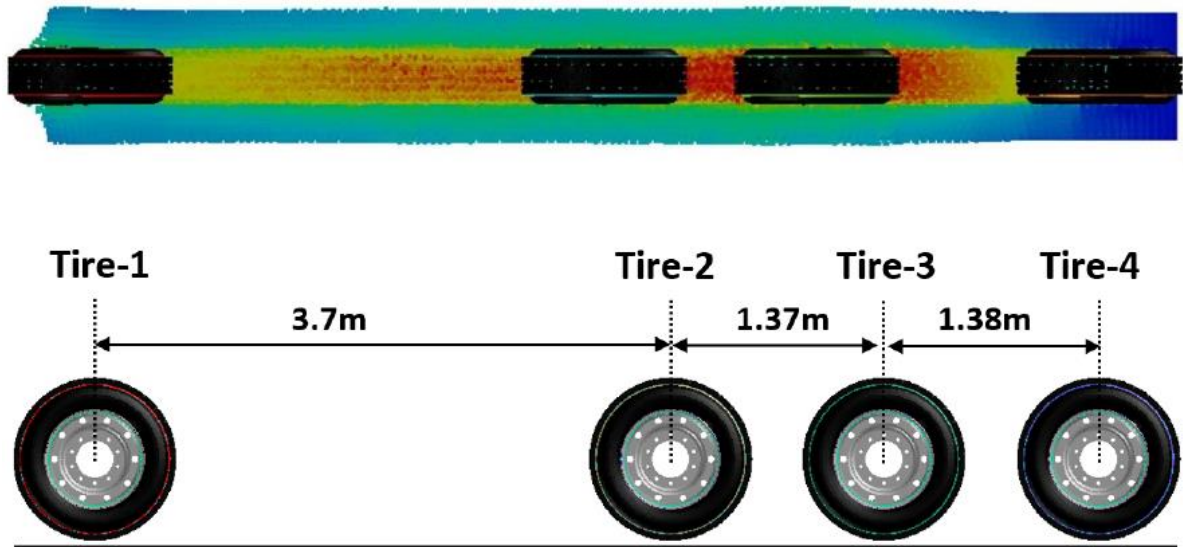


Figure 5.3. Multi-pass tire-terrain interaction model considering the four tires of a single vehicle track

For the rolling resistance simulations, a desired inflation pressure is initially applied to each tire together with a constant vertical load applied to the center of each wheel. Each tire is then allowed to settle on the terrain. The constant linear longitudinal velocity is

subsequently applied to the center of the free-rolling tire. An angular velocity is simultaneously applied to the center of each driven tire. The tires are then allowed to roll over the terrain for about 1.5 seconds to obtain steady motion at the tire-terrain contact patch. It should be noted that the simulation model consists of four tires running in a single run.

It should be noted that the total rolling resistance of an off-road tire comprises both the internal and external rolling resistances. The internal rolling resistance arises from the loss of energy attributed to deformations of the tire, while the external rolling resistance is due to energy loss associated with the deformation of the soil. In this study, the rolling resistance of the tire is evaluated in terms of the longitudinal force opposing the tire motion due to the deformation of the soil, which does not include the energy losses due to hysteresis and the thermal losses due to tire deformation.

To validate the simulation model, physical testing on gravelly soil was previously carried out at Volvo Group's Truck Technology center in Gothenburg, Sweden in 2018 [Zeinab, 2020]. The measurements included response and acceleration from the ground through the axle, as well as soil compaction and changes in ground properties after successive driving. The response parameters extracted from the simulation model to determine the RRC include the vertical load applied on the tire and the contact force between the tire and terrain in the tire's forward direction. The results showed that the tire-soil interaction model simulation is in good agreement with experiments [Zeinab, 2020].

5.3 Rolling resistance analyses

The simulations of different terrains include dry and moist sands, a clayey soil, and a dense sand. The simulations are also repeated for different operating conditions. These included three different inflation pressures (379 kPa (85 psi), 586 kPa (110 psi), and 758 kPa (130 psi)), three different vertical loads (13 kN, 27 kN, and 40 kN), and three different longitudinal speeds (5 km/h, 10 km/h and 15 km/h). The simulation results are presented below and discussed to highlight the impacts of variations in the vertical load, inflation pressure, soil compaction, and soil mechanical properties on the rolling resistance. RRC is subsequently evaluated by normalizing the resisting force to the wheel load.

5.3.1 Effect of vertical load

Figures 5.4(a), 5.4(b), and 5.4(c) show the effects of variations in vertical load on the rolling resistance coefficient of the free rolling tire model coupled with the models of clay loam, dense sand, and clayey soil, respectively. The results are presented for a constant forward speed of 10 km/h and three different inflation pressures. The results suggest a nearly linear increase in RRC with an increase in vertical load, irrespective of the inflation pressure. This is due to greater sinkage of the wheel into the soil and higher tire-soil contact area under the higher wheel load. The interactions of the tire with clayey soil, however, yield slightly nonlinear effects of normal load on the resulting RRC. This is evident in Figure 5.4(c) for the higher inflation pressure.

The results exhibit significant effects of the soil on the RRC and its rate of change with the vertical load. The operation on the clay loam soil yields an almost linear increase in RRC with the vertical load, irrespective of the inflation pressure. The rate of change of RRC with the vertical load, however, tends to be considerably lower for the low inflation pressure of 380 kPa (55 psi). Lower inflation pressure also yields notably lower RRC for all the vertical loads considered, which is attributable to relatively lower wheel sinkage under the lower inflation pressure. The results suggest the lowest RRC of 0.226 corresponding to the 13 kN wheel load and 380 kPa (55 psi) inflation pressure, while the highest RRC of 0.269 is observed under the 40 KN load and 758 kPa (110 psi) inflation pressure. Similar trends in RRC are also observed for the tire's interactions with the dense sand and clayey soil, as seen in Figures 5.4(b) and 5.4(c). The RRC of the free rolling tire, however, is significantly higher during operation on the clayey soil. For the higher inflation pressure of 758 kPa (110 psi), the RRC increases from about 0.32 to 0.75, when the wheel load is increased from 13 kN to 40 kN. The results thus suggest that the tire's interactions with the clayey soil are far more sensitive to wheel load when compared to those with clay loam and dense sand which is due to the softness of the soil. The results also show that the rolling resistance coefficient changes linearly with regard to the vertical load regardless of the soil characteristics. Many published researchers consider the relationship of rolling resistance versus load as linear [Gheshlaghi et al., 2020] while Michelin [2013] reported slight nonlinearity with an exponent of 0.85.

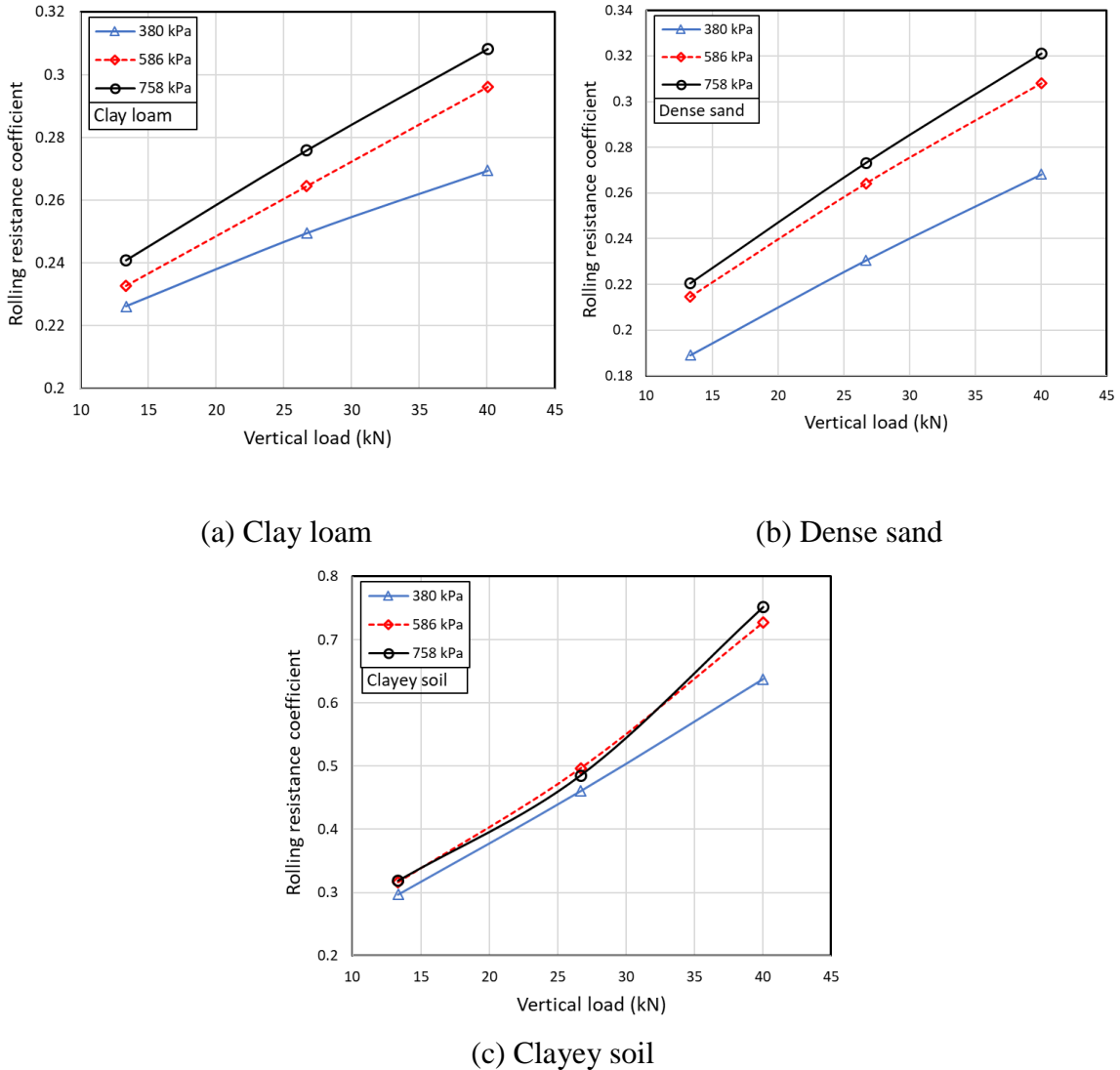


Figure 5.4. Influence of vertical load on rolling resistance coefficient of the tire rolling freely on different soils: (a) clay loam; (b) dense sand; and (c) clayey soil (forward speed = 10km/h)

5.3.2 Effect of inflation pressure

The sinkage of the wheel and thus the RRC is also strongly affected by the inflation pressure. The results in Fig. 5.4 suggest that the higher inflation pressure yields relatively higher RRC, while the effect of pressure on RRC is highly nonlinear. Furthermore, the application of a driving torque may also contribute to greater shearing of the soil and thereby higher external rolling resistance. Figure 5.5 shows the effect of inflation pressure on the RRC of the driven leading axle tire over the clay loam soil. The results are presented

for the constant forward speed of 10 km/h and three different magnitudes of driving torque (0, 2 and 4 kNm), where the 0 kNm torque represents the free-rolling tire. The results show that the RRC of the driven tire increases as the inflation pressure increases, as it was observed for the free rolling tire (Figure 5.4). The reason is that the rolling resistance of the tire in soft soils is the longitudinal force opposing tire motion due to soil deformation. As the tire inflation pressure rises until a maximum value, the soil sinkage rises, resulting in a rise in rolling resistance force. The most basic assumption for predicting the rolling resistance trend is that the wheel was analogous to a plate that was continually driven into the soil to a depth equal to the depth of the rut caused by the wheel. Bekker [1969] proposed equation 2.21 for the pressure beneath a plate of length l and width b driven into the terrain. Since the pressure is an exponential function of sinkage, the internal pressure of the tire is expected to show a nonlinear effect on the rolling resistance (Figure 5.5).

Nguyen et al. (2008) also reported trends similar to those seen in Figure 5.5. The study reported that the internal rolling resistance of the tire decreases with an increase in inflation pressure, while the external rolling resistance increases.

The results in Figure 5.5 clearly show the important effect of driving torque on the RRC. Unlike the free rolling tire, application of a driving torque yields a more nonlinear increase in RRC with increasing inflation pressure, while a higher drive torque leads to higher RRC. The reason is that at high torques, which generate a longitudinal force to the terrain of about half the applied vertical load, the rolling resistance increases significantly which is due to increasing longitudinal slip. The soil sinkage also increases with increasing the drive torque that producing a more nonlinear increase in RRC.

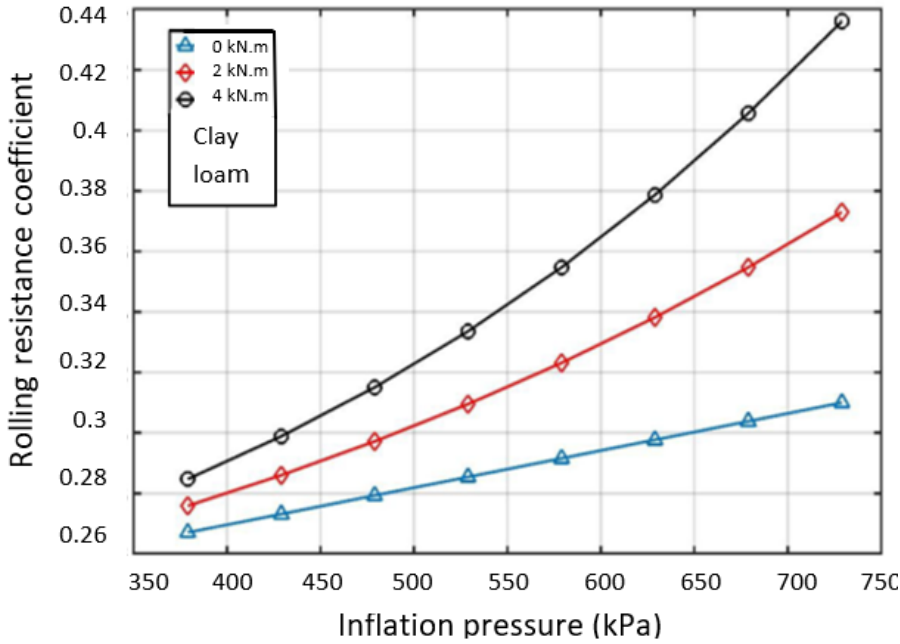


Figure 5.5. Effect of inflation pressure on rolling resistance coefficient of a driven tire subject to different drive torques over the clay loam soil (Forward speed: 10 km/h; Wheel load: 40 kN).

Figures 5.6(a), 5.6(b), and 5.6(c) further show the effects of variations in inflation pressure on the rolling resistance coefficient of the free rolling tire model coupled with the models of clay loam, dense sand, and clayey soil, respectively. The results are presented for a constant forward speed of 10 km/h and three different vertical loads (13 kN, 27 kN and 40 kN). The most significant effect of inflation pressure on the rolling resistance coefficient is observed for the clayey soil, especially under the 40 kN vertical load. The results suggest coupled effects of vertical load and inflation pressure on the RRC. For example, increasing the pressure from 370 kPa (54 psi) to 770 kPa (112 psi) yields an increase in RRC of about 0.02 under the vertical load of 13 kN or 27 kN. This is evident for all the three soils considered in the study. In general, the effect of inflation pressure on the RRC is relatively small when the vertical tire load is small. The rate of change of RRC with the inflation pressure is nearly negligible under light loads. The effect of inflation pressure on the RRC, however, becomes more pronounced with increase in the vertical load, particularly in case of the clayey soil.

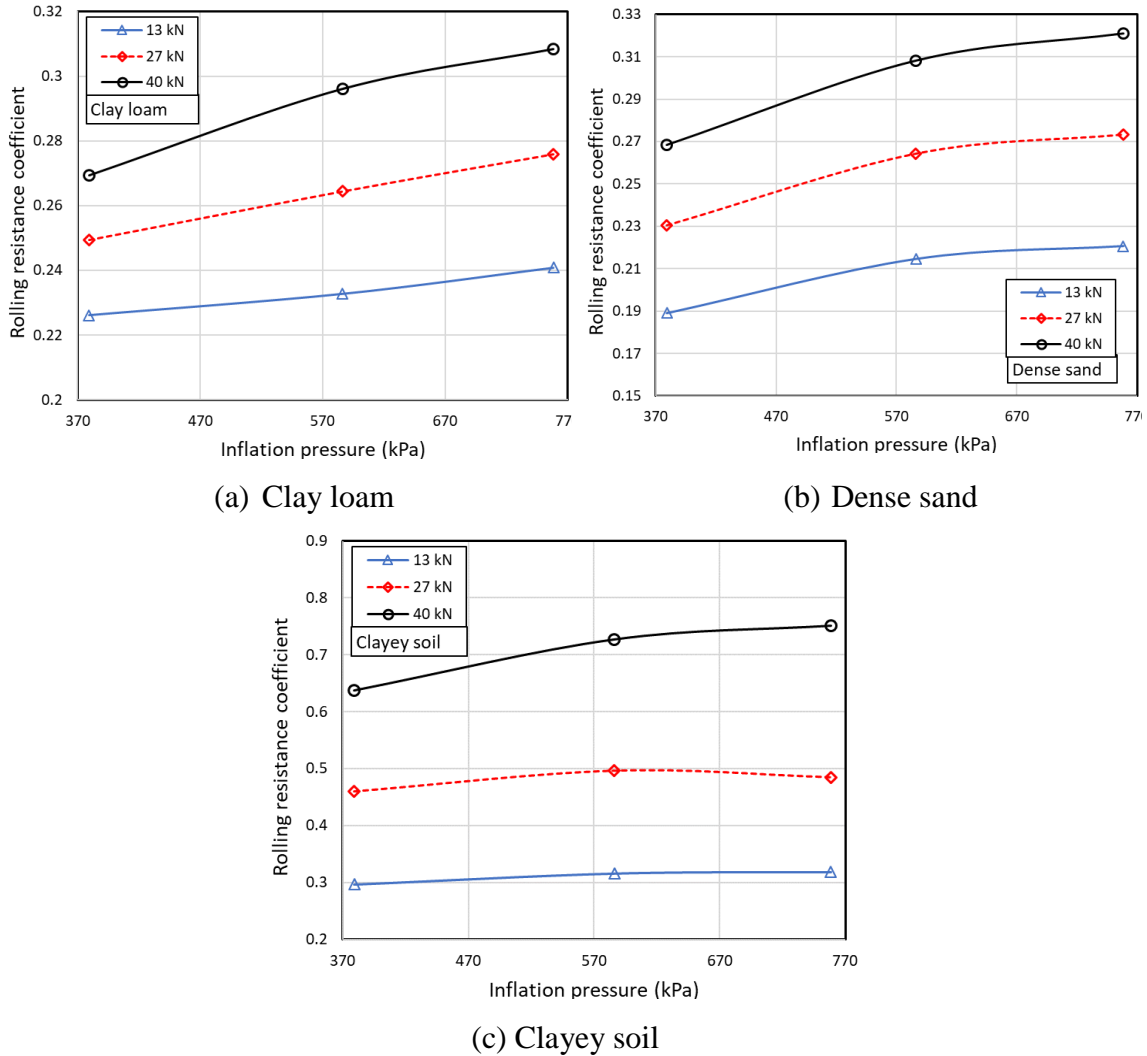


Figure 5.6. Influence of inflation pressure on rolling resistance coefficient of the tire rolling freely on different soils: (a) clay loam; (b) dense sand; and (c) clayey soil (forward speed = 10km/h)

Tire operation on clayey soil yields substantially higher RRC compared to those observed for the clay loam and dense sand, as seen in Figure 5.6(c). Under the 40 kN vertical load, the RRC of tire operating on the clayey soil increases from 0.63 to 0.75, when the inflation pressure is increased from 370 kPa (54 psi) to 770 kPa (112 psi). The results show that the external resistance of the tire is far more sensitive to both inflation pressure and load when compared to clay loam and dense sand soils. This is due to the softness of the soil, which causes the soil to deform more under pressure and vertical load and causes more rolling resistance.

5.3.3 Effect of soil compaction

The tire's interactions with a deformable terrain strongly depend on soil compaction, which tends to alter soil density and thereby sinkage or soil depth and the tire-soil contact footprint. Variations in soil compaction, observed especially during the passage of multiple wheels, may thus exhibit notable effects on RRC. The multi-pass model, described in Figure 5.3, is used to simulate the multi-pass effect of rolling tires on deformable soils. The simulations are performed for sandy soils with different moisture contents of 0%, 10% and 25%. The lead axle (axle 1), drive axles (axles 2 and 3) and the trailing axle (axle 4) are all subjected to vertical loads of 40 kN, 758 kPa (110 psi) inflation pressure and 10 km/h speed. These tests were performed on sandy soils with different moisture contents because they are a better representative of changes in rolling resistance to sinkage as they offer a wider range of internal soil friction. Data collection for these soils along with optimizing the time of all tests was another reason. It is noted that scattered tests for the multi-axle model with different pressures, loads and speeds in clay, clay loam and dense sand soils were also performed.

The passage of wheels on the soils causes soil compaction and thereby reductions in soil depth. The RRC is computed for the tire on each axle, which revealed notable effects of soil depth. Figure 5.7 shows the variations in RRC of different axle tire as a function of the corresponding soil depth. The soil depth after passing the first axle is 0.585 m, after passing the second axle is 0.575 m, after passing the third and fourth axles is 0.565 m. The same depth of the third and the fourth axle is due to the nature of the fourth tag axle. As shown in figure 5.7, the rolling resistance coefficient increases with the increase of soil depth. In another word, the highest rolling resistance force has been yielded at the highest soil depth after passing the first axle (0.585 m). It is due to the highest sinkage happening after passing the first axle on fresh soil. Since the second axle moves on compacted soil, it naturally sinks less in the soil and shows less rolling resistance than the first axle. This result is similar for the third and fourth axes. Furthermore, the rolling resistance coefficient decreases with increasing the soil moisture content which is due to an increase in the internal friction angle or in other words, increasing the ability of a unit of soil to withstand shear stress.

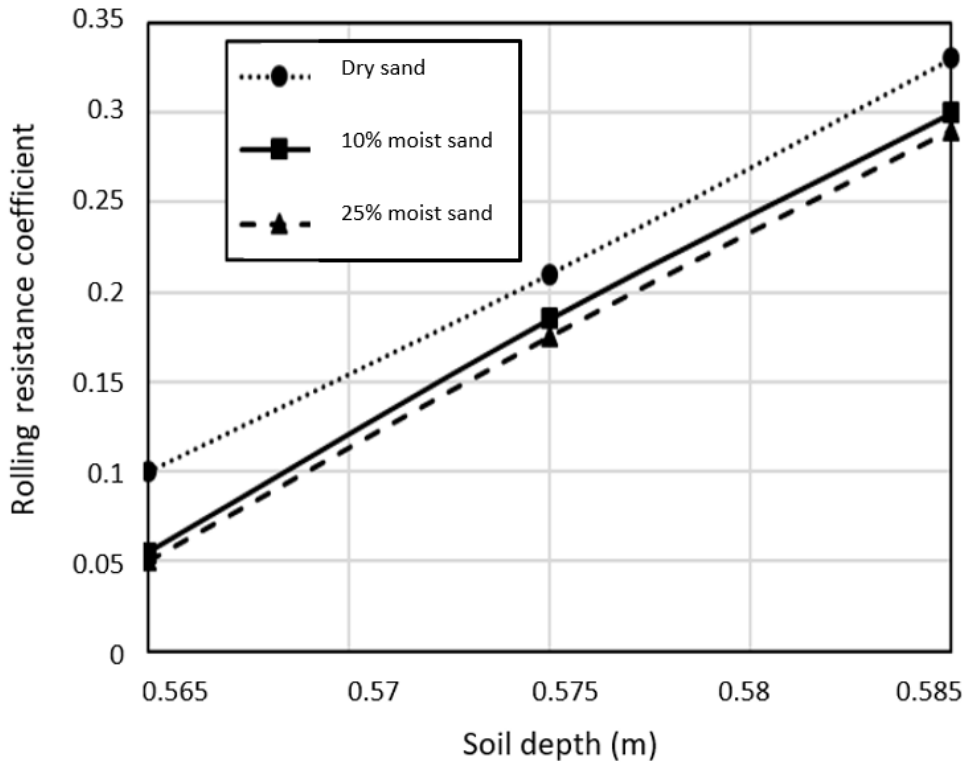


Figure 5.7. Rolling resistance coefficient as a function of soil depth at different soils

5.3.4 Effect of speed

The important effects of rolling speed of the tire on internal resistance of the tires operating on non-deformable terrains have been widely reported [Shakiba et al., 2016; Suyabodha et al., 2017]. Only limited knowledge, however, exists on the effect of rolling speed on the external resistance of the tires operating on deformable soils. In this study, the RRC of the tire operating on soft soils is investigated considering different speeds, ranging from 5 to 20 km/h. As an example, Figure 5.8 shows the variations in RRC of the tire rolling on the clay soil as a function of the longitudinal speed. The results were obtained considering 758 kPa (110 psi) inflation pressure and different vertical loads. The RRC increases considerably with the vertical load, as it was seen in Figure 5.4. The results, in general, show an increase in RRC with the forward speed. The rate of increase of RRC, however, depends on the vertical load. The RRC increases by approximately 25% when the speed is increased from 5 km/h to 20 km/h under the load of 13 kN. The corresponding increase in RRC is in the order of only 8% under the higher load of 40 kN. Similar tests were performed on clay loam soil at 758 kPa (110 psi) inflation pressure and different vertical loads. The

results showed that the RRC increases approximately 16% when the speed increases from 5 km/h to 20 km/h under 13 kN vertical load while the RRC increases approximately %11 when the speed increase by 15 km/h under 40 kN vertical load.

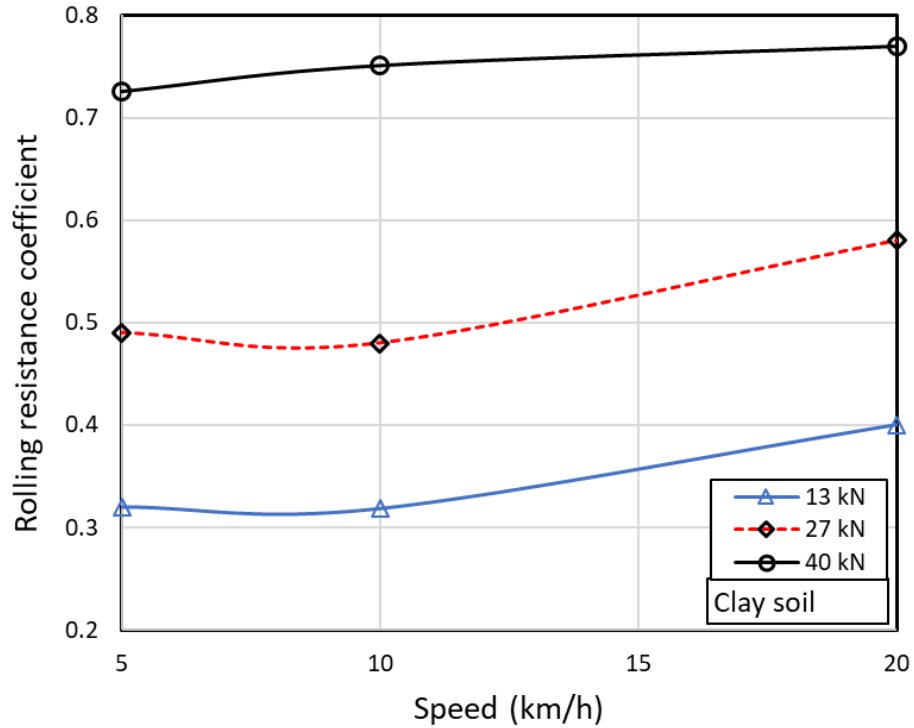


Figure 5.8. Effect of forward speed on the rolling resistance coefficient of the tire operating on the clay soil for different vertical loads (inflation pressure: 758kPa (110 psi))

5.4 The development of rolling resistance relationship using genetic algorithm

Owing to substantial computational demands of the FEA tire and SPH soil models, it is desirable to develop regression models for RRC considering a range of operating factors. This could facilitate computationally efficient analyses of vehicle and tire rolling resistance considering the multi-pass effects apart from the other operating factors. A relationship between RRC and the operating conditions could be obtained using the genetic algorithms, which are derived from evolution principles [Whitlwy, 1994]. The first application of GA was reported by J. Hollans [1992] to study the adaptive approach of ecosystems. A genetic algorithm is considered well suited for complex processes that rely on main operators such as mutation, selection, and crossover [Mitchell, 1996]. Abe [2004] used the GA to present

an optimum tire construction by considering many variables such as belt angle, belt topology, and belt materials. The optimized GA model was confirmed to enhance the cornering stiffness by more than 15% by comparing the control construction in an indoor drum test [Abe, 2004]. Taghavifar et al. [2015] developed a GA model to predict the power required for the driven tires of off-road vehicles. The data to generate the GA model were provided by a single-wheel tester in a soil bin facility under different vertical load, slip, and speed conditions. The model with a 0.022 mean square error showed a high-quality solution for predicting the power provided by the driven tire.

The genetic algorithm is the computational technique that can present the complex process of tire-soil interaction in the form of a mathematical relationship. Figure 5.9 shows the flowchart of the modeling technique used in this study to identify a GA mathematical relationship for RRC of the tire. It starts with an initial population considered as a random solution. Each population comprises a set of problem-solving candidates, called chromosomes. The chromosome evolution is based on the evaluation of fitness function through successive generations. The subsequent generation is made up of children in the current population. The algorithm creates parents by selecting a group of chromosomes that have the highest fitness in the current population. Three main operators (crossover, mutation, and selection) in the GA work together to guide the algorithm towards a successful solution. The user-defined crossover is used to generate a new offspring by combining the genetic information of two parents, while the mutation operator is activated to modify a chromosome for the next generation. The high-quality solutions are subjected to preferred weightings by choosing individual genomes for the subsequent breeding using the selection operator. Finally, after producing a successive population, the algorithm converges to the best chromosomes, which provide the optimal solution to the problem [Abe, 2004].

The Eureqa modeling engine is utilized in this study to develop a relationship between RRC and the essential operating conditions considering different soil environments. Eureqa software employs evolutionary search to anticipate a mathematical relationship between the input and output data points. The chromosome evolution is based on the evaluation of fitness function. The Eureqa training is internal and it produces different equations with

different accuracy. The operating conditions such as vertical load, speed, tire inflation pressure, soil depth, soil internal friction angle, and soil cohesion were considered as the inputs. While the rolling resistance was incorporated in the output. In order to study the multi-pass effect, which involved stacking of four FEA tire models to examine variations in rolling resistance with varying levels of soil compaction, the soil sinkage induced by each axle was regarded as the input reflecting the soil axle location.

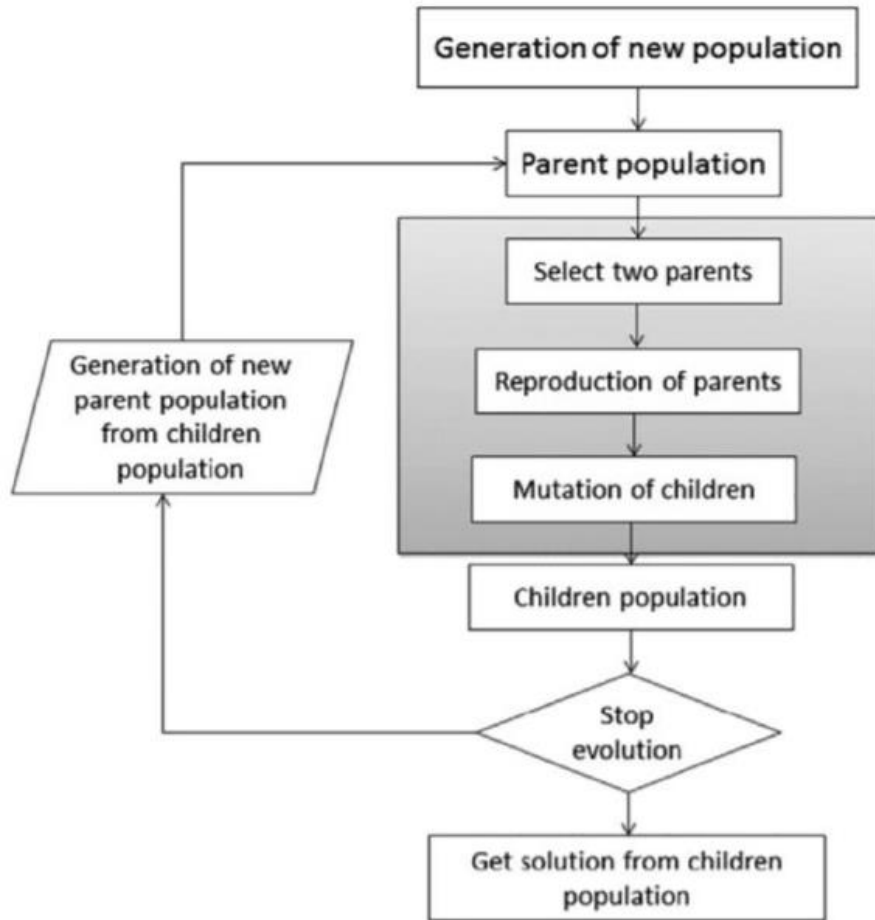


Figure 5.9. The flowchart of the proposed genetic algorithm [Abe, 2004]

The rolling resistance data collected from the FEA_SPH tire-soil simulation models were utilized to develop the relationships for the rolling resistance as a function of various operating conditions. The resulting GA rolling resistance relationship is subsequently implemented into the full vehicle model, denoted as the Volvo Transportation Model (VTM). The VTM is a MATLAB/Simulink code that predicts the full vehicle motions and responses during different maneuvers. The VTM model originally included the PAC2002

tire model which was replaced during previous work with a rigid ring tire model. The rigid ring tire model, however, does not consider the multi-pass effect. Moreover, it is not applicable for moist soils [El-Sayegh, 2020; Brantin, 2016]. In the study, a refined VTM model is formulated by replacing the longitudinal force of the rigid ring tire model with the developed GA relationship.

$$RRC = 4.35vd + 3.068e^{-6}F_zp + 2.034e^{-12}F_zTp^3 + \frac{0.0042F_z - 0.0239}{\phi - 12.14} - 6.856 - 0.0015c \quad (5.1)$$

$$F_x = \frac{T}{R} - RRC \times F_z \quad (5.2)$$

Where F_x and F_z are the average steady state forces in the longitudinal and vertical directions in kN, respectively, p is the inflation pressure in kPa, V is the forward velocity in m/s, C is the soil cohesion in kPa, ϕ is soil shear resistance in deg, d is soil depth in m, T is applied torque in kNm.

The GA algorithm comprised 312 outputs in its population and eight inputs for each output. These included inflation pressure, vertical load, speed, torque, soil cohesion, soil depth, and internal friction angle of the soil. The goodness of fit of the rolling resistance relationship, r^2 , was obtained as 0.91, while the mean square error was obtained as 0.0015.

The GA relationship, presented in Equation (5.1) suggests that the RRC varies in proportion to the vertical load, as it was observed in Figure 5.4, although the effect is coupled with the inflation pressure and drive torque. The ratio of the probability of a particular result in one intervention group vs that of a comparison group means the relative impact. The relative impact of vertical load on the rolling resistance coefficient model is around 0.35. Moreover, the RRC relationship could also predict the nonlinear effect of vertical load for the clayey soil, as it was observed in Figure 5.4(c). In other words, the relationship between the rolling resistance coefficient and the vertical load in most of the tested soils is linear. The Size (complexity) and the Fit (accuracy) on the validation data characterize the ideal solution Eureqa created for the rolling resistance coefficient. Eureqa ranks responses by default based on a complexity-to-accuracy ratio; answers that are right but not extremely difficult appear first. Eureqa employs a subset of the input data called

the training set to discover solutions. The validation data is provided by a different subset that is entirely used to determine the formulations' accuracy. Table 5.2 shows the sensitivity of each parameter on the rolling resistance coefficient in the most optimal solution with the highest goodness of fit and the least mean error compared to other solutions.

Table 5.2. Sensitivity analysis of GA equation parameters on the rolling resistance coefficient

Variable	Relative impact on rolling resistance coefficient
F_z	0.35
P	0.2
ϕ	1.36
d	0.778
c	0.09
T	0.078
v	0.0751

The GA rolling resistance coefficient equation shows that the rolling resistance coefficient as a function of inflation pressure is not linear, and it appears in two terms. The relative impact within the model for the pressure is around 0.2. Furthermore, as the torque increases the effect of pressure on the rolling resistance coefficient becomes more nonlinear, this is visible in the term of equation 5-1.

It is noted that the relative impact of the soil compaction on the RRC equation is 0.778 while the internal friction angle has a relative impact on the equation of around 1.36.

To evaluate the developed GA rolling resistance coefficient equation on different terrains, rolling resistance tests were performed with the RHD tire in the mud. The simulations were carried out with the RHD tire in an SPH soil channel at 40 kN vertical load and 758 kPa (110 psi) inflation pressure at the first, second, third, and fourth axle with different speeds of 10 km/h, and 15 km/h. After extracting the simulation data of tire rolling resistance coefficient on the mud, these data were compared with the data obtained from the genetic rolling resistance coefficient equation. Thus, in the genetic equation of rolling resistance coefficient, the mud characteristics and the operating conditions similar to the simulations

were used. Figure 5.10 shows the simulated and GA rolling resistance coefficient with R2 goodness of 0.907 which shows the capability of the GA RRC model to predict the rolling resistance coefficient of the tire on the mud.

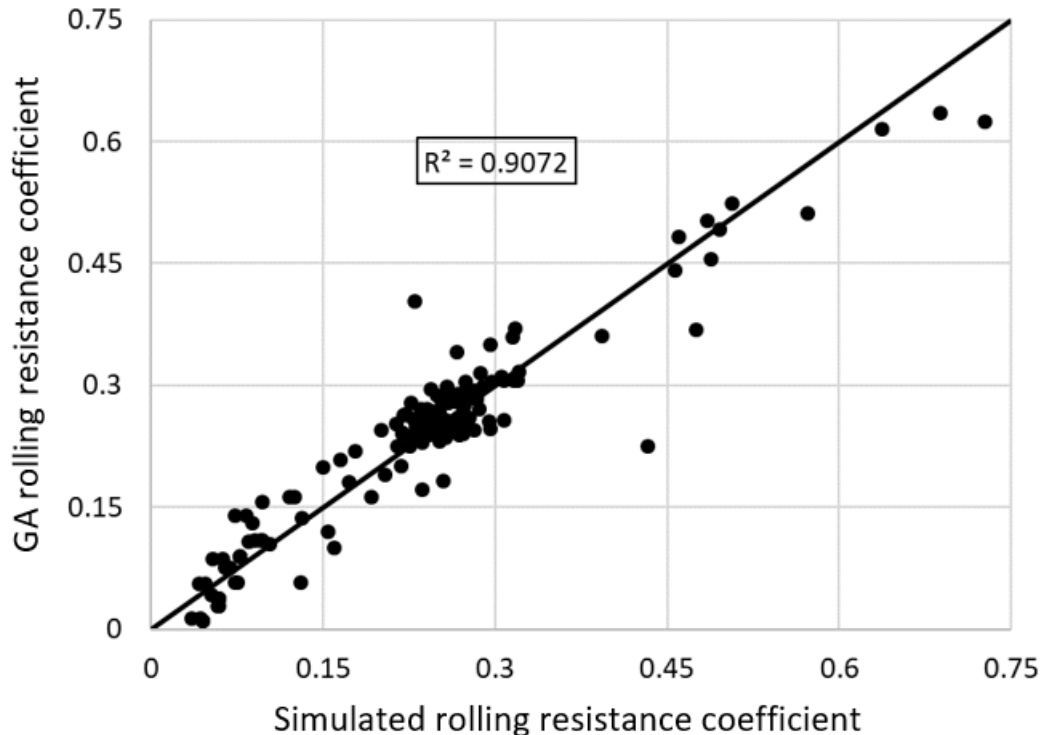


Figure 5.10. Predicted versus simulated rolling resistance coefficient

5.5 Summary

The rolling resistance for the RHD truck tire size 315/ 80R22.5 was analyzed under various terrains. The SPH approach was used to model and calibrate the soils, and the findings were given in Chapter 4. This chapter focuses on estimating, analyzing and validating the rolling resistance coefficient equation for a truck tire running over various soils under various operating conditions, such as tire inflation pressure, vertical load, and speed.

The rolling resistance coefficient was found to be highly dependent on the applied vertical load. The tire inflation pressure, on the other hand, has less impact on the rolling resistance coefficient at low vertical loads and a larger impact at high vertical loads. Concerning a truck tire traversing various terrains, the truck tire was found to have the greatest rolling

resistance coefficient at a lower internal friction angle. As a result, if a truck is driving through clayey terrain, it will use more gasoline than if it is driving on clay loam.

The RRC data from this chapter was then utilized to establish an equation between the RRC and the operating conditions. Cohesion, internal friction angle, and soil sinkage were used to create the operating conditions in addition to tire operating conditions such as inflation pressure, vertical load, and speed. An equation that relates the rolling resistance coefficient with several operating conditions was developed using advanced algorithm techniques through training and testing using Pam-Crash simulation results. It was concluded that the equation can predict the rolling resistance coefficient at different operating and soil conditions. The developed equation has an R-square fitness of 0.91 (91.1%), the mean square error is 0.0015 and the mean average error is 0.022.

CHAPTER 6

TIRE-TERRAIN INTERACTIONS ANALYSIS:

CORNERING CHARACTERISTICS

6.1 Introduction

The cornering property of a tire is most critical for adequate vehicle handling and directional stability. The cornering characteristics of tires are strongly affected by many designs and operating factors such as tire construction and material properties, tire load, inflation pressure and rolling speed [El-Razaz et al., 1988; Bolarinwa et al., 2004]. In an off-road environment, the properties of the soil further affect the cornering properties in a highly complex manner. In this chapter, the tire-terrain interaction models, integrating the FEA tire model and the SPH soil models, are used to derive the cornering properties of the tire under different operating conditions including different soils. Owing to the excessive computational demands of the tire-terrain interaction models, the simulation results attained for selected operating conditions are used to develop a mathematical relationship between the cornering property and the operating factors.

The first part of the chapter presents a tire-terrain interaction model setup using a combination of FEA and SPH techniques for calculating tire cornering characteristics for different operating conditions. The operating conditions include the longitudinal speed, applied torque, inflation pressure, vertical load, and slip angle. The soil characteristics such as cohesion, angle of internal friction and sinkage are considered in the setup. The second part of the chapter includes the analysis of cornering characteristics under different operating and soil factors. In the final section, the simulation results are used to develop regression relationships for the cornering force, self-aligning moment, and overturning moment as functions of the operating factors. The relationships are developed using advanced algorithm techniques through testing, training and validations while taking into consideration the multi-pass effect, soil compaction, and the free-rolling and the driven tire. The validity of the proposed mathematical relations is demonstrated in the final section considering different operating conditions. For this purpose, the cornering tests of the RHD tires were performed while operating over the mud soil.

6.2 Simulation model setup

Two different model simulation schemes were designed to determine the tire cornering characteristics. In the first scheme, a single tire-terrain interaction model is used to evaluate tire's cornering characteristics on different soils to reduce the simulation time. The second scheme employs a 4 tires multi-pass interaction model to study the multi-pass and soil compaction effects. The model, shown in Figure 6.1, represents a four-axle Volvo truck. The numerical tests are carried out for both driven and free-rolling tires.

After inflating each tire to the desired inflation pressure, the selected vertical load is applied to the center of the rim. The tire is subsequently pre-steered to various slip angles, ranging from 0° to 12° , to investigate the cornering force and aligning moment as a function of the side-slip angle. In the case of the free-rolling tires, each tire is permitted to roll so as to achieve a desired forward speed. The simulations are performed for three different forward speeds (5 km/h, 10 km/h and 15 km/h). In the case of driven tires, an angular velocity is applied to the center of each driven tire. The force responses within the contact area between the tires and the soil are extracted to obtain the cornering force and aligning moment for each given side-slip angle. Apart from the aligning moment (M_z) about the vertical axis of the tire, the shift in the vertical force center is considered to derive the overturning moment (M_x) of the tire, as shown in Figure 6.2. The overturning moment is predominantly caused by two factors. These include the horizontal deformations of the tire carcass induced by the lateral force, and the effective carcass camber caused by the tire camber and the lateral force.

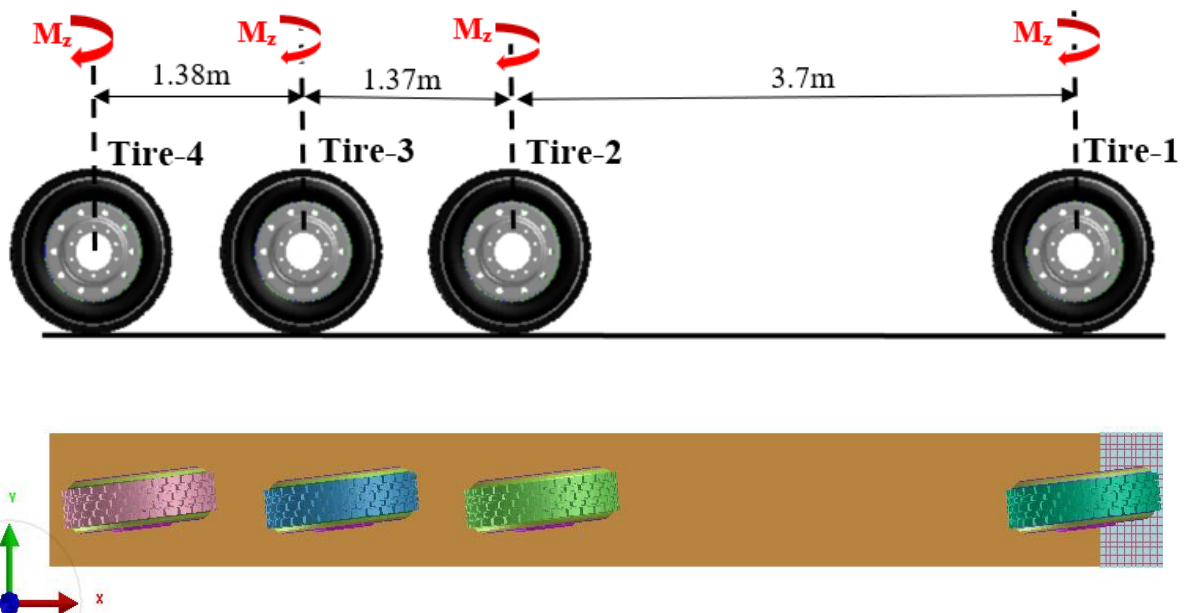


Figure 6.1. Tire-terrain interaction model considering side-slip of tires of a four-axle truck

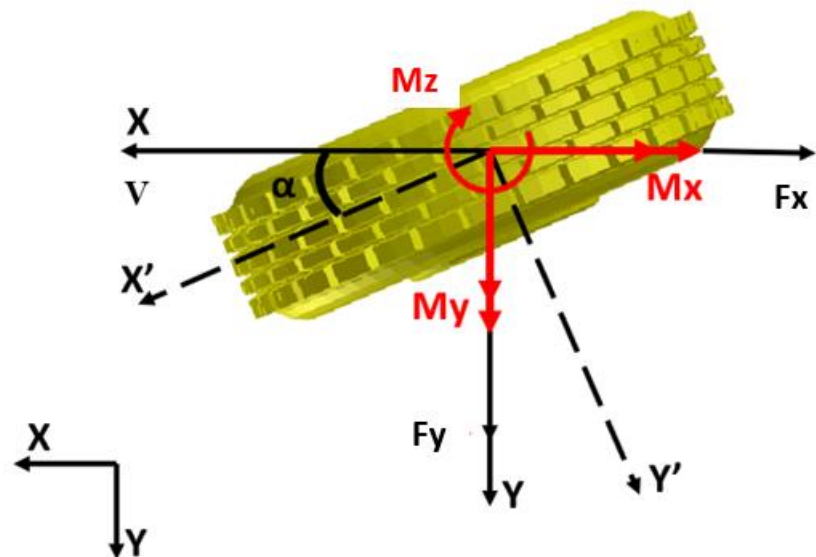


Figure 6.2. Forces and moments acting on a steered tire

6.3 Cornering characteristics analyses

The tire-soil interaction model simulations were performed considering different operating conditions and soils. The operating factors included four levels of forward speed (5, 10, 15, and 20 km/h), three levels of inflation pressure (379.21(55 psi), 586.05 (110 psi) and 758.42 kPa (130 psi)), three levels of vertical load (13, 27, and 40 kN) and four different side-slip angles (0, 2, 4, 6, and 12 degrees). The soil models included those of clay, sandy loam, clay loam, 10% moist sand, 25% moist sand and 50% moist sand. The simulation results obtained for both the schemes are discussed in the following sub-sections.

6.3.1 Effect of side-slip angle

Figures 6.3 and 6.4 illustrate the variations in the self-aligning moment and cornering force developed by each free-rolling tire as a function of the slip angle, respectively. The simulation setup, in this case, includes the four wheels model to investigate the multi-pass effect on the cornering characteristics. The simulation results are presented for the sandy loam soil (cohesion 9.8 kPa and internal friction angle 29.4 degrees), as an example, considering the constant forward speed of 15 km/h speed, 758 kPa (110 psi) inflation pressure, and 40 kN vertical load. The results show that the self-aligning moment increases with an increase in the slip angle and it is more significant under a higher level of soil compaction. In other words, the self-aligning moment increases as the soil undergoes compaction. It is noted that the cornering force and self-aligning moment reach saturation on the hard surface only at a larger slip angle, but on soft soil, they don't [El-Razaz, 1988; Schwanghart, 1981]. It is because the lateral force generated by an off-road tire is a function of the tire's lateral deformation and the soil shear-induced lateral deformation. The lateral deformation of a tire refers to a force at the soil-tire contact caused by a displacement of the tire tread or carcass, and it is the most important characteristic for determining the lateral force of tires on hard surfaces. The lateral displacement of soil due to soil shearing which is characterized by Equation 2.20 is the more important parameter on the lateral force of tires on deformable terrains. Since the soil shearing behavior shows a linear relationship based on Equation 2.20, a linear trend is also expected for the cornering force and self-aligning moment versus slip angle on deformable terrain.

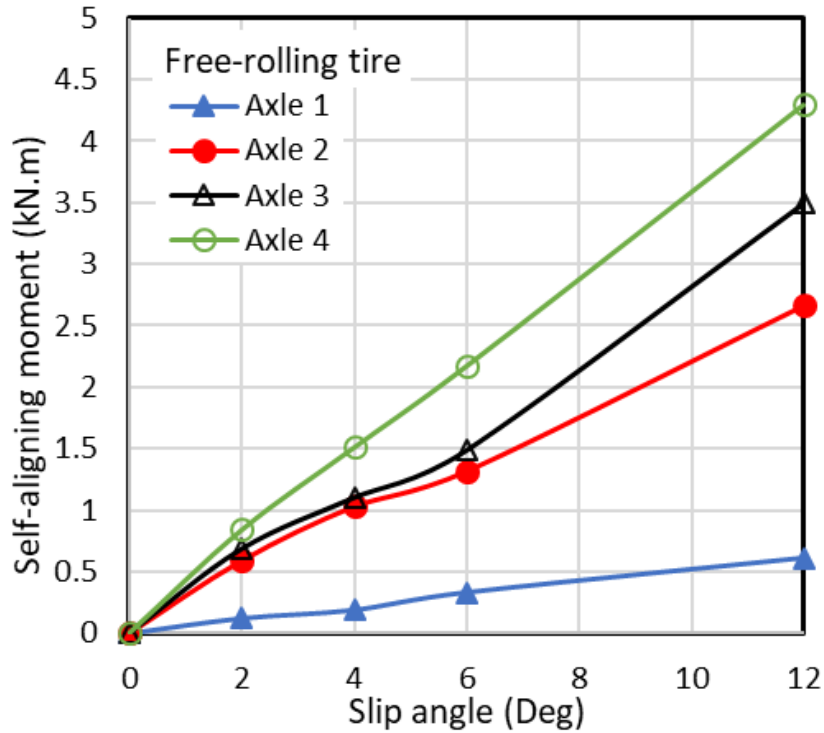


Figure 6.3. Self-aligning moment as a function of side-slip angle for the free-rolling tires over the sandy loam at different axles (speed:15 km/h; inflation pressure: 758 kPa (110 psi) ; vertical load: 40 kN)

Figure 6.4 shows the variations in the cornering forces developed by the free-rolling tires of different axles as a function of the slip angle while running over the sandy loam at a speed of 15 km/h speed. The cornering force of radial-ply truck tires increases with an increase in the slip angle. The results suggest the minimal effect of soil compaction on the cornering stiffness of tires, defined as the cornering force gradient in the vicinity of zero side-slip. The cornering stiffness seems to be similar for all wheels, irrespective of compaction. It is because the cornering stiffness is the tire's ability to resist deformation while cornering and this ability depends on tire characteristics which are the same in all axles. The effect of soil compaction on the cornering force is evident under higher slip angles. In other words, the cornering force shows the highest value at the highest slip angle (12 degrees) and highest compaction level (Axe 4). For example, the tire at 12 degrees side-slip angle shows a cornering force of 22 kN at the first pass while this value for the fourth pass is 35 kN. It is due to the tire's lateral deformation effect which is evident on compacted soils [El-Razaz, 1988].

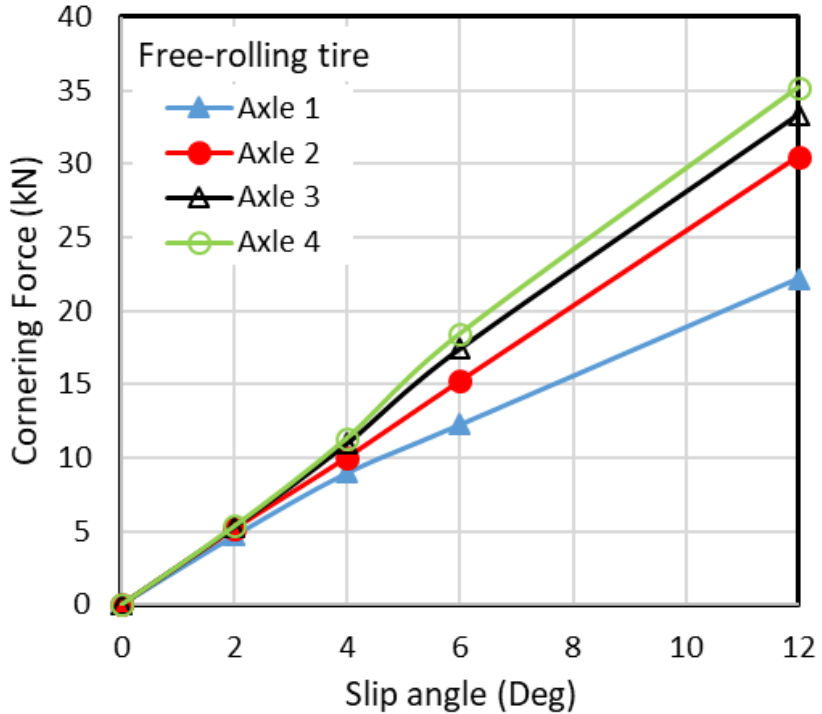


Figure 6.4. Cornering force as a function of side-slip angle for the free-rolling tires over the sandy loam at different axles (speed: 15 km/h; inflation pressure: 758 kPa (110 psi); vertical load: 40 kN)

The cornering properties of the tires are further investigated in the presence of drive torque. Figures 6.5 and 6.6 show the self-aligning moment and cornering force characteristics, respectively, of the driven tires as a function of slip angle. The results are obtained considering the angular velocity of 8.25 rad/s (equal to 15 km/h forward speed) applied to all axle tires, while the cornering responses are obtained at the forward speed of 15 km/h, 758 kPa (110 psi) inflation pressure, and 40 kN vertical load. It is noted that the variation of the angular velocity at constant linear longitudinal velocity will result in longitudinal slip which indicates that the cornering force is calculated at a driven rolling tire. The self-aligning moment increases with side-slip angle and it becomes more significant with increasing level of soil compaction. The tires' multi-pass effect on the self-aligning moment is clearly evident in Figure 6.5. At a 6° side-slip angle, the self-aligning moment developed by the second axle tire is nearly twice that of the leading axle tire, which is attributable to soil compaction by the leading axle tire. Tires of the subsequent axles' tires, however, exhibit a relatively smaller increase in the aligning moment, suggesting the

reduction in soil compaction. The effect of soil compaction on the cornering force, however, is very small, especially at low slip angles. The effect of soil compaction becomes more pronounced under higher side-slip angles, as seen in Figure 6.6. Comparisons of cornering properties of driven tires with those of the free-rolling tires (Figures 6.3 and 6.4) show both the cornering force and self-aligning moment are substantially small for the driven tire compared to the free-rolling specially on compacted soil. Is it because of traction force and friction split happening in driven tires. The traction allows the tire to accelerate in a controlled manner and yields small cornering force and self-aligning moment.

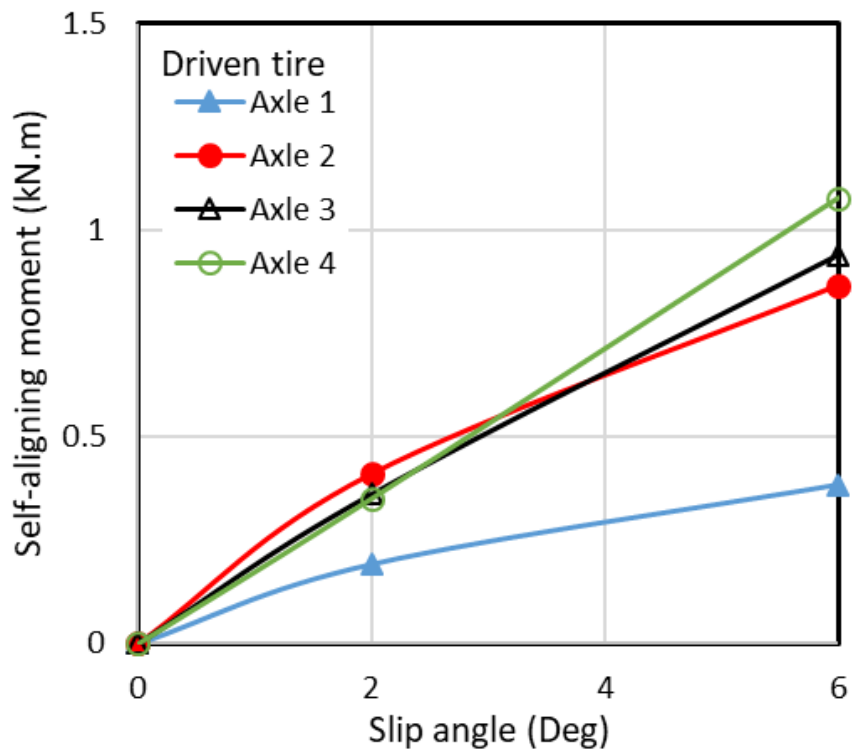


Figure 6.5. Self-aligning moment as a function of side-slip angle for the driven tires over the sandy loam at different axles (speed: 15 km/h; inflation pressure: 758 kPa (110 psi); vertical load: 40 kN)

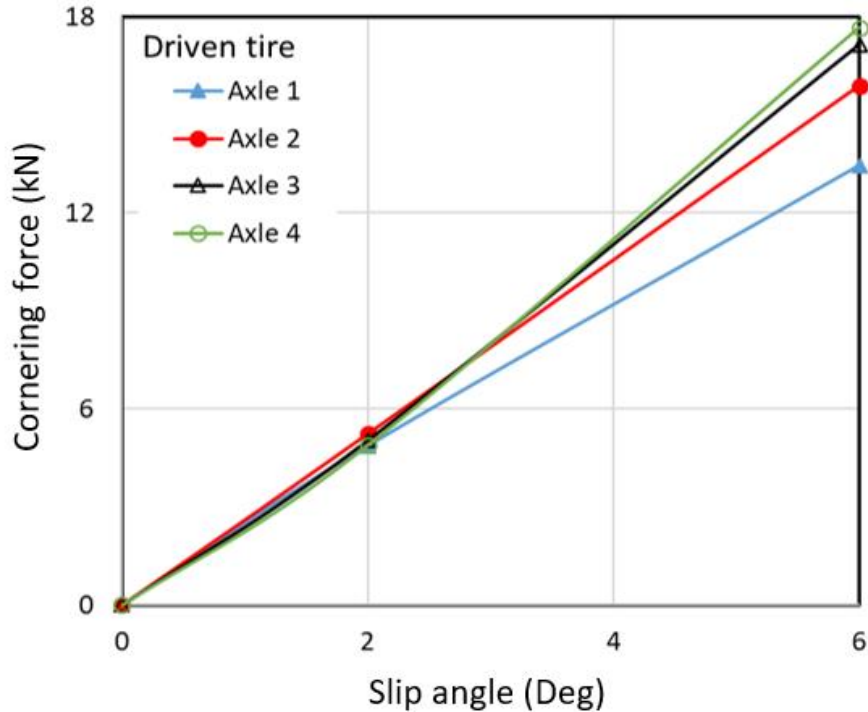


Figure 6.6. Cornering force as a function of side-slip angle for the driven tires over the sandy loam at different axles (speed: 15 km/h; inflation pressure: 758 kPa (110 psi); vertical load: 40 kN)

The overturning moments developed by the rolling tires are further evaluated under various side-slip conditions. As an example, Figure 6.7 illustrates the variations in overturning moments of different axles' tires as a function of tire slip angle considering free-rolling over the sandy loam soil. The results are obtained for the constant forward speed of 15 km/h, 758 kPa (110 psi) inflation pressure, and 40 kN vertical load. The results show trends similar to those observed for the cornering forces, shown in Figure 6.4. The simulations were also performed to evaluate cornering force, aligning moment and overturning moment characteristics of the free-rolling and driven tires operating on different soils. The results obtained from all the soils considered showed similar trends. Considering identical loads and operating speed, the overturning moments developed on the clay loam soil were higher than those observed for the clay soil, which is attributable to the mechanical properties of the soils, especially the greater compliance of clay loam soil.

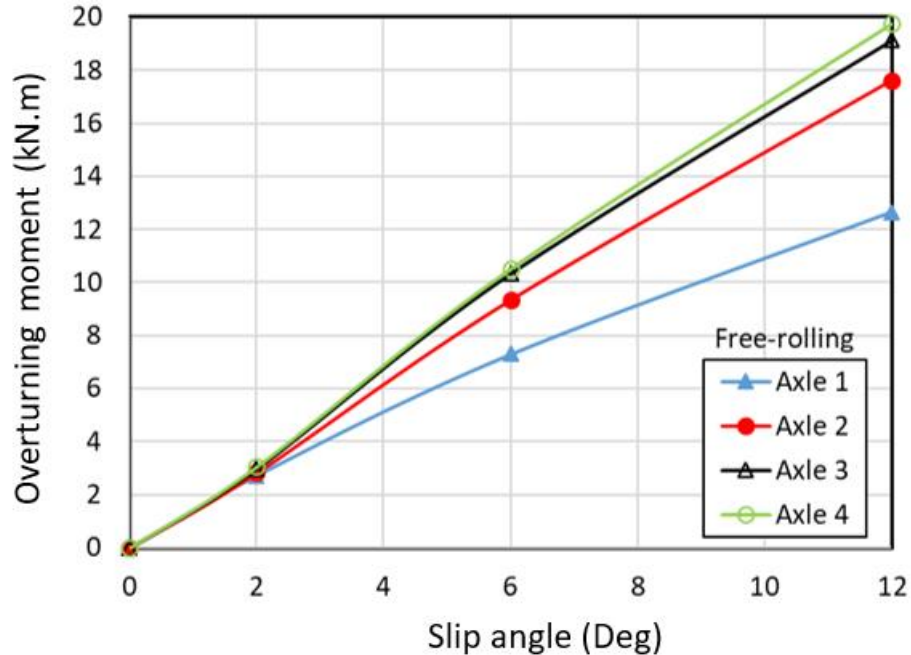


Figure 6.7. Overturning moment as a function of side-slip angle for the free-rolling tires over the sandy loam at different axles (speed: 15 km/h; inflation pressure: 758 kPa (110 psi); vertical load: 40 kN)

6.3.2 Effect of vertical load

Variations in vertical load applied to the wheel are known to significantly alter the cornering properties of tires operating on non-deformable terrains [Jiang et al., 2014; Vorotovic et al., 2013]. The increase in wheel sinkage and soil compaction under a higher vertical load further affect the cornering properties of the tires operating on deformable soils. As an example, Figures 6.8 and 6.9 show variations in the self-aligning moment and cornering force, respectively, developed by a free-rolling tire corresponding to 6° side-slip angle as a function of the vertical wheel load, while operating on the 25% moist sandy soil (cohesion: 4 kPa; internal friction angle: 21.36 degree). The simulation results are obtained for the lead axle tire operating at a constant forward speed of 15 km/h speed with three different inflation pressures (379, 586 and 758 kPa (55, 85 and 110 psi)). For a given inflation pressure, both the self-aligning moment and cornering force increase nearly linearly with the vertical load. It is due to the increase in soil sinkage and shear zone with the increase in the vertical load that increase the cornering force. The pneumatic trail is also extended accordingly to enlarge the contact area in higher tire loads. Correspondingly

the increased cornering force and pneumatic trail cause a rise in the self-aligning moment. On the other hand, the cornering force and aligning moment of the tire increase with the decrease in inflation pressure, although the effect of inflation pressure is not linear. It is due to the fact that tire deformation increases with the decrease in inflation pressure which causes higher cornering force. Decreasing the inflation pressure for a given vertical load also increases the pneumatic trail that causes a substantially higher self-aligning moment. Similar tendencies are also seen in other soils however the increase or decrease rate of cornering force and self-aligning moment is different due to the softness or hardness of the soil.

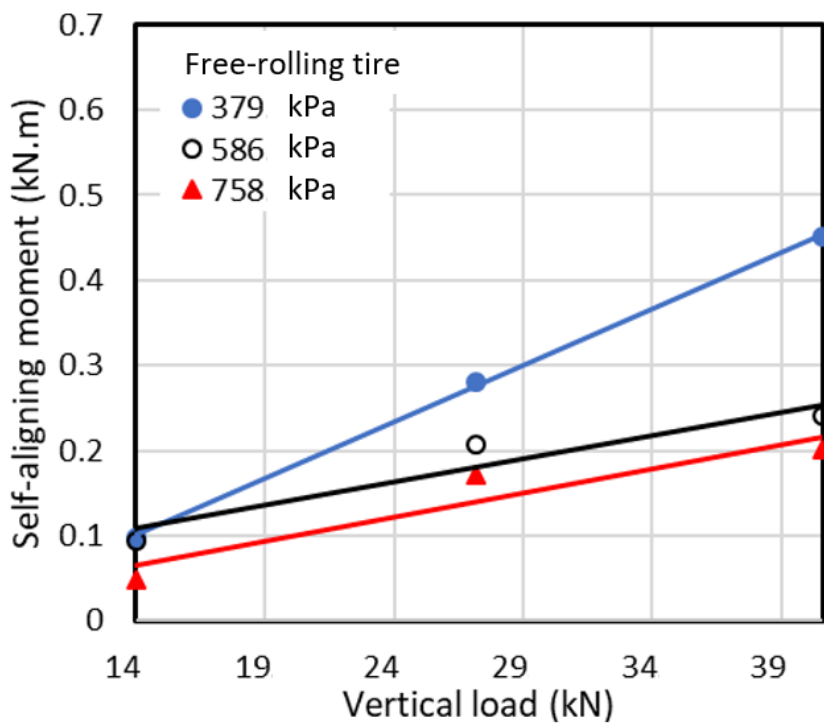


Figure 6.8. Influence of vertical wheel load on the self-aligning moment of the free-rolling tire operating on 25% moist sandy soil for different inflation pressures (slip angle: 6 deg; speed: 15 km/h)

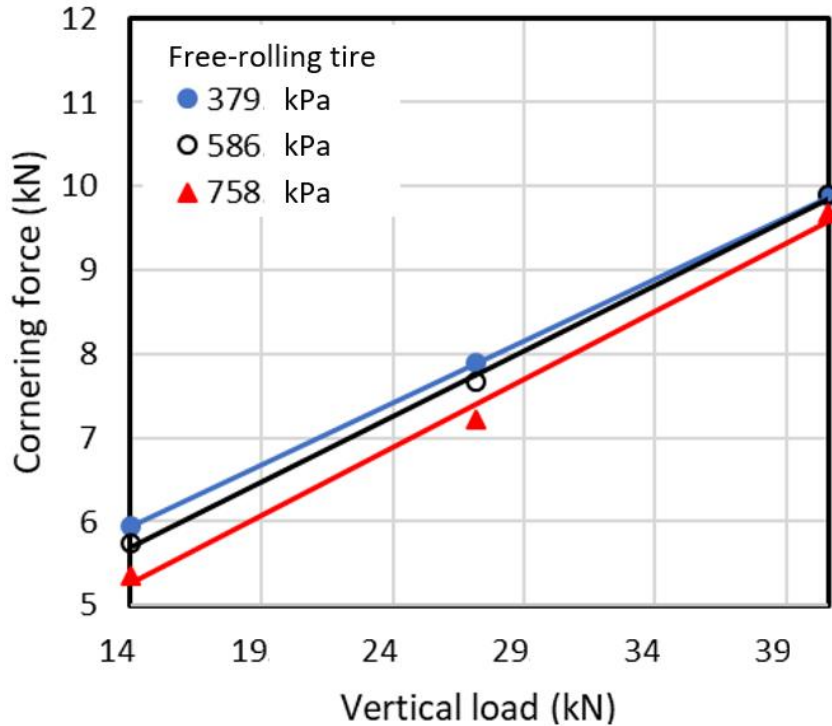


Figure 6.9. Influence of vertical wheel load on the cornering force of the free-rolling tire operating on 25% moist sandy soil for different inflation pressures (slip angle: 6 deg; speed: 15 km/h)

Figures 6.10 and 6.11 illustrate variations in the self-aligning moment and cornering force developed by the tire subject to 6° side slip, and an angular velocity of 8.25 rad/s (equal to 15 km/h forward speed) and different vertical loads. The simulation results are obtained for the leading axle tire considering a constant forward speed of 15 km/h speed, and different inflation pressures (379, 586 and 758 kPa (55, 85 and 110 psi)). The results show higher self-aligning moment and cornering force with the increasing vertical load. The results also show the nonlinear effect of inflation pressure on the cornering properties, which is due to the effects of tire pressure on wheel沉降 (sinkage), soil compaction, footprint area part from the out-of-plane stiffness of the tire. Increasing the inflation pressure yields a substantially lower self-aligning moment, while an opposite effect is observed on the cornering force. It is noted that the both cornering force and pneumatic trail affect the self-aligning moment. Increasing the inflation pressure causes an increase in the soil sinkage specially at high vertical loads while it causes a decrease in the pneumatic trail. Accordingly increasing and decreasing the soil sinkage and the pneumatic trail,

respectively cause an increase in the cornering force and a decrease in the self-aligning moment, respectively. The increase rate of cornering force is probably less than the decrease rate of pneumatic trail that yields a lower self-aligning moment. Like Figures 6.3-6.6, the driven tire of the first axle shows a higher self-aligning moment and cornering force than the free-rolling tire. It is due to the fact that the driven tire of the first axle on soft soil causes the highest soil sinkage that increases the cornering force and self-aligning moment accordingly. At the second, third and fourth axles of driven tires, the driven tire operates on compacted soil and causes lower cornering force and self-aligning moment than the free-rolling tire because of traction force and friction split happening in driven tires.

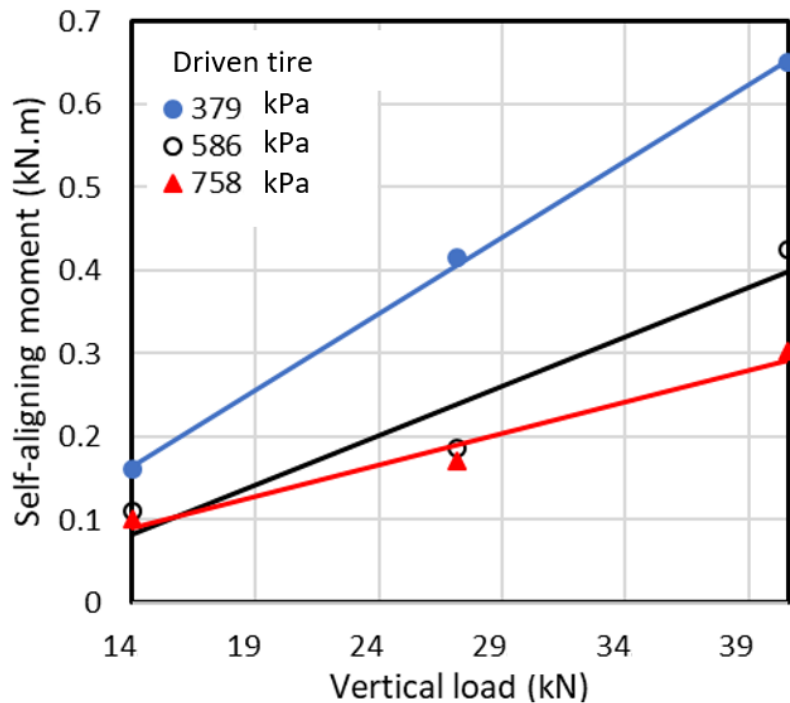


Figure 6.10. Influence of vertical wheel load on the self-aligning moment of the driven tire operating on 25% moist sandy soil for different inflation pressures (slip angle: 6 deg; speed: 15 km/h)

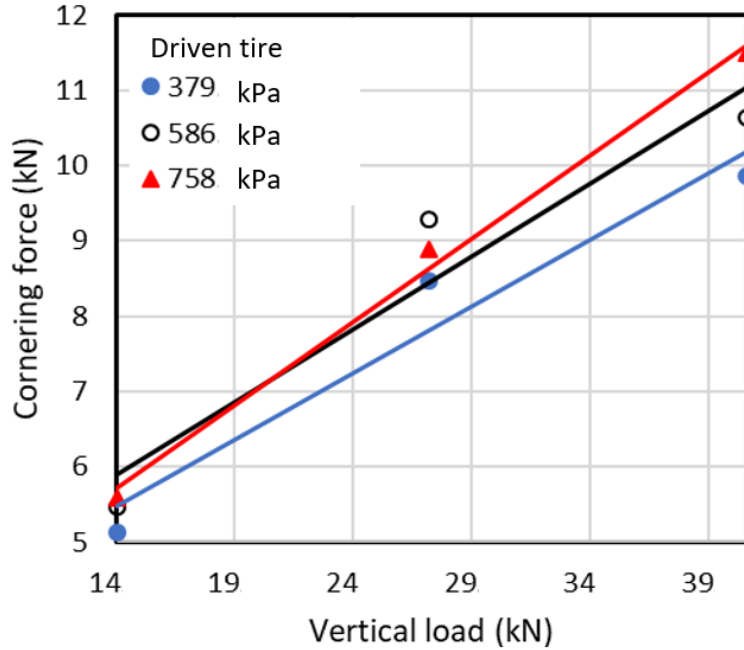


Figure 6.11. Influence of vertical wheel load on the cornering force of the driven tire operating on 25% moist sandy soil for different inflation pressures (slip angle: 6 deg; speed: 15 km/h)

Figure 6.12 further illustrates the effect of vertical load on the overturning moment developed by a free-rolling tire on the 25% moist sandy soil (cohesion: 4 kPa; internal friction angle: 21.36°). The results are presented for 12 deg slip angle, 10 km/h speed and different inflation pressures. For a given inflation pressure, the results show that the overturning moment increases nearly linearly with the vertical load, irrespective of the inflation pressure. In addition, at a given vertical load the overturning moment increases only minimally as the inflation pressure decreases. It is noted that for other soils at the given inflation pressure, the cornering force increases with an increase in the normal load in the entire range of side-slip angles. At higher side-slip angles the cornering force increases rapidly, which is attributed to greater adhesion of the contact patch with the soil.

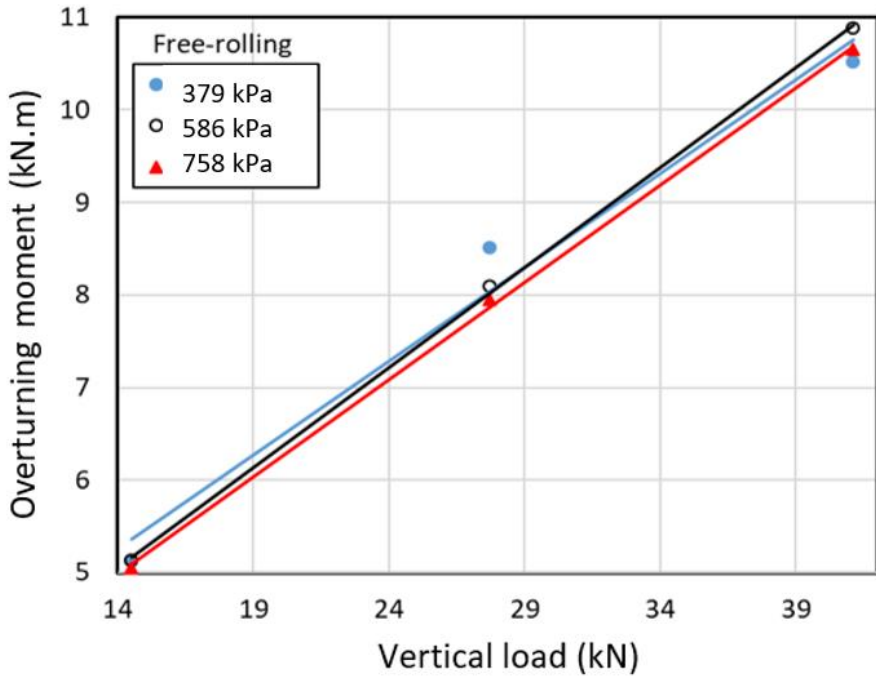


Figure 6.12. Influence of vertical wheel load on the overturning moment of the free-rolling tire operating on 25% moist sandy soil for different inflation pressures (slip angle:

6 deg; speed: 15 km/h)

6.3.3 Effect of inflation pressure

Figures 6.13 and 6.14 show the influence of tire inflation pressure on the self-aligning moment and cornering force, respectively, of the tire rolling freely over the 25% moist sand (cohesion: 4 kPa; internal friction angle: 21.36°). Simulation results are obtained considering 40 kN vertical load and 15 km/h forward speed. The results are also presented for two different side slip angles: 2° and 6° . As the inflation pressure increases, the self-aligning moment decreases and this decrement is more visible at 6° slip angle. Higher side slip angle means higher side velocity and therefore lateral shearing that makes a higher cornering force. The results suggest the effect of pressure on the aligning moment is nonlinearly coupled with the side-slip angle and thus the side velocity. The effect of pressure on the aligning moment is very small under lower side-slip angles, while it becomes more pronounced for higher slip angles. Increasing the inflation pressure causes a considerable reduction in the aligning moment under the higher side-slip of 6° , as seen in Fig. 6.13, which may be attributed to the lower pneumatic trail. The moment comes from

cornering force and shift in the center of force (trail effect). In this case, since the cornering force is almost constant, the change in the pneumatic trail is the predominant factor affecting the self-aligning moment variation. The effects of tire pressure variations on the cornering force, however, is considerably small, irrespective of the side-slip angle, as seen in Figure 6.14. Other studies reporting the effect of inflation pressure on cornering force developed by a tire operating on non-deformable as well as deformable surfaces have also reported similar trends [El-Razaz et al., 1988; Shokouhfar, 2017].

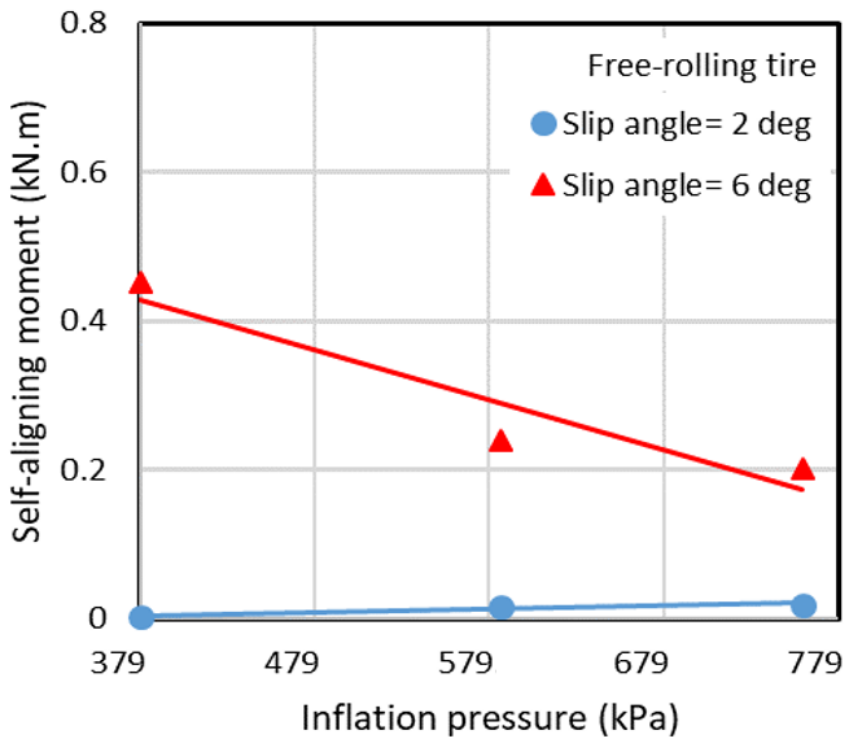


Figure 6.13. Influence of inflation pressure on self-aligning moment of the tire rolling freely on the 25% moist sandy soil for two different slip angles (vertical load: 40 kN; speed: 15 km/h)

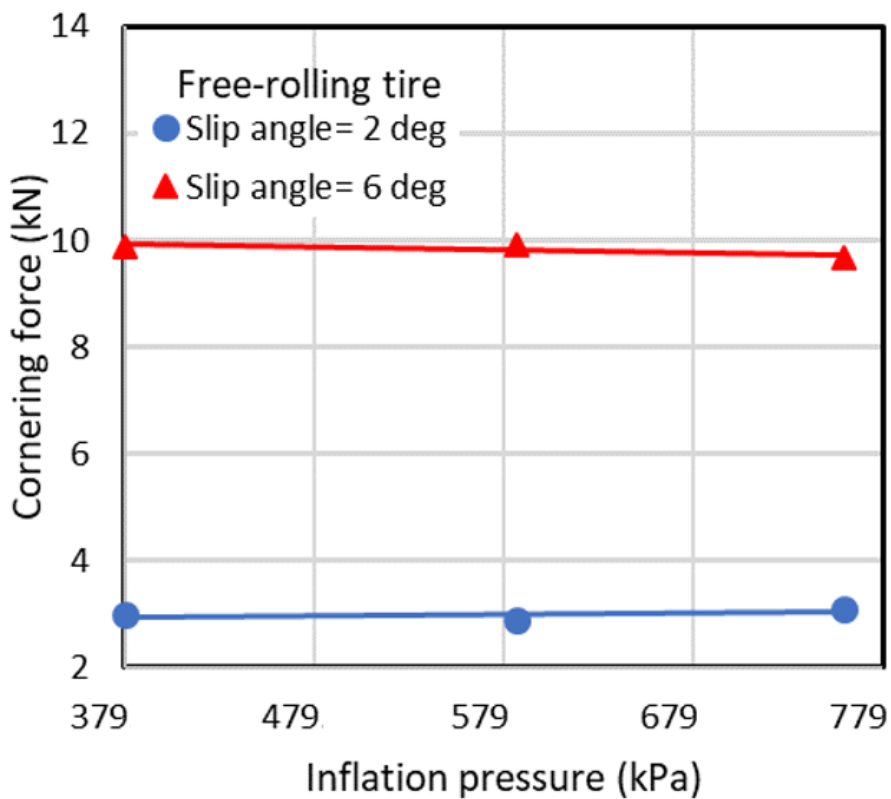


Figure 6.14. Influence of inflation pressure on cornering force of the tire rolling freely on the 25% moist sandy soil for two different slip angles (vertical load: 40 kN; speed: 15 km/h)

In a similar manner, Figures 6.15 and 6.16 show the effect of inflation pressure on characterizing characteristics of the driven tire operating on the same soil at a speed of 15km/h and 40 kN vertical load. The results suggest that an increase in inflation pressure yields notable reduction in the self-aligning moment for both the slip angles, as seen in Figure 6.15. Unlike the free-rolling tire, notable reduction is also evident for the lower side-slip angle of 2° which is due to the torque applied to the tire that significantly affects the tire control manner and accordingly the pneumatic trail. It is also seen that a driven tire yields a substantially higher aligning moment compared to the free-rolling tire (Figure 6.13). This is due to increasing the soil sinkage and soil shear zone happening under the driven tire on deformable terrains. The effect of drive torque on the cornering force of the tire, on the other hand, is relatively smaller, as seen in Figure 6.16. The effect of inflation pressure on the cornering force, however, becomes more pronounced under the higher side slip. Under the lower side-slip of 2°, the cornering force increases by only 3%, when the

inflation pressure is increased from 379 kPa (55 psi) to 758 kPa (110 psi). The corresponding increase in the force is in the order of 27% under the side-slip of 6° . This can be attributed to the higher lateral deformation of soil and soil shearing zone under high slip angle of 6° . The simulation results also revealed only minimal effect of inflation pressure on the overturning moment, irrespective of the side-slip angle, as seen in Fig. 6.17. The overturning moment of the free-rolling tire decreased slightly with the increase in the inflation pressure. Overturning moment relates to shift in the centre of vertical contact force. Increasing the tire inflation pressure decreases the contact area and tire distortion and accordingly the footprint shape change. However, this effect is minimal on soft soils which yields a slight decrease in the overturning moment. The observed trends for other soils are similar showing the minimal effect of inflation pressure on the cornering characteristics however the rate of decrease or increase is different based on the softness of the soil and shear deformation. The reports from the measured data for a radial-ply 12R22.5 heavy vehicle tire show similar trends for cornering characteristics of tires versus inflation pressure [Fancher, 1981].

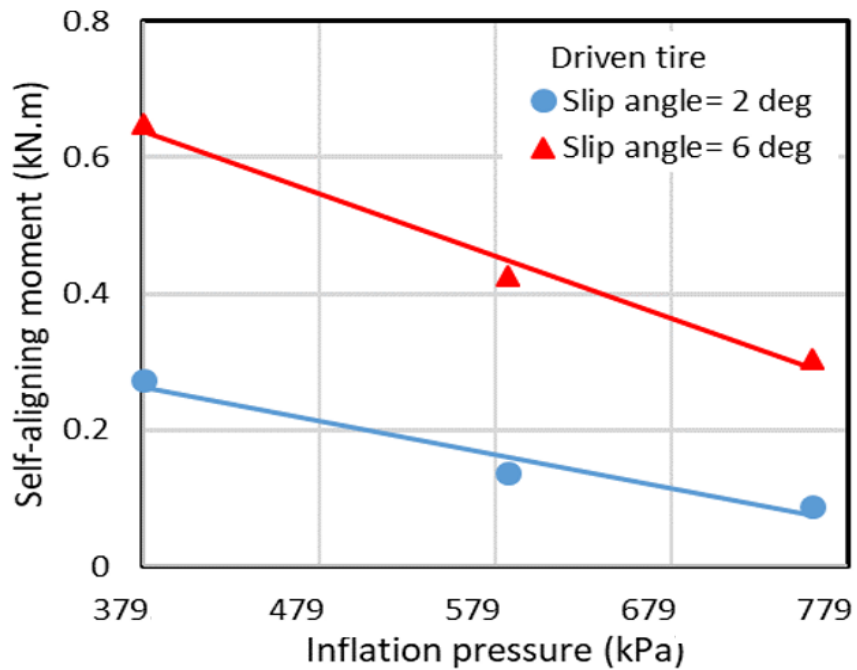


Figure 6.15. Influence of inflation pressure on self-aligning moment of the driven tire on the 25% moist sandy soil for two different slip angles (vertical load: 40 kN; speed: 15 km/h)

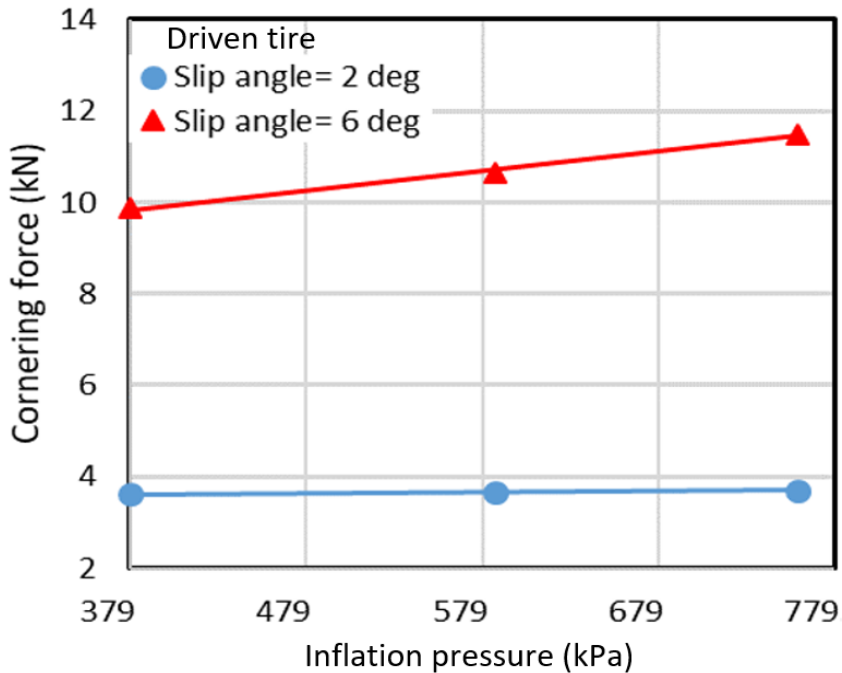


Figure 6.16. Influence of inflation pressure on cornering force of the driven tire on the 25% moist sandy soil for two different slip angles (vertical load: 40 kN; speed: 15 km/h)

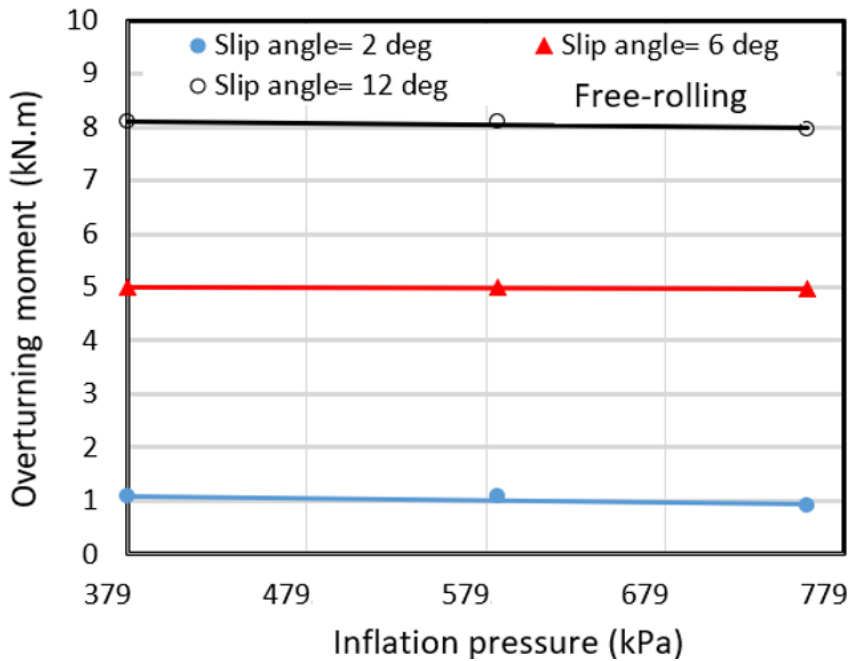


Figure 6.17. Influence of inflation pressure on overturning moment of the tire rolling freely on the 25% moist sandy soil for different slip angles (vertical load: 40 kN; speed: 15 km/h)

6.3.4 Effect of rolling speed

Studies reporting cornering properties of tires operating on non-deformable terrains have, invariably, shown minimal effect of speed on the cornering force developed by the tire [Shokouhfar, 2017; Longhouse, 1972]. The tire's interactions with deformable soils, however, are strongly affected by the mechanical properties of the soil, soil compaction and the speed. The effect of rolling speed on the resulting cornering properties of free-rolling as well as driven tires operating on deformable soils are thus investigated considering the soil compaction effect. For this purpose, the simulations are performed considering tires of the four axles vehicle. As an example, Figure 6.18 shows the effects of forward speed on variations in the self-aligning moments developed by the free-rolling tires of four axles operating on the sandy loam soil corresponding to 6 deg slip angle. Each tire in the simulation model is subjected to 40 kN vertical load and 758 kPa (110 psi) inflation pressure, and simulations are performed considering three different speeds (5, 10 and 15 km/h). The self-aligning moment developed by each tire generally increases with an increase in the forward speed. Tires of different axles, however, exhibit substantial differences in their aligning moment, which clearly show the effect of increasing soil compaction. The tire rolling speed affects the relative slip between the tire contact patch and the terrain, which could affect the tire cornering force and trail pneumatic, particularly under large side-slip angles and compacted soils. Since the cornering force shows a minimal change versus rolling speed in Figure 6.19, the pneumatic trail is the vital factor that is affected by rolling speed and changes the aligning moment accordingly.

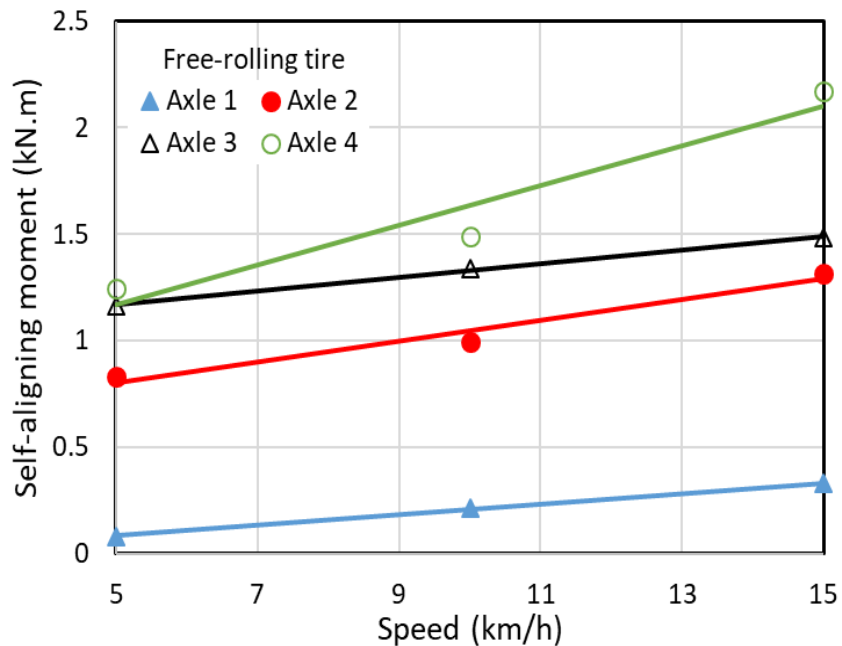


Figure 6.18. Influence of forward speed on the self-aligning moment of free-rolling tires of the four-axle vehicle model operating on the dry sandy loam soil (slip angle: 6 deg; inflation pressure: 758 kPa (110 psi); vertical load: 40 kN)

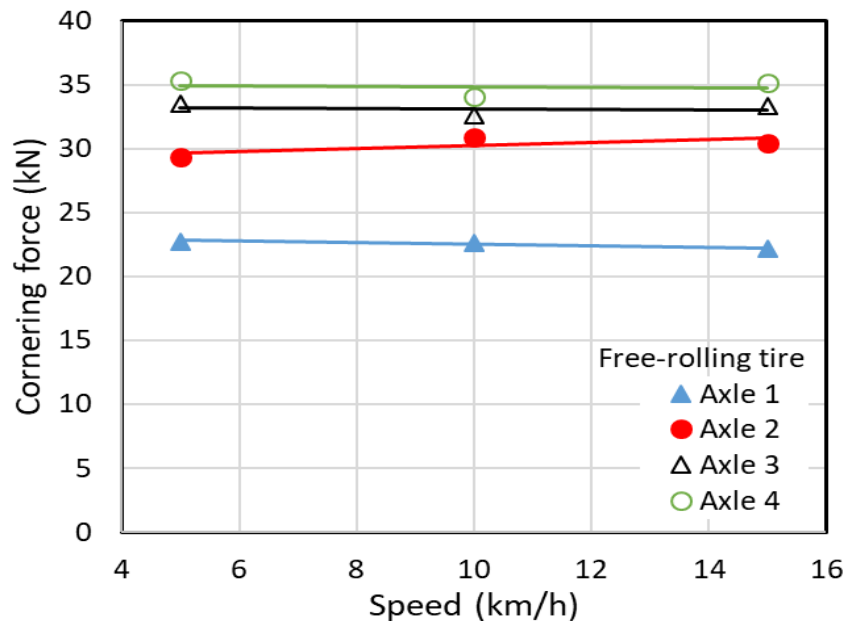


Figure 6.19. Influence of forward speed on the cornering force of free-rolling tires of the four-axle vehicle model operating on the dry sandy loam soil (slip angle: 6 deg; inflation pressure: 758 kPa (110 psi); vertical load: 40 kN)

The effects of rolling speed on the cornering forces and overturning moments developed by the tires are observed to be relatively small, as seen in Figures 6.19 and 6.20, respectively. Longhouser [1972] reported similar trends for the cornering force of a military truck tire at different speeds on dry and wet pavements.

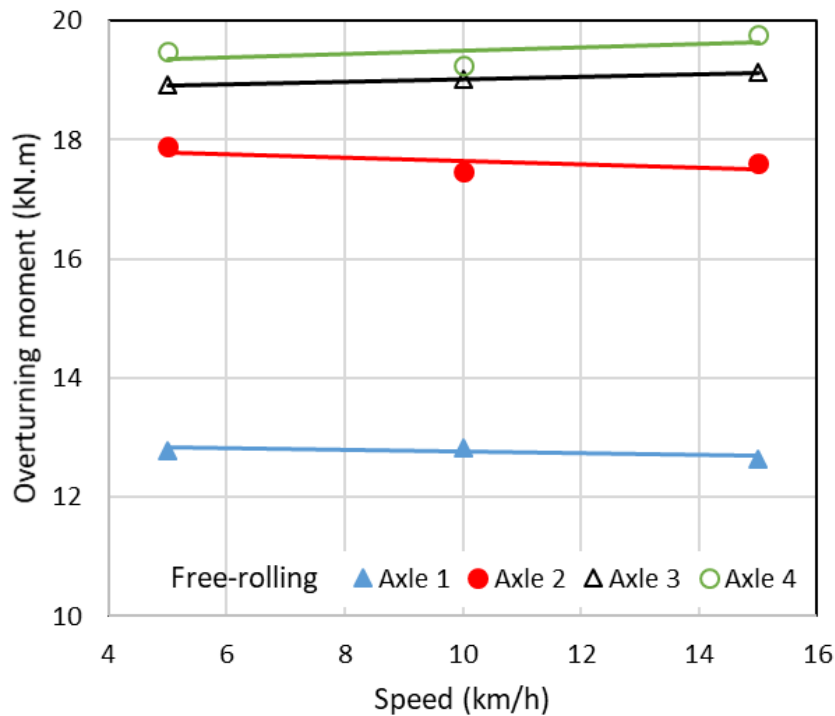


Figure 6.20. Influence of forward speed on the overturning moment of free-rolling tires of the four-axle vehicle model operating on the dry sandy loam soil (slip angle: 6 deg; inflation pressure: 758 kPa (110 psi); vertical load: 40 kN)

Effect of rolling speed on the cornering properties of tires are further investigated considering the soil compaction effect of driven tires operating on the dry sandy loam soil. Figure 6.21 shows the effect of speed on self-aligning moments of driven tires of four vehicle axles corresponding to 6 deg slip angle. Each tire is subjected to 758 kPa (110 psi) inflation pressure and 40 kN vertical load and different axles. The results generally suggest minimal effect of speed on the self-aligning moment developed by each tire. Progressively increasing compaction of the soil, however, yields notably higher self-aligning moment due to tires of axles 2, 3 and 4. Relatively higher effect of speed is observed on the aligning moment of the last axle's tire, which can attribute to greater soil compaction. The effects

of longitudinal speed on the self-aligning moments of the free-rolling tires, shown in Figure 6.18, are more significant than those of the driven tires. It could attribute to the effect of torque on the relative slip between tire and terrain. Figure 6.22 shows similar effects of speed on the cornering forces developed by the driven tires on the dry sandy loam soil. The cornering force due to the last axle tire increases with increase in vehicle speed due to greater soil compaction. The effect of speed on the cornering force developed by the other axles' tires are relatively small, as it is observed for the free-rolling tires (Figure 6.19). The results are obtained for other soils show the similar trends for cornering characteristics of free-rolling and driven tires versus rolling speed.

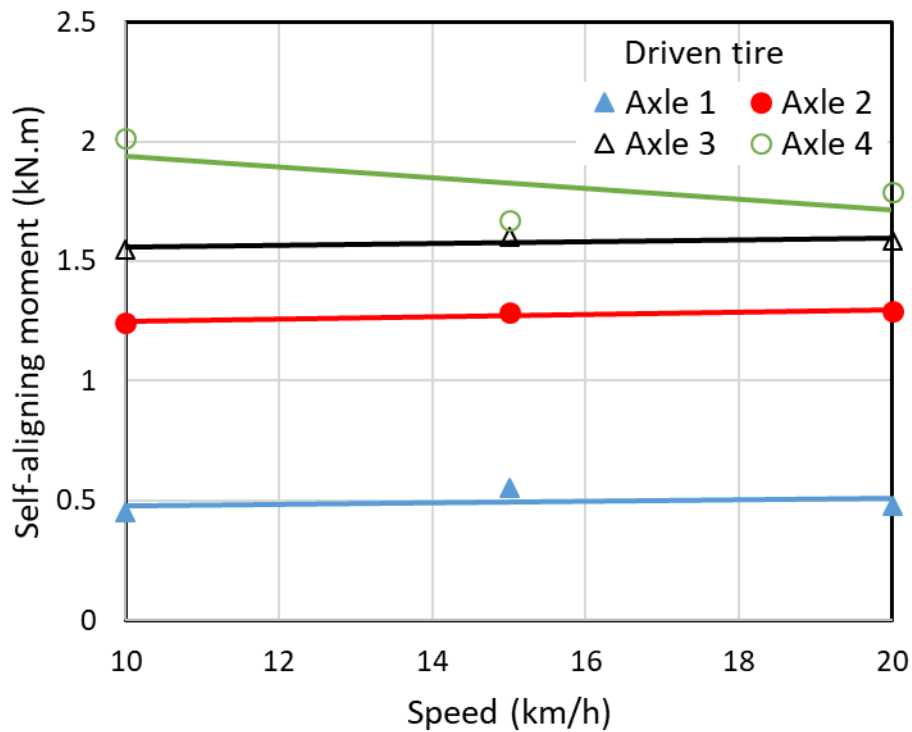


Figure 6.21. Influence of forward speed on the self-aligning moment of driven tires of the four-axle vehicle model operating on the dry sandy loam soil (slip angle: 6 deg; inflation pressure: 758 kPa (110 psi); vertical load: 40 kN)

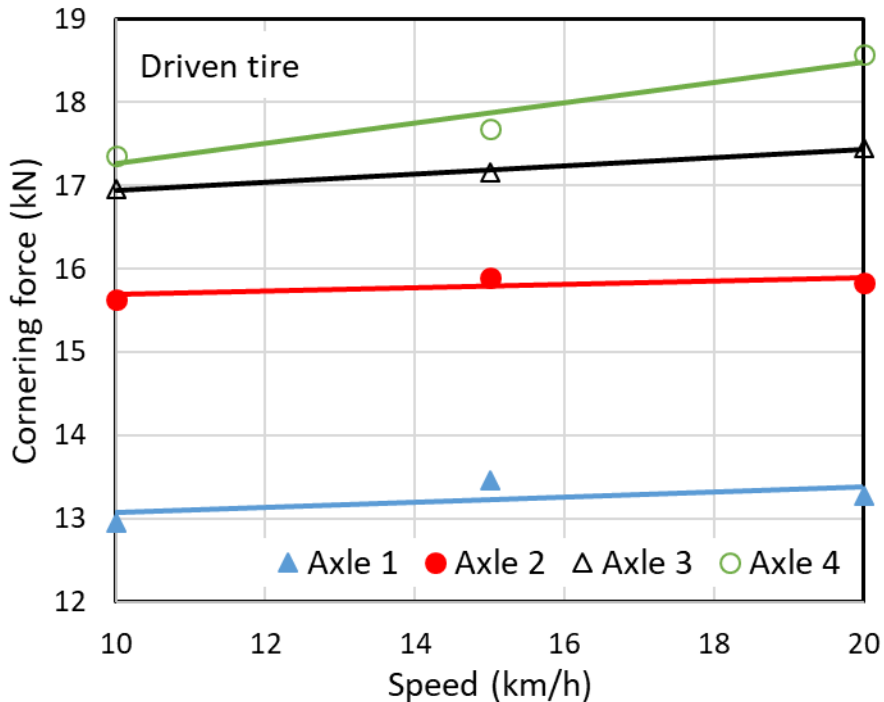


Figure 6.22. Influence of forward speed on the cornering force of driven tires of the four-axle vehicle model operating on the dry sandy loam soil (slip angle: 6 deg; inflation pressure: 758 kPa (110 psi); vertical load: 40 kN)

6.3.5 Effect of soil internal friction angle

The cornering properties of tires operating on soft soils are strongly affected by mechanical properties of the soil such as cohesion coefficient and internal friction angle. In this study, the effect of internal friction angle of the soil is evaluated on the cornering as well as overturning moment characteristics of the free-rolling and driven tires. The internal friction angle relates to the moisture content of the soil. A higher internal friction angle represents higher moisture content of the soil. Simulations are performed for three different internal friction angles of the soil, namely, 21, 21.36 and 29.4 degrees. Figures 6.23 and 6.24 show the effect of internal friction angle on self-aligning moment and cornering force, respectively, developed by the free-rolling tire for two different side-slip angles, namely, 2° and 6°. The results are obtained for the tire running at a speed of 15 km/h with 758 kPa (110 psi) inflation pressure and 40 kN vertical load. The results show both the cornering force and self-aligning moment increase with increase in the friction angle for both the side-slip conditions considered. For the 6°angle, the self-aligning moment and cornering

force increase by nearly 88% and 50%, respectively, when the internal friction angle is increased from 21 degrees to 29.4 degrees. This is attributable to greater wheel sinkage and compression of the soil with higher internal friction angle, which contributes to higher cornering force and thereby higher self-aligning moment. The overturning moment developed by the free-rolling tire also increases with increase in the internal friction angle, as shown in Figure 6.25. The figure shows variations in overturning moment as a function of the internal friction angle for three different side-slip angles (2° , 6° and 12°). Higher slip angle yields more significant increases in the cornering force, self-aligning moment and the overturning moment, which can be attributed higher side velocity of the freerolling tire.

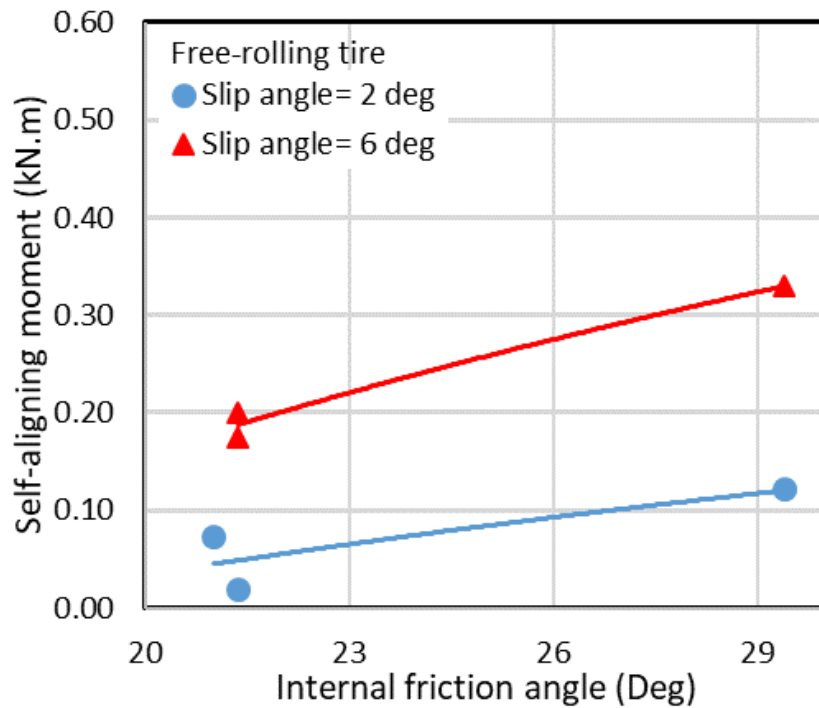


Figure 6.23. Influence of soil internal friction angle on the self-aligning moment developed by the free-rolling tire for two different slip angles (inflation pressure: 758 kPa (110 psi); vertical load: 40 kN; speed: 15 km/h)

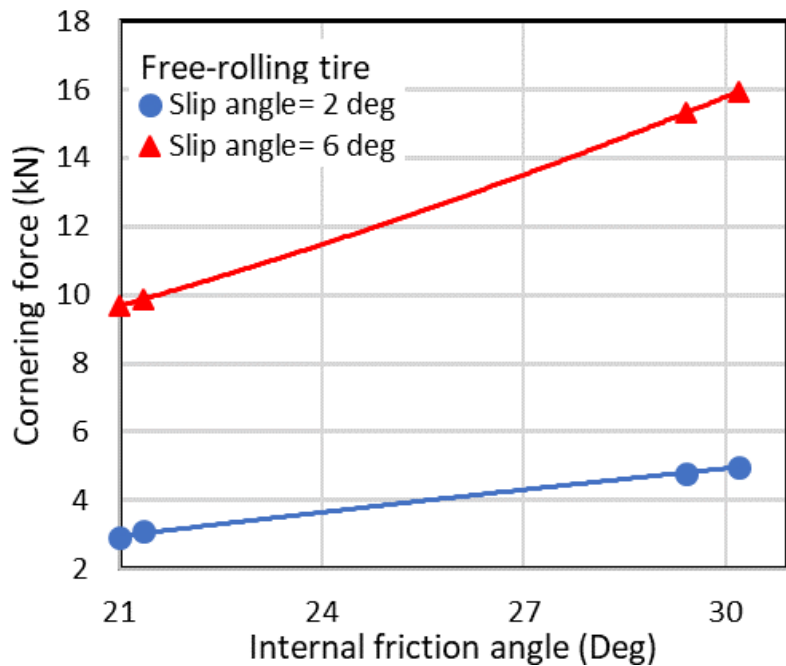


Figure 6.24. Influence of soil internal friction angle on the cornering force developed by the free-rolling tire for two different slip angles (inflation pressure: 758 kPa (110 psi); vertical load: 40 kN; speed: 15 km/h)

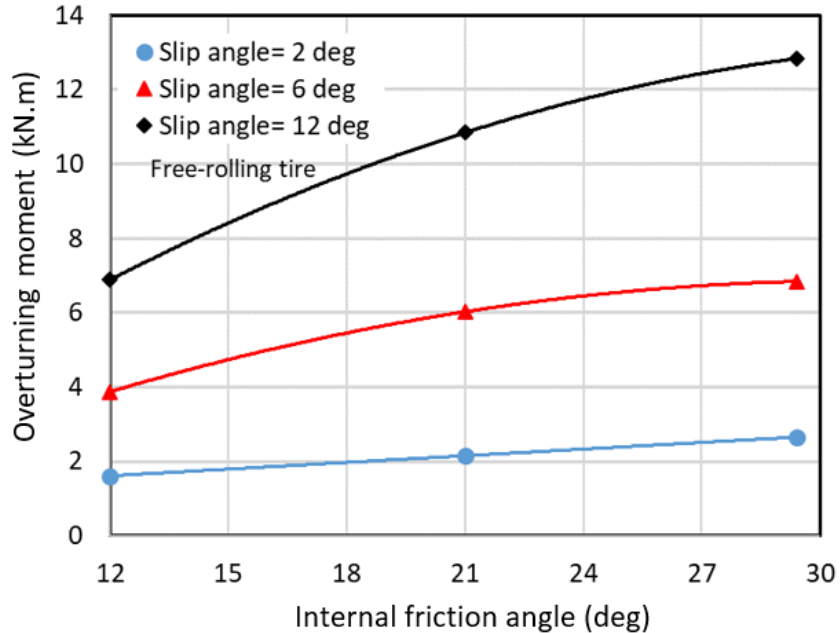


Figure 6.25. Influence of soil internal friction angle on the overturning moment developed by the free-rolling tire for different slip angles (inflation pressure: 758 kPa (110 psi); vertical load: 40 kN; speed: 15 km/h)

Figures 6.26 and 6.27 show the effect of internal friction angle on self-aligning moment and cornering force, respectively, developed by the driven-rolling tire for two different side-slip angles, namely, 2° and 6° . The results are obtained for the tire running at a speed of 15 km/h with 758 kPa (110 psi) inflation pressure and 40 kN vertical load, and the soil internal friction ranging from 21° to 30.19° . The self-aligning moment increases with increase in the soil internal friction angle, as seen in Figure 6.26, as it was observed for the free-rolling tire. This is due to additional friction of the soil with greater internal friction angle. The cornering force also increases with the internal friction angle, as seen in Figure 6.27. The observed trends in the cornering force and aligning moment, however, differ from those of the free-rolling tire (Figures 6.23 and 6.24), which is due to greater sinkage of the wheel in the soil in the presence of the drive torque.

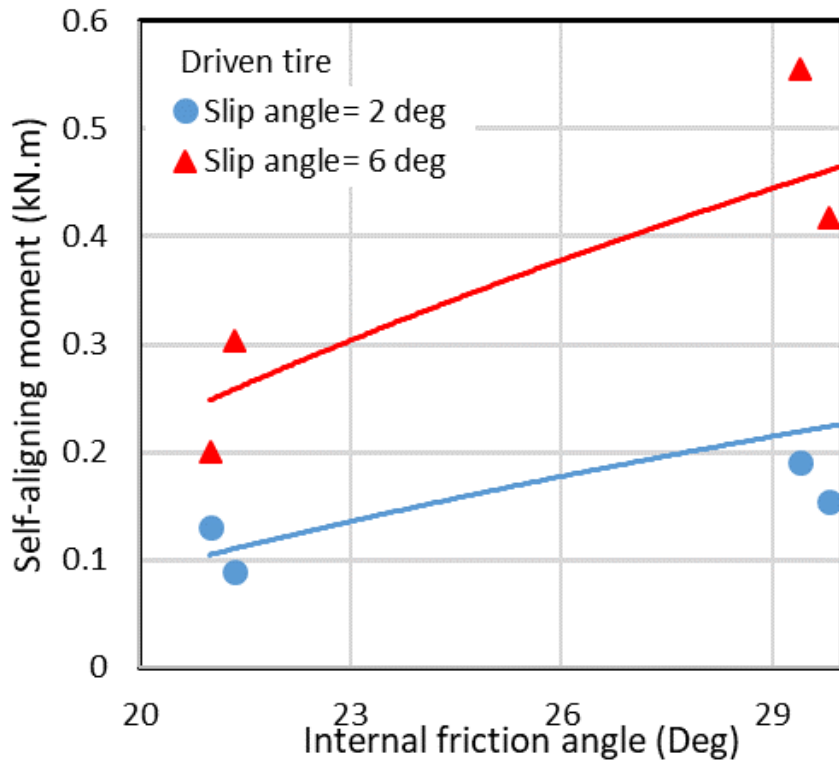


Figure 6.26. Influence of soil internal friction angle on the self-aligning moment developed by the driven tire for two different slip angles (inflation pressure: 758 kPa (110 psi); vertical load: 40 kN; speed: 15 km/h)

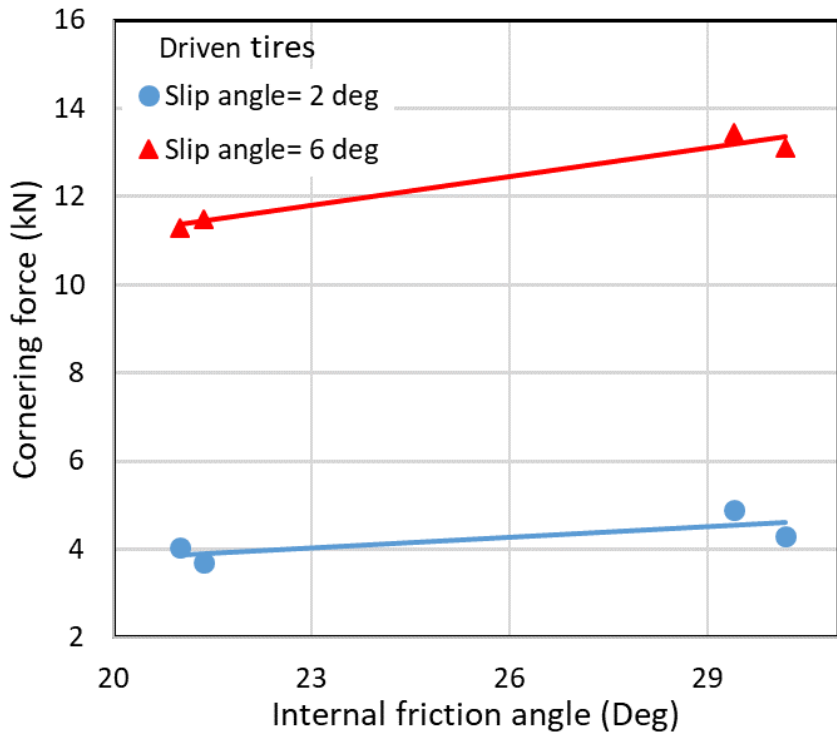


Figure 6.27. Influence of soil internal friction angle on the cornering force developed by the driven tire for two different slip angles (inflation pressure: 758 kPa (110 psi); vertical load: 40 kN; speed: 15 km/h)

6.3.6 Effect of soil compaction

Simulations are performed to investigate the effect of soil depth, a measure of soil compaction, on the cornering properties of free-rolling as well driven tires. Figures 6.28 and 6.29 show the variation in the self-aligning moment as a function of soil depth for the free-rolling tire and the driven tire, respectively, operating on the sandy loam soil. The results are obtained for the tires at a speed of 15 km/h speed, while the inflation pressure and vertical load are held as 758 kPa (110 psi) and 40 kN, respectively. The figures illustrate the aligning moment responses for two different slip angles, namely, 2° and 6°. The results suggest nearly linear increase in the self-aligning moment with increase in soil sinkage for both the free-rolling as well as driven tires. Same tendency is evident for both the slip angles considered, although the rate of change moment with respect to sinkage is substantially higher for the higher side-slip. This is attributable to higher side velocity of the tire subjected to higher side-slip.

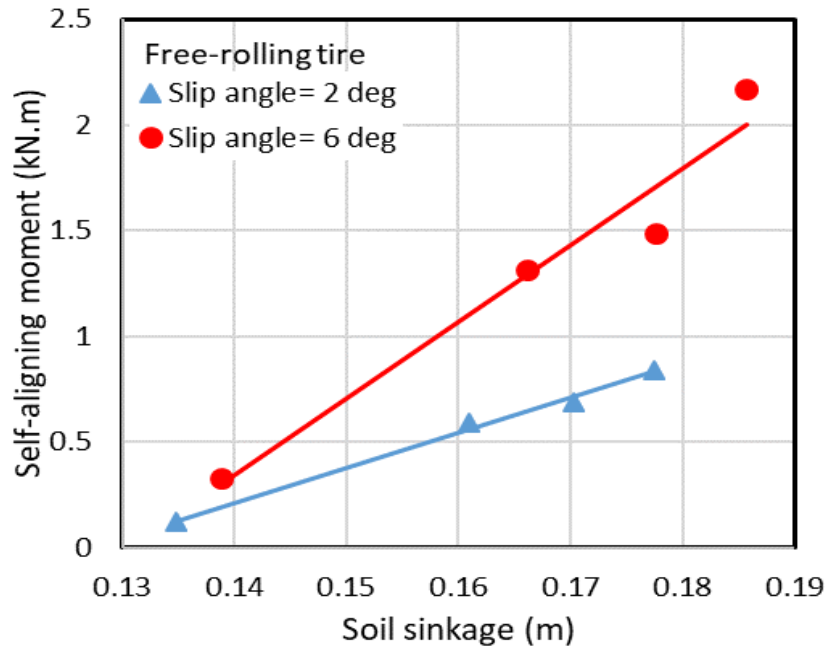


Figure 6.28. Influence of soil sinkage on the self-aligning moment of the free-rolling tire operating on the dry sandy loam soil at 15 km/h speed, 758 kPa (110 psi) inflation pressure, and 40 kN vertical load

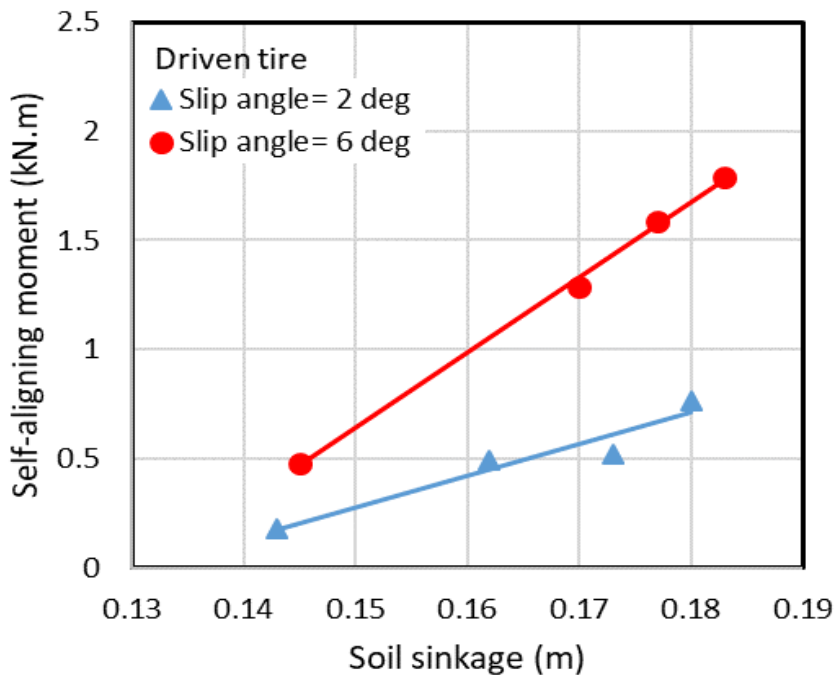


Figure 6.29. Influence of soil sinkage on the self-aligning moment of the driven tire operating on the dry sandy loam soil at 15 km/h speed, 758 kPa (110 psi) inflation pressure, and 40 kN vertical load

The effect of soil sinkage on the cornering force responses of the free-rolling and the driven tires are illustrated in Figures 6.30 and 6.31, respectively, for 2° and 6° side-slip angles. The results suggest highly nonlinear effect of sinkage with regard to tire side-slip. The cornering force of the free-rolling as well as driven tire is insensitive to wheel sinkage under the low slip angle of 2° . Under this side-slip condition, increasing the wheel sinkage yields slight reduction in the cornering force of the driven tire, while the effect is negligible for the free-rolling tire. The wheel sinkage, however, yields significant effect on cornering force under the higher side-slip of 6° . In this case, the cornering increases considerably with increase in the wheel sinkage, as it is observed for the self-aligning moment. Moreover, the cornering increases nearly linearly with the wheel sinkage, as it is also observed for the aligning moment. The wheel sinkage also revealed similar effects on the overturning moment, as seen in Figure 6.32.

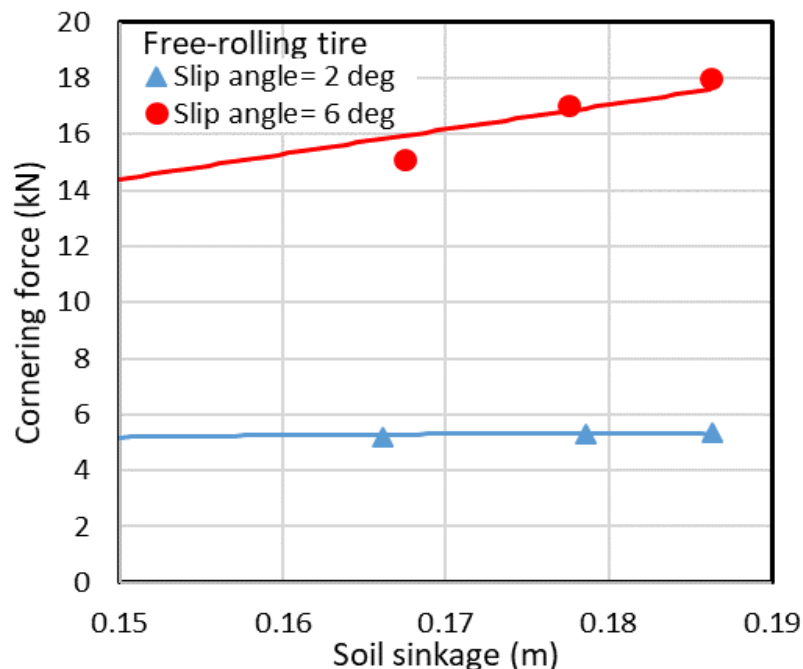


Figure 6.30. Influence of soil sinkage on the cornering force of the free-rolling tire operating on the dry sandy loam soil at 15 km/h speed, 758 kPa (110 psi) inflation pressure, and 40 kN vertical load

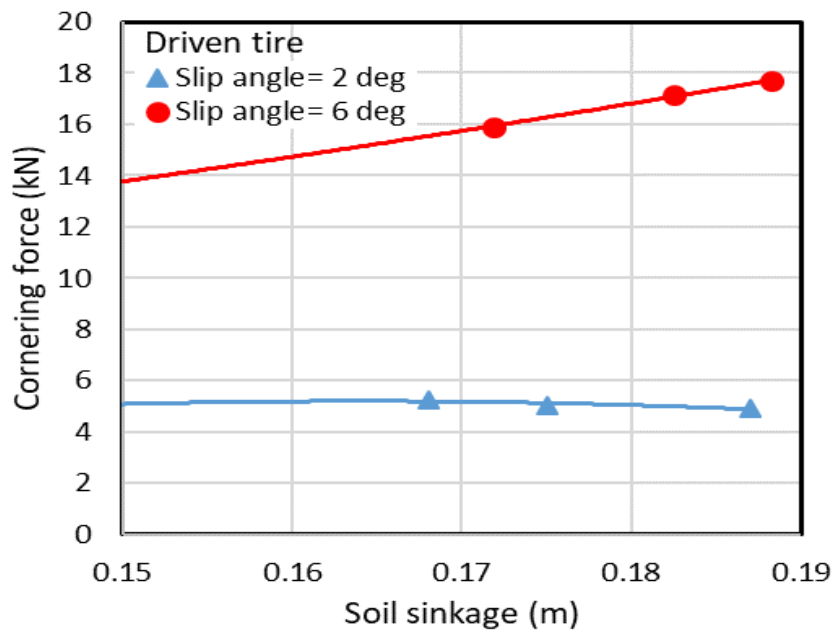


Figure 6.31. Influence of soil sinkage on the cornering force of the driven tire operating on the dry sandy loam soil at 15 km/h speed, 758 kPa (110 psi) inflation pressure, and 40 kN vertical load

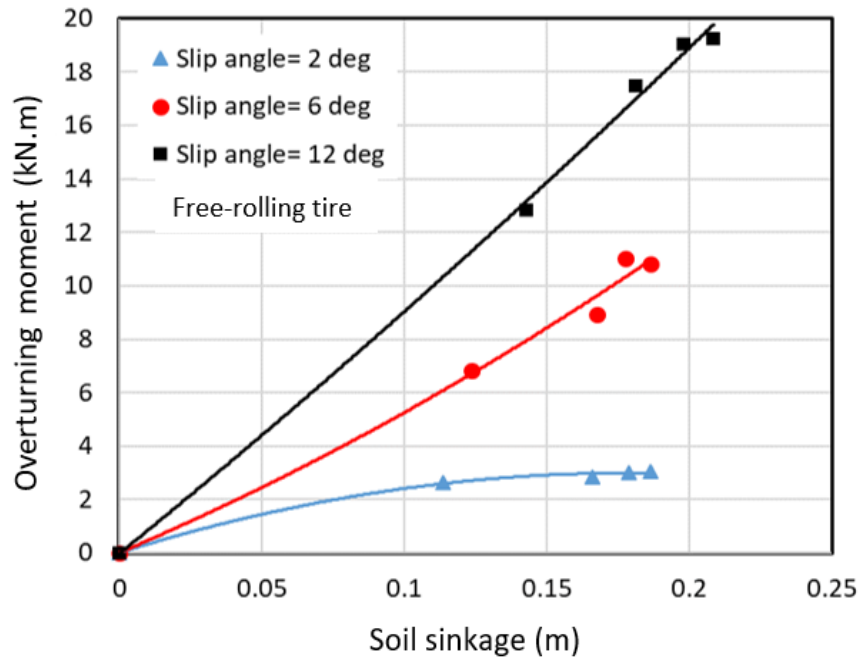


Figure 6.32. Influence of soil sinkage on the overturning moment of the free-rolling tire operating on the dry sandy loam soil at 15 km/h speed, 758 kPa (110 psi) inflation pressure, and 40 kN vertical load

6.4 The development and validation of cornering characteristics relationships using genetic algorithm

Genetic algorithms are used to derive mathematical relations between the cornering properties of the tires and the essential soil factors and operating conditions, as described in section 5.4 with regard to the rolling resistance. The primary motivations for deriving such relationships is to predict cornering properties of free-rolling and driven tires as functions of operating conditions, which would permit directional response analyses of off-road vehicles in a computationally efficient manner. For this purpose, the simulation results obtained from the FEA-SPH tire-soil interaction models are utilized to relationships for predicting the cornering force, self-aligning moment, and overturning moment developed by the free-rolling as well as driven tires for a range of operating conditions including the soil factors. The identified mathematical relations are intended to replace a portion of the rigid ring tire model [El-Sayegh, 2020] and the Pacejka magic formulae that are currently used in the Volvo Transportation Model (VTM). It should be noted that the rigid ring tire model exhibits notable limitations when the tire interacts with moist soils. Moreover, it does not permit analyses under the multi-pass conditions [El-Sayegh, 2020].

Following mathematic relations were obtained for the cornering force, aligning moment and the overturning moment as functions of the essential operating factors using the genetic algorithm.

$$F_y = 28.1dF_z\phi\alpha + 11220v\sin(9.98\alpha) + 13.27c\alpha\phi^2 - 3.45T\alpha \quad (6.1)$$

$$M_z = 17.5v\alpha + 7.5dF_z\phi\alpha + 1000\sin(0.00012vc\alpha - 3.5e^{-13}\alpha T^3) - 5e^{-3}F_z\alpha - 2e^{-8}\phi\alpha T^3 \quad (6.2)$$

$$M_x = 57.3 \phi \sin(5.72 e^{-5}c\alpha + 0.115 v\alpha + 2.97 e^{-4}dF_z\alpha - 1.37e^{-8} \alpha T^2) \quad (6.3)$$

for cornering force F_y , is the self-aligning moment M_z and overturning moment M_x , respectively, as functions of important operating factors that include the vertical load F_z in N, forward velocity v in m/s, soil cohesion C in Pa, soil shear resistance ϕ in rad, soil depth d in m, drive torque T in N.m, and slip angle α in rad. It should be noted Equations (6.1) to (6.3) describe the regression relations that the pressure has minimal effect on cornering characteristics of the tire. The simulation results showed that the cornering force and

overturning moment are least sensitive to variations in inflation pressure, which is evident in Figures 6.14, 6.16 and 6.17. The effect of pressure was also judged to be relatively small on the self-aligning moment. It is recommended that for the effectiveness of GA models and making a more versatile model for a larger class of tires, the tire design factors should be considered since the tire properties are also affected by the design factors such as tire construction and material properties of the constituents.

The optimal solution Eureqa generated for the cornering force is characterized by two parameters: The Size (complexity) and the Fit (accuracy) on the validation data. By default, Eureqa ranks answers based on a complexity-to-accuracy ratio; solutions that are correct but not overly complicated are displayed at the top. The training set is a portion of input data that Eureqa uses to find solutions. The validation data is represented by a separate subset that is exclusively utilized to determine accuracy of the formulations.

It's noted that the method of identifying the relations involves 312 outputs in its population and eight inputs for each output. The goodness of fit (R-square) for the cornering force was determined as 0.96, while the correlation coefficient was 0.98 with the mean square error of 2.52. The goodness of fit (R-square) for the self-aligning moment relationship was determined as 0.8 with correlation coefficient of 0.98 and a mean square error of 0.0056. The GA overturning moment equation revealed the R-square value of 0.93 with correlation coefficient of 0.98 and the mean absolute error of 0.55.

Table 6.1 shows the sensitivity of each parameter on the cornering force, self-aligning moment, and overturning moment. The sensitivity analysis of operating conditions on the cornering force showed that the cornering force is highly affected by changes in the slip angle variable with 0.835 sensitivity, as would be expected. It was further noticed that the cornering force is least affected by a change in the longitudinal speed (sensitivity: 0.0817).

The sensitivity analysis of operating conditions with regard to self-aligning moment showed that the self-aligning moment is highly affected by changes in the soil depth with 1.075 sensitivity and least affected by the tire speed and the vertical load with 0.097278 and 0.097275 sensitivity, respectively.

Based on the sensitivity of each parameter on the overturning moment, it is noted that the overturning moment is least affected by the inflation pressure. The inflation pressure is thus not included in the overturning relationship. It is also noted that the slip angle is the most effective parameter on the overturning moment, while the speed shows the least effect on the overturning moment.

Table 6.1. Sensitivity analysis of GA equation parameters on the cornering characteristics

Variable	Cornering force sensitivity	Self-aligning moment sensitivity	Overturning moment sensitivity
α	0.83442	0.56617	0.8384
d	0.35893	1.075	0.3279
ϕ	0.31473	0.72398	0.3214
F_z	0.18493	0.097275	0.1982
c	0.101	0.25063	0.1063
T	0.08832	0.18683	0.1200
v	0.081677	0.097278	0.0520

The effectiveness of the mathematical relations developed for the cornering force, self-aligning moment and overturning moment were evaluated by performing additional cornering tests on the mud. The simulations were carried out with a free-rolling tire in an SPH soil channel under 40 kN vertical load and 758 kPa (110 psi) inflation pressure of the first, second, third, and fourth axle tires rolling at two different speeds (0 km/h and 15 km/h). The tests were limited to two different side-slip angles, namely, 6° and 12°. Relatively higher slip angles were chosen to examine the validity of the mathematical relations since the simulation results revealed important effects of most of the operating factors under the higher slip angle. Figure 6.33 illustrates the correlations between the simulated and predicted cornering force responses of the tires at the mentioned operating conditions. The results show that the GA model-predicted cornering force responses are highly correlated with those obtained the FEA-SPH simulation models ($R^2 \approx 0.98$). Similar degree of correlation is also observed for the GA model-predicted self-aligning and

overturning moments with those obtained from the FEA-SPH simulation models ($R^2 \approx 0.95$ - 0.97), as seen in Figures 6.34 and 6.35, respectively.

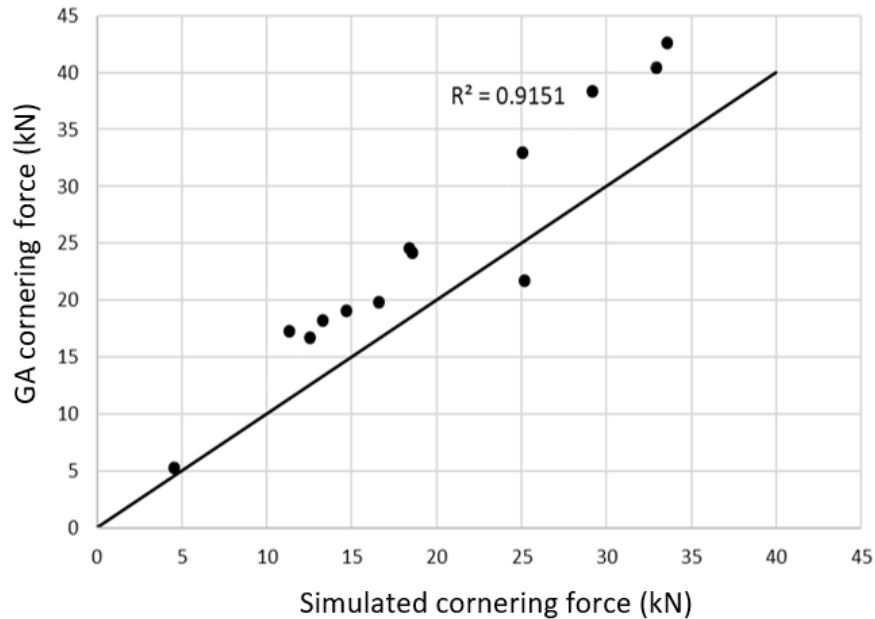


Figure 6.33. Correlations of the cornering force predicted from the identified mathematical relations with those predicted from the FE-SPH simulation model.

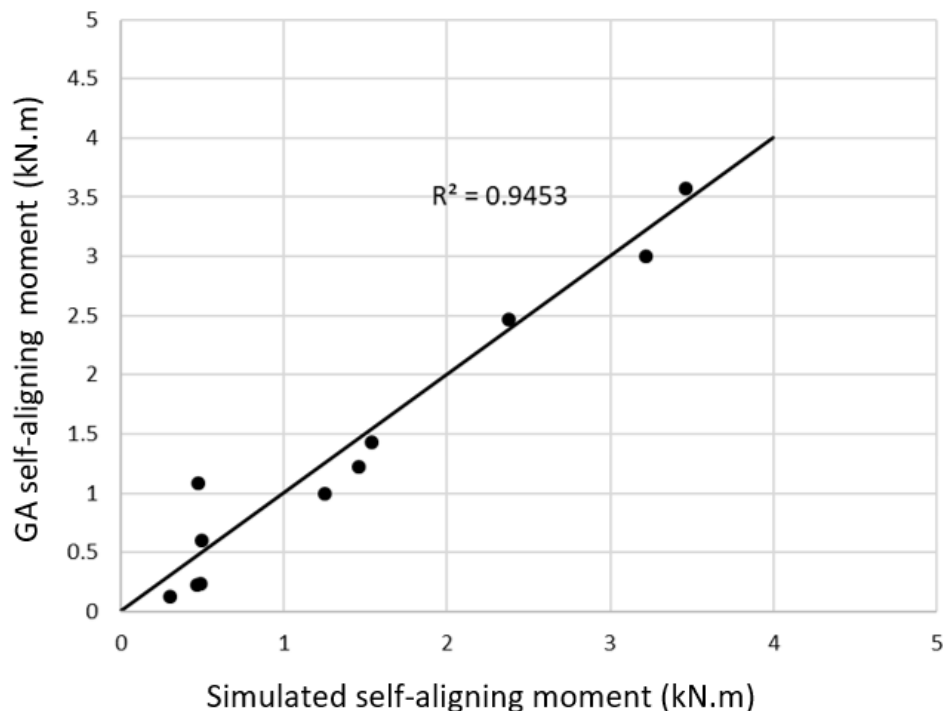


Figure 6.34. Correlations of the self-aligning moment predicted from the identified mathematical relations with those predicted from the FE-SPH simulation model.

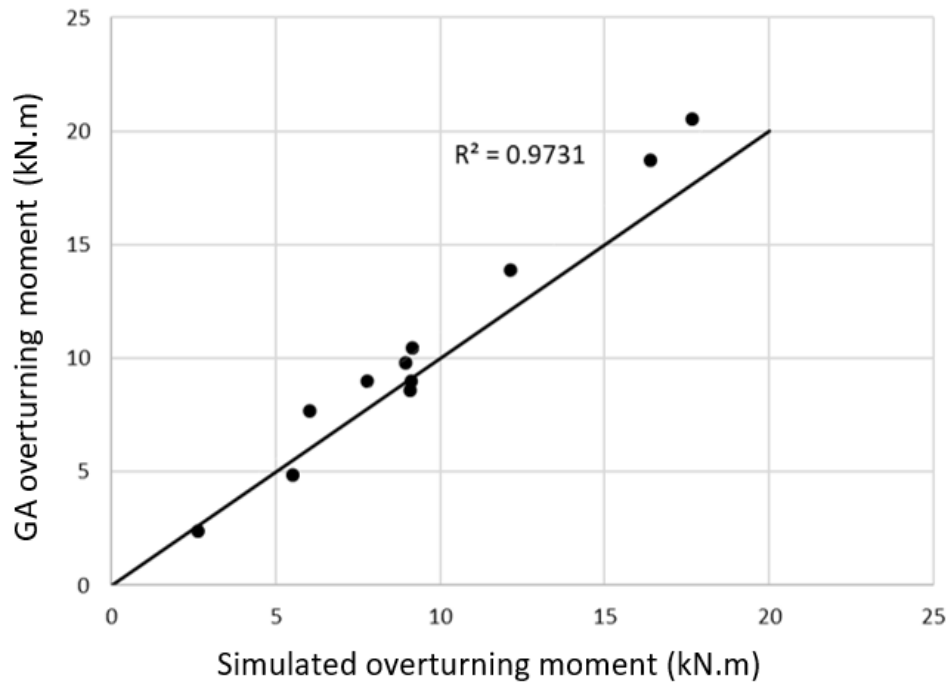


Figure 6.35. Correlations of the overturning moment predicted from the identified mathematical relations with those predicted from the FE-SPH simulation model.

6.5 Summary

The cornering characteristics for the RHD truck tire (315/ 80R22.5) were analyzed under various terrain-related factors and operating conditions. The SPH approach was used to calibrate the soil models considered in the study, as it was described in Chapter 3. This chapter focused on analyses of tire-terrain interactions relevant to cornering properties of the tire, specifically, the cornering force, self-aligning moment, and the overturning moment under free-rolling and driven conditions and a wide range of operating situations. The operating factors included the tire inflation pressure, vertical load, speed, soil compaction, and soil mechanical characteristics such as cohesion, angle of resistance and depth. The cornering force of the free-rolling tire was found to be highly dependent on the soil compaction. The tire speed, on the other hand, revealed relatively less impact on the cornering force. The results revealed highest self-aligning moment under higher soil compaction. Trends observed in the overturning moment were identical to those noted for

the cornering force over the entire ranges of operating conditions considered in the study. The tire overturning moment was observed to be highly dependent on soil compaction, while the tire speed had a minimal impact on the overturning moment.

The simulation results were used to develop mathematical relations for the cornering force, self-aligning moment, and overturning moment as functions of important operating factors using advanced algorithm techniques through training, testing and validations in the Pam-Crash simulation platform. Cornering tests were performed for the RHD tire operating over the mud soil to examine the validity of the GA-based cornering force, self-aligning moment, and overturning moment relationships. It was concluded that the identified mathematical relations could provide very good estimations of the cornering characteristics under a broad range of operating conditions and soils ($R^2 \approx 0.95-0.98$).

CHAPTER 7

MAJOR CONCLUSIONS AND CONTRIBUTIONS

7.1 Major contributions of the thesis

The thesis research focused on the development of a comprehensive dynamic tire-soil interactions model for investigating tires' interactions with deformable soils considering a wide range of operating and soil factors. The major contributions of the study are summarized below:

Owing to the excessive computational demands posed by the FEA-SPH tire-soil models, the thesis proposed a unique mathematical relationship for estimating the rolling resistance coefficient of the free-rolling as well driven truck tires in an efficient manner. A methodology based on genetic algorithms is employed to derive the relationship considering different soil properties and a broad range of operational factors. The soils included the clay loam, dense sand, clayey soil, sandy, moist sand with varying moisture content (10%, 25%, and 50%). The operating conditions included the inflation pressure, vertical load, speed, torque, and multi-pass effect. The effectiveness of the proposed rolling resistance coefficient relationship is also demonstrated under different operating conditions. The proposed relationship could be implemented to the total vehicle model for assessing rolling resistance under different operating conditions in a computationally efficient manner.

The methodology based on genetic algorithms is further applied to develop novel relations for predicting cornering characteristics of the tire operating on different types of soils. The relationships are derived for predicting cornering force, self-aligning moment and overturning moment of free-rolling as well as driven tires as functions of the side-slip angle. The validity of the proposed relations is examined for a range of operating conditions, such as vertical load, speed, torque, the multi-pass effects, and soils, namely, clay loam, dense sand, clayey soil, sandy, moist sand with varying moisture content (10%, 25%, and 50%).

7.2 Major conclusions

In this study, the tire-soil interaction model was developed by integrating the comprehensive FEA model of a truck tire with SPH models of different soils. The validity of the FEA tire model was examined by performing different static and dynamic tests, such as the drum-cleat, vertical stiffness, and footprint tests. The validity of the model was demonstrated by comparing the simulation results with the published data. The comparisons generally showed good agreements between the model-predicted static and dynamic responses with the available data. For the static vertical stiffness, comparisons revealed a maximum deviation of about 2.3%, which was observed under 586 kPa (85 psi) inflation pressure. The peak errors for the 758 kPa (110 psi) and 896 kPa (130 psi) inflation pressure were in the order of 3.1%. The results obtained from the footprint tests of the FEA model also showed reasonably good agreements with the available data for the same tire. The results obtained from the drum-cleat tests of the RHD tire model revealed that fundamental vertical mode frequency ranges from 53 Hz to 59 Hz for the range of inflation pressure considered in the study. The corresponding fundamental horizontal mode frequency ranged from 52 Hz to 57 Hz. The model-predicted fundamental vertical and horizontal modes frequencies were observed to lie within the ranges of frequencies reported in earlier studies. The simulation results also showed higher vertical tire stiffness and thus the fundamental vibration mode frequencies with increasing inflation pressure. It also showed a slight non-linear relationship between the vertical load and deflection that can be considered a linear trend.

The soil was modeled using the Smoothed-Particle Hydrodynamics technique. The models for different soils were subsequently formulated through calibrations involving pressure-sinkage and shear-strength tests. The model calibrations were conducted for a number of soils that are often encountered during off-road driving. These included the clay loam, dense sand, and clayey soil. The validity of the calibrated models was examined using the available terramechanics data. Experiments were designed and performed for calibration and validations of the clay loam soil model. The experiments were performed using a portable bevameter and a shear box in a soil bin in the terramechanics laboratory of Urmia University in Iran. The comparisons of the measured pressure-sinkage and shear strength

test data with the simulation results showed that the SPH soil model was successfully calibrated.

The FEA tire model and the SPH soil model were utilized to predict and analyze the rolling resistance coefficient and cornering characteristics of free-rolling as well as driven tires under different operating conditions. The predicted cornering force, self-aligning moment, and overturning moment simulation data were then used to develop relationships using genetic algorithms through training and testing. The input parameters were the longitudinal speed, torque, inflation pressure, vertical load, and slip angle; in addition to the terrain characteristics such as cohesion, friction angle, and depth.

The simulation results showed that the vertical load has a significant impact on the rolling resistance coefficient. The rolling resistance coefficient is less affected by tire inflation pressure at low vertical loads and more affected by it at high vertical loads. The truck tire was found to have the greatest rolling resistance coefficient at a lower internal friction angle when operating over different terrains. It was also discovered that the free-rolling tire's cornering force was highly dependent on soil compaction. The influence of tire speed on the cornering force, on the other hand, was rather minor. The results demonstrated that increased soil compaction resulted in the highest self-aligning moment. Under all operating conditions evaluated in the study, the overturning moment followed the same trends as the cornering force. The overturning moment of a tire was shown to be highly dependent on soil compaction, while tire speed had only a minor influence.

It was concluded that the GA cornering characteristics equations were able to predict the cornering characteristics at different operating and terrain conditions with an R-square fitness of greater than 0.8. It was also found that there is a minimal effect of the inflation pressure on the cornering characteristics. Hence, the inflation pressure parameter didn't appear in the GA equations. The most effective parameter on the cornering force and the overturning moment was the slip angle, as expected, while soil depth was the most effective parameter on the self-aligning moment. As the tire sinkage increased the cornering force, self-aligning moment, and the overturning moment all increased at a given operating condition.

It was also found that for the RRC relationship the R-square goodness of fit is 0.911, the mean error is 0.201, the mean square error is 0.0015 and the mean average error is 0.022. It was concluded that the rolling resistance coefficient varies linearly concerning vertical load, as the vertical load increase the rolling resistance coefficient increases as well. The same observation was found for the cornering force as a function of vertical load. Furthermore, the inflation pressure was concluded to have a greater effect on the rolling resistance than the cornering force. As for the effect of the tire multi-pass described by the tire sinkage, it was noticed that as the tire sinkage increases the rolling resistance coefficient increases.

7.3 Future works

The work done to achieve the aims of this thesis includes a wide range of engineering and science topics. The greatest effort has been put in a certain amount of time in order to simulate each test as accurately as feasible. The techniques, modeling and testing setup, and actual experiments, on the other hand, may continually be improved and modified. Tire modeling and evaluation is a factor that can be considered to improve the tire-terrain interaction results. For this purpose, it is suggested that tire evaluation tests be performed experimentally to provide a more accurate reference for evaluating the tire model. Tire material is another parameter that has not been accessible. The materials used for the tire model were the result of experiments by previous researchers, which were used with optimization methods for the most accurate modeling. Access to tire materials provides a more realistic and accurate model of the tire.

It is recommended that experimental pressure-sinkage and shear-strength tests of 10% moist sand, 25% moist sand, and 50% moist sand, such as tests performed for clay loam soil, be performed to provide more accurate calibration of the test soils. For soil modeling, it is also suggested to study the particle layering method to cover a wide range of soils. For example, clay loam soil can be modeled according to the percentage of its components.

It is recommended that the developed equations for cornering force, self-aligning moment, and overturning moment should be validated using physical testing since the equations are mainly based on simulation results.

It is recommended for future work to investigate the effect of slip angle on the longitudinal force. This will allow for better modeling of the longitudinal force during the cornering maneuver.

Regarding the developed genetic equations, it is suggested that the tire design parameters such as tire size, tire tread, etc. be considered in order to extend the equation to more comprehensive conditions. Therefore, it is recommended that all cornering and rolling resistance tests performed on the RHD truck tire be performed on another tire with different design characteristics. Cornering tests on other terrains such as snow, flooded surface, and mud can also help to integrate the GA equations.

7.4 Publications

Gheshlaghi, F., El-Sayegh, Z., El-Gindy, M., Oijer, F. et al., "Advanced Analytical Truck Tires-Terrain Interaction Model," SAE Technical Paper No. 2021-01-0329, April 13- 15, Detroit Michigan, USA, (2021), <https://doi.org/10.4271/2021-01-0329>.

Gheshlaghi, F., El-Sayegh, Z., El-Gindy, M., Oijer, F. et al., "Analysis of off-road tire cornering characteristics using advanced analytical techniques" Tire Society Journal, Oct 2021, USA, (Under review).

Gheshlaghi F., El-Sayegh Z., El- Gindy M et al. 'Prediction and validation of terramechanics models for estimation of tyre rolling resistance coefficient". Int. J. Vehicle Systems Modelling and Testing, 14, no. 3-4 (2020) 1-12.

Gheshlaghi, F., Rakheja, S., El-Gindy, M., "Tire-Terrain Interaction Modeling and Analysis: Literature Survey" Int. J. Vehicle Systems Modelling and Testing, (To be submitted).

REFERENCES

1. Goodyear, C. (1853) “Gum-Elastic and its Varieties: With a Detailed Account of its Applications and Uses and of the Discovery of Vulcanization”, Vol. 2, Harvard University, Published for the author.
2. <https://www.treadwright.com/blogs/treadwright-blog/the-history-of-tires>
3. Gheshlaghi F., Mardani A., Mohebi A. (2020) “Investigating the effects of off-road vehicles on soil compaction using FEA-SPH simulation”. Int. J. of Heavy Vehicle Systems, 14 N1:1-10 (DOI: 10.1504/IJHVS.2020.10027405)
4. Slade et al., (2009) “Off-road Tire-Soil Modeling using Finite Element Analysis Technique”, ASME International Design Engineering Technical Conference, August 30, 2009, San Diego, California.
5. Schmeitz, A. (2004) “Semi-Empirical Three-Dimensional Model of the Pneumatic Tyre Rolling over Arbitrarily Uneven Road Surfaces”. PhD thesis, Delft University of Technology, 2004.
6. Lugner, P. and Plochl, M. (2005) “Tyre model performance test: first experiences and results,” Vehicle System Dynamics, vol. 43, no. suppl, pp. 48 – 62.
7. Padovan, J., (1977), “Numerical Simulation of Rolling Tires,” Tire rolling losses and fuel economy, an R & D Planning Workshop, October 19-20, series SAE conference proceedings P-74. pp. 87-94.
8. Olatunbosun, O.A., Bolarinwa, E.O., (2004) “FE Simulation of the Effect of Tire Design Parameters on Lateral Forces and Moments”. Tire Science and Technology, TSTCA, 2004. 32(3): p. 146-163.
9. Bolarinwa, E.O., Olatunbosun, O.A., and Burnett, M. (2004) “A Study of Tyre Cornering Behaviour using a Finite Element Model, in Computational Mechanics”, WCCM VI in conjunction with APCOM'04. 2004: Beijing, China.
10. El-Sayegh Z., Gheshlaghi F., Sharifi M., and Mardani A. (2019) “Development of an HLFS agricultural tire model using FEA technique”. SN Applied Sciences 1, no. 11: 1454.
11. Gheshlaghi F., Mardani A. (2021) “Prediction of soil vertical stress under the off-road tire using smoothed-particle hydrodynamics”. Journal of Terramechanics, Volume 95, Pages 7-14.
12. Dhillon, R.S. (2013) “Development of Truck Tire-Terrain Finite Element Analysis Models”, PhD thesis, University of Ontario Institute of Technology.
13. Vehicle Dynamics Terminology, SAE J670e, Society of Automotive Engineers, 1978.
14. Bekker, M. G. (1950). “Relationship between soil and a vehicle.” Society of Automotive Engineers, 4(3), 381-396
15. Gheshlaghi, F., El-Sayegh, Z., Sharifi, M., and El-Gindy, M., (2020) “Prediction and Validation of Terramechanics Models for Estimation of Tyre Rolling Resistance Coefficient,” Int. J. Vehicle Systems Modelling and Testing 14(3-4):1-12.

16. Fancher, S. Ervin, R.D., Winkler, C.B., and Gillespie, T.D. (1986) "A Fact Book of the Mechanical Properties of the Components for Single-unit and Articulated Heavy Trucks," Report No. DOT HS 807 125, National Highway Traffic Safety Administration, U.S. Department of Transportation.
17. Luty, W. (2011) "An analysis of tire relaxation in conditions of the wheel side cornering angle oscillations", *Journal of Kones* 18 (1): 325–332.
18. Pacejka, Hans B. (2006) "Tyre and vehicle dynamics (2nd ed.)" SAE International. p. 22. ISBN 978-0-7680-1702-1.
19. Lu, D., Guo, K., Wu, H., Moschus, N., Lu, X.-P. & Chen, S.-K. (2006) "Modelling of tire overturning moment and loaded radius", *Vehicle System Dynamics*, 44:sup1, 104-114.
20. Liu, C.H., and Wong, J.Y. (1996) "Numerical Simulations of Tire–Soil Interaction Based on Critical State Soil Mechanics," *Journal of Terramechanics*, vol. 33, no. 5.
21. Liu, C.H., Wong, J.Y., and Mang, H.A. (1999) "Large Strain Finite Element Analysis of Sand: Model, Algorithm and Application to Numerical Simulation of Tire–Sand Interaction" *Computers and Structures*, vol. 74, no. 3.
22. Hiroma, T., Wanjii, S., Kataoka, T. and Ota, Y. (1997) "Stress analysis using fem on stress distribution under a wheel considering friction with adhesion between a wheel and soil", *Journal of Terramechanics*, Vol. 34, No. 4, pp.225–233.
23. PAM System International (2000) Pam-Shock User Manual.
24. Chen Liang, Zhi Gao, Shengkang Hong, Guolin Wang, Bentil Mawunya Kwaku Asafo-Duho, Jieyu Ren, (2021) "A Fatigue Evaluation Method for Radial Tire Based on Strain Energy Density Gradient", *Advances in Materials Science and Engineering*, vol. 2021, Article ID 8534954, 12 pages. <https://doi.org/10.1155/2021/8534954>
25. Zumrat Usmanova, Emin Sunbuloglu. (2021) "Finite element method estimation of temperature distribution of automotive tire using one-way-coupled method", *Proc IMechE Part D: J Automobile Engineering* 1–12, IMechE, DOI: 10.1177/09544070211008757.
26. Jung, H., Park, W. and Jeong, K. (2018) "Finite Element Analysis of Tire Traction Using a Rubber-Ice Friction Model". *Open Journal of Applied Sciences*, 8, 495-505. doi: 10.4236/ojapps.2018.811040.
27. CrmN, S. T. and Wong, J. Y. (1988) "an approach to improving the prediction of pneumatic tire performance over unprepared terrain". Proc. 2nd Asia-Pacific Conf. ISTVS, pp. 293-302.
28. Chen, S. T. (1988) "Study of tire-terrain interaction using the finite element method". Unpublished Master of Engineering Thesis, Carleton University, Ottawa, Canada.
29. Wang, L. (1990) "Tire modelling using a three-dimensional finite element method". Unpublished Master of Engineering Thesis, Carleton University, Ottawa, Canada.
30. Nakashima, H., and Wong, J.Y. (1993) "A Three-dimensional Tire Model by the Finite Element Method," *Journal of Terramechanics*, vol. 30, no. 1.

31. Zhang, X., Rakheja, S., and Ganesan, R., (2001), “Estimation of tire-road contact pressure distribution based on nonlinear finite element analysis”, Heavy Vehicle Systems, Series B, International Journal of Vehicle Dynamics, Vol. 8 No.3/4, pp. 197-217.
32. Yan, X., (2003), “Nonlinear Three-Dimensional Finite Element Analysis of Steady Rolling Radial Tires,” Journal of Reinforced Plastics and Composites, Vol. 22, No.8. pp. 733-750.
33. Wu, G. Z., and He X. M., (1992), “Effects of Aspect Ratio on the Stresses and Deformations of Radial Passenger Tires,” Tire Science and Technology, TSTCA, Vol. 20, No. 2, pp. 74-82.
34. Chae, S., Chang, Y. P., El-Gindy, M., Streit, D. A., (2001), “Standing Wave Prediction of a Racing Car Tire,” CSME-MDE-2001, November 21-22, Montreal, Canada.
35. Chang, Y. P., El-Gindy, M., and Streit, D. A., (2002), “Influence of Tire Loading and Inflation Pressure on Standing Waves Phenomena using PAM-SHOCK,” a special issue on “New Development in Heavy Vehicle Simulation,” International Journal of Heavy Vehicle Systems.
36. Chae, S. (2006) “Nonlinear Finite Element Modeling and Analysis of a Truck Tire”, PhD thesis, The Pennsylvania State University.
37. Marjani, M. (2016) “Development of FEA Wide-Base Truck Tire and Soil Interaction Models”, PhD thesis.
38. El-Sayegh Z., Gheshlaghi F., Sharifi M., and Mardani A. (2019) “Development of an HLFS agricultural tire model using FEA technique”. SN Applied Sciences 1, no. 11:1454.
39. Jafari, S. (2018) “Transient In-plane Analysis of Lug Tire Traversing Rigid Obstacles and Validation of Finite Element Modeling by Experimental Tests”. Doctoral dissertation. (In Persian).
40. Xiong, Y., and Tuononen, A. (2015) “Rolling deformation of truck tires: Measurement and analysis using a tire sensing approach”, Journal of Terramechanics 61: 33–42, ISSN 0022-4898.
41. Xiong, Y., Tuononen, A.J., (2014) “A laser-based sensor system for tire tread deformation measurement” Meas. Sci. Technol. 25 (11), 115103.
42. De Beer, M., Maina, J.W., van Rensburg, Y., Greben, J.M. (2012) “Towardusing tire-road contact stresses in pavement design and analysis”. TireSci. Technol., 246–271.
43. Van Keulen, H., and C.G.E.M. Van Beek. (1971) “Water movement in layered soils a simulation model”. Neth. J. Agric. Sci. 19:138–153.
44. Rubin, J., and R. Steinhardt. (1963) “Soil water relations during rainfall infiltration: I. Theory”. Soil Sci. Soc. Am. Proc. 27:247–251.
45. Nujid, M. and Raihan Taha Professor, M. (2017) “A Review of Bearing Capacity of Shallow Foundation on Clay Layered Soils Using Numerical Method”. Available at: <http://www.ejge.com/2014/Ppr2014.072mar.pdf> (Accessed: 17 March 2017).
46. T. More, S. and Bindu, D. R. S. (2017) “Effects of mesh size on finite element analysis of plate structure”, *Certified International Journal of Engineering Science and Innovative Technology*, 9001(3), pp. 2319–5967. Available at: http://www.ijesit.com/Volume 4/Issue 3/IJESIT201503_24.pdf (Accessed: 17 March 2017).

47. Gingold, R.A., Monaghan, J.J., (1977) “Smoothed particle hydrodynamics: theory and application to non-spherical stars”. *Mon. Not. R. Astron. Soc.* 181 (3), 375–89. Bibcode:1977MNRAS.181..375G. <http://doi.org/10.1093/mnras/181.3.375>.
48. Liu GR, Liu MB (2003) “Smoothed particle hydrodynamics a meshfree particle method”. World Scientific Publishing, Singapore
49. Islam, N., Hawlader, B., Wang, C., Soga, K. (2019) “Large deformation finite-element modelling of earthquake-induced landslides considering strain-softening behavior of sensitive clay”. *Can Geotech J* 56:1003–1018.
50. Abe, K., Soga, K., Bandara, S. (2013) “Material point method for coupled hydromechanical problems”. *J Geotech Environmental Eng* 140:04013033. [https://doi.org/10.1061/\(asce\)gt.1943-5606.0001011](https://doi.org/10.1061/(asce)gt.1943-5606.0001011)
51. Soga, K, Alonso, E., Yerro, A. et al. (2017) “Trends in large-deformation analysis of landslide mass movements with particular emphasis on the material point method”. *Géotechnique* 68:457–458. <https://doi.org/10.1680/jgeot.16. d.004>.
52. Akbari, H. (2017) “Simulation of wave overtopping using an improved SPH method”. *Coast Eng* 126:51–68. <https://doi.org/10.1016/j.coastaleng.2017.04.010>
53. Ran, Q., Tong, J., Shao, S. et al (2015) “Advances in water resources incompressible SPH scour model for movable bed dam break flows”. *Adv Water Resour* 82:39–50. <https://doi.org/10.1016/j.advwatres.2015.04.009>
54. Ghaïtanellis, A., Violeau D, Ferrand M et al (2018) “A SPH elasticviscoplastic model for granular flows and bed-load transport”. *Adv Water Resour* 111:156–173. <https://doi.org/10.1016/j.advwatres.2017.11.007>.
55. Joseph, J., Monaghan and John C Lattanzio. (1985) “A refined particle method for astrophysical problems”. *Astronomy and astrophysics*, 149:135-143.
56. PAM System International. Pam-crash user manual version 2014. ESI Group,2014.
57. Wong, Jo Yung. (2008) “Theory of ground vehicles”. John Wiley & Sons.
58. El-Gindy, M., Lescoe, R., Öijer, F., Johansson, I. & Trivedi, M. (2011) “Soil Modelling Using FEA and SPH Techniques for a Tire-Soil Interaction”. ASME International Design Engineering Technical Conference, 28 August 2011.
59. Reese, L., Qiu, T., Linzell, D., & Rado, Z. (2016) “Field-Scale Testing and Numerical Investigation of Soil-Boulder Interaction under Vehicular Impact Using FEM and Coupled FEM-SPH Formulations”. Civil Engineering Faculty Publications, 7(1) 77–99.
60. Gheshlaghi, F., Mardani, A. & Mohebi, A. (2020a) “Investigating the effects of off-road vehicles on soil compaction using FEA-SPH simulation”. *Int. J. Heavy Vehicle Systems*, DOI: 10.1504/IJHVS.2020.10027405.
61. Gheshlaghi, F., and Mardani, A., (2021) “Prediction of soil vertical stress under off-road tire using smoothed-particle hydrodynamics”, *Journal of Terramechanics* 95 (2021) 7–14.

62. Aubel, T. (1993) "FEM simulation of the interaction between elastic tire and soft soil". In Proceedings, 11th International Conference of the ISTVS, Lake Tahoe, Nevada.
63. Fervers, C. W. (1994) "FE simulations of tire-profile effects on traction on soft soil". In Proceedings, 6th European Conference of the ISTVS, Vienna, Austria, 1994.
64. Fervers, C. W. (1997) "Effects of traction and slip, investigations with FEM". In Proceedings, 7th European Conference of the ISTVS, Ferrara, Italy.
65. Gentaro, H., Susan, F., A State, Chris, L., and Henry, F. (2001) "An implicit finite element method for elastic solids in contact". In Computer Animation, 2001. The Fourteenth Conference on Computer Animation. Proceedings, pages 136{254. IEEE, 2001.
66. Thiyahuddin, M.I., Yuan Tong Gu, RB Gover, and DP Thambiratnam. (2014) "Fluid-structure interaction analysis of full-scale vehicle-barrier impact using coupled sphfea". Engineering Analysis with Boundary Elements, 42:26-36.
67. Hermange, C., Oger, G. and Touzfe D. (2016) "Development of a coupling strategy between smoothed particle hydrodynamics and finite element method for violent fluid-structure interaction problems". In 3rd International Conference on Violent Flows 2016.
68. Aimin, Y., Jinze, L., Hengheng, Q., Yuhang, P., Yanhong, K., and Yuzhu, Z. (2016) "Numerical simulation of hypervelocity impact fem-sph algorithm based on large deformation of material".
69. Hallquist, J. Goudreau, G., and Benson, D. (1985) "Sliding interfaces with contact impact in large-scale lagrangian computations". Computer methods in applied mechanics and engineering, 51(1-3):107-137.
70. Onafeko, O. (1964) "Instrumentation for measuring radial and tangential stresses beneath rigid wheels". Journal of Terramechanics, 1(3):61-68.
71. Onafeko, O., and Reece, AR. (1967) "Soil stresses and deformations beneath rigid wheels". Journal of Terramechanics, 4(1):59-80.
72. Wong, Jo-Yung and Reece, AR. (1967) "Prediction of rigid wheel performance based on the analysis of soil-wheel stresses part I". performance of driven rigid wheels. Journal of Terramechanics, 4(1):81-98.
73. Wong, Jo-Yung and Reece, AR. (1967) "Prediction of rigid wheel performance based on the analysis of soil-wheel stresses: Part II". performance of towed rigid wheels. Journal of Terramechanics, 4(2):7-25.
74. Chu, Lok-Man and Yin, Jian-Hua. (2005) "Comparison of interface shear strength of soil nails measured by both direct shear box tests and pullout tests". Journal of geotechnical and geo-environmental engineering, 131(9):1097-1107.
75. Larry, D., Libersky, Albert G Petschek, Theodore C Carney, Jim R Hipp, and Firooz a Allahdadi. (1993) "High strain lagrangian hydrodynamics: a three-dimensional sph code for dynamic material response". Journal of computational physics, 109(1):67-75.

76. Shokouhfar, S., Rakheja, S., and El-Gindy, M. (2016a) "Development of a rolling truck tire model using an automatic model regeneration algorithm" International J. of Vehicle Systems Modelling and Testing, 11(1); 68-95.
77. Shokouhfar, S., Rakheja, S., and El-Gindy, M. (2016b) "Modal analysis of a rolling truck tire subjected to inflation pressure and vertical deflection" International J. of Vehicle Systems Modelling and Testing, 11(2):116.
78. Shokouhfar, S., Rakheja, S., and El-Gindy, M. (2015) "Verification of the Part-Composite Approach for modeling the multi-layered structure of a rolling truck tire" 10th European LS-DYNA Conference 2015, Würzburg, GermanyAt: Würzburg, Germany, DOI:10.13140/RG.2.1.2453.1048.
79. Shokouhfar, S., Rakheja, S., and El-Gindy, M. (2016c) "Development of a computationally efficient rolling truck tire model using part-composite approach and its verification" International J. of Vehicle Systems Modelling and Testing, 11(2):142. DOI: 10.1504/IJVSMT.2016.077929.
80. Lardner, K., (2017), "Prediction of the off-road rigid-ring model parameters for truck tire and soft soil interacions", MASc thesis, University of Ontario Tech.
81. Hiroma, T., Wanjii, S. Kataoka, T., and Ota, (1997), "Stress analysis using fem on stress distribution under a wheel considering friction with adhesion between a wheel and soil," Journal of Terramechanics, vol. 34, no. 4, pp. 255-233, October 1997.
82. Takayama, M., and Yamagishi, K., (1984), "Simulation Model of Tire Vibration," Tire Science and Technology, vol. 1, no. No. 1, pp. 38-49.
83. Loo, M., (1985), "A Model Analysis of Tire Behavior Under Vertical Loading and Straight-Line Free Rolling," Tire Science and Technology, vol. 13, no. 2, pp. 67-90.
84. Taheri, S., Sandu, C., Taheri, S., Pinto, E. and Gorsich, D. (2015) 'A technical survey on terramechanics models for tire-terrain interaction used in modeling and simulation of wheeled vehicles', J. Terramechanics, Vol. 57, pp.1–22, ISSN 0022-4898, pp.1–22.
85. Bekker, M.G. (1969) 'Part I: The terrain', 'Part II: The vehicle', Introduction to Terrain-Vehicle Systems, University of Michigan, Ann Arbor, Michigan.
86. Wakui F, Terumichi Y. (2011) "Numerical simulation of tire behavior on soft ground". J Syst Des Dyn 2011; 5(3): 486–500.
87. Nakajima, Y., and Padovan, J., (1986), "Numerical Simulation of Tire Sliding Events Involving Impacts with Holes and Bumps," Tire Science and Technology, Vol. 14, No. 2, pp. 125-136.
88. Chan, B.J., and Sandu, C., (2008), "A semi-analytical approach to off-road tire modeling for vehicle dynamics simulations" International Society for Terrain Vehicle Systems, January 2008.
89. MASTINU, G et al. (1997), "A Semi-Analytical Tyre Model for Steady- and Transient-State Simulations." Vehicle system dynamics 27.sup001 1997: 2–21. Web.
90. Xu, W., Zeng, H., Yang, P., and Zang, M. (2020), "Numerical analysis on tractive performance of off-road tire on gravel road using a calibrated finite element method–discrete element method model

- and experimental validation”, Proc IMechE Part D: J Automobile Engineering, Vol. 234(14) 3440–3457.
91. El-Gindy, M, Lescoe, R, O'ijer, F, Johansson, I, & Trivedi, M. (2011), "Soil Modeling Using FEA and SPH Techniques for a Tire-Soil Interaction." Proceedings of the ASME 2011 International Design Engineering Technical Conferences and Computers and Information in Engineering Conference. Washington, DC, USA. August 28–31, 2011. pp. 793-802. ASME.
 92. Dhillon, R, El-Gindy, M, Ali, R, Philippis, D, Öijer, F, & Johansson, I. (2013), "Sensitivity Analysis of Smoothed Particle Hydrodynamics in PAM-CRASH for Modeling of Soft Soils." Proceedings of the ASME 2013 International Design Engineering Technical Conferences and Computers and Information in Engineering Conference. USA. August 4–7, 2013. V001T01A015. ASME. <https://doi.org/10.1115/DETC2013-12024>.
 93. Kim, J.-T.; Im, D.-U; Choi, H.-J.; Oh, J.-W.; Park, Y.-J. (2021), “Development and Performance Evaluation of a Bevameter for Measuring Soil Strength”. Sensors 2021, 21, 1541.
 94. Syed, Z., Tekeste, M., and Way, T. (2017), “Discrete element modeling of cone penetration testing on soil with varying relative soil density”, 2017 ASABE Annual International Meeting Sponsored by ASABE Spokane, Washington, July 16-19, 2017.
 95. Jiang, M. J., H-S Yu, and D. Harris. (2006), "Discrete element modelling of deep penetration in granular soils." International Journal for Numerical and Analytical Methods in Geomechanics 30 (4):335-361.
 96. Bolton, M. D., and M. W. Gui. (1993), “The study of relative density and boundary effects for cone penetration tests in centrifuge”: University of Cambridge, Department of Engineering.
 97. Wong, J.Y, (2010). Terramechanics and Off-Road Vehicle Engineering, 2nd ed.; Butterworth-Heinemann: Oxford, UK.
 98. Okello, J.A., Watany, M., Crolla, D.A. (1998), “A theoretical and experimental investigation of rubber track performance models”, J. Agric. Eng. Res. 1998, 69, 15–24.
 99. Massah, J., Noorolahi, S. (2010), “Design, development and performance evaluation of a tractor-mounted bevameter”. Soil Tillage Res. 2010, 110, 161–166.
 100. Guo, M., Li, X., Ran, M., Z, X., and Yan, Y. (2020), “Analysis of contact stresses and rolling resistance of truck-bus tires under different working condition”, Sustainability 2020, 12, 10603; doi:10.3390/su122410603.
 101. Yong, R, Fattah, E. (1976) “Prediction of wheel–soil interaction and performance using the finite element method”. J Terramech; 13(4):227–40.
 102. Yong, R., Fattah E. and Boosinsuk, P. (1978), Analysis and Prediction of Tyre-Soil Interaction and Performance using Finite Elements, J. Terramechanics 15, 43-63
 103. Mashadi, B., Mousavi, H., and Montazeri, M. (2015) “Obtaining Relations between the Magic Formula Coefficients and Tire Physical Properties”, International Journal of Automotive Engineering; 5(1): 911-922.

- 104.Farhadi, P., Golmohammadi, A., Sharifi Malvajerdi, A., Shahgholi, G. (2019) ‘Finite element modeling of the interaction of a treaded tire with clay-loam soil’, Journal of Computers and Electronics in Agriculture; 162: 793-806.
- 105.Gaertig, T., Schack-Kirchner, H., Hildebrand, E.E., von Wilpert, K., (2002), “The impact of soil aeration on oak decline in southwestern Germany”, Forest Ecol. Manag.159, 15–25.
- 106.Pacejka, H.B., Bakker, E., 1992. The magic formula tyre model. Veh. Syst. Dyn. 21(001), 1–18.
- 107.Li H, Schindler C. Analysis of soil compaction and tire mobility with finite element method. Proc Inst Mech Eng K 2013.
- 108.Grujicic M et al. A finite element analysis of pneumatic-tire/sand interactions during off-road vehicle travel. Multi. Model. Mater. Struct. 2009;6(2):284–308.
- 109.Shoop SA. Finite element modeling of tire–terrain interaction. Hanover, NH: US Army Corps of Engineers; 2001.
- 110.Sandu, C. et al. (2019), “Hybrid Soft Soil Tire Model (HSSTM). Part II: Tire-terrain interaction, Journal of Terramechanics 86 (2019) 15–29
- 111.Gheshlaghi, F., El-Sayegh, Z., Sharifi, M., and El-Gindy, M. (2020), “Prediction and validation of tire rolling resistane coefficient, Int. J. Vehicle Systems Modelling and Testing, Vol. 14, No. 1, 2020.
- 112.W Gengenbach. (1968), “Expermantelle untersuchung von reifen auf nasser fahrbahn (experimental investigation of tires on wet tracks)”. Automobiltechnische Zeitschrift, Yol, 70:310-316, 1968.
- 113.El-Sayegh, Z., and El-Gindy, M., (2018), “Cornering characteristics of a truck tire on wet surface using finite element analysis and smoothed-particle hydrodynamics”, International Journal of Dynamics and Control (2018) 6:1567–1576
- 114.KA Grosch and G Maycock. (1968), “Inuence of test conditions on wet skid resistance of tire tread compounds”. Rubber Chemistry and Technology, 41(2):477-494, 1968.
- 115.Tonuk, E. Unlusoy, Y. S., (2001), “Prediction of Automobile Tire Cornering Force Characteristics by Finite Element Modeling and Analysis”, Computers and Structures.
- 116.G. S. Vorotovic, B. B. Rakicevic, S. R. Mitic and D. D. Stamenkovic. (2013), “Determination of Cornering Stiffness Through Integration of a Mathematical Model and Real Vehicle Exploitation Parameters”. FME Transactions, 41, 66-71, 2013.
- 117.Wei, C., Olatunbosun, O.A. (2016), “the effects of tire material and structure properties on relaxation length using finite element method” Materials and Design 102 (2016) 14–20.
- 118.Allen II, J., et al., (2007), “Predictions of tire-reeain interaction using finite element analysis models”, Proceedings of DETC’07, 2007 ASME International Design Engineering Technical Conference, September 4-7, 2007, Las Vegas, Nevada.

- 119.Kayacan, E., Kayacan, E., Ramon, H., and Saeys, W. (2014), "Nonlinear modeling and identification of an autonomous tractor–trailer System", Computers and Electronics in Agriculture 106 (2014) 1–10.
- 120.Hirschberg, W., Rill, G., Weinfurter, H. (2010), "User-appropriate tyre-modelling for vehicle dynamics in standard and limit situations". Veh. Sys. Dyn. 2010, 38, 103–12.
- 121.Bui, H.H., Sako, K. and Fukagawa, R. (2007), "Numerical simulation of soil–water interaction using smoothed particle hydrodynamics (sph) method", Journal of Terramechanics, Vol. 44, No. 5, pp.339–346.
- 122.P. S. Fancher. (1981), "Descriptive parameters used in analyzing the braking and handling of heavy trucks - measurements of the longitudinal and lateral traction properties of truck tires", data volume iii. Tech. Rep. UM-HSRI-81-19-3-4, University of Michigan, Highway Safety Research Institute, 1981.
- 123.Ragheb, H., El-Gindy, M., and Kishawy, H., (2013), "Development of a Combat Vehicle FEA Tire Model for Off-Road Applications," SAE Technical Paper 2013-01-0632, 2013, <https://doi.org/10.4271/2013-01-0632>.
- 124.El-Sayegh, Z. (2020), "Modeling and Analysis of Truck Tire-Terrain Interaction," Doctoral dissertation, 2020.
- 125.Chi Y., and GIM G.H., (2000), "Improved UA tire model as a semi-empirical model" 2000 FISITA World Automotive Congress At: Seoul, Korea.
- 126.Svendenius, J. and Gäfvert, M., (2004), "A Brush-Model Based Semi-Empirical Tire-Model for Combined Slips," SAE Technical Paper 2004-01-1064, 2004, <https://doi.org/10.4271/2004-01-1064>.
- 127.Tang S, Yuan S, Li X, Zhou J. (2020), "Dynamic modeling and experimental validation of skid-steered wheeled vehicles with low-pressure pneumatic tires on soft terrain". Proceedings of the Institution of Mechanical Engineers, Part D: Journal of Automobile Engineering. 2020;234(2-3):840-856. doi:10.1177/0954407019847302.
- 128.Carbonell, J., Monforte L., Ciantia M., et al, (2022), "Geotechnical particle finite element method for modeling of soil-structure interaction under large deformation conditions", Journal of Rock Mechanics and Geotechnical Engineering, 2022, ISSN 1674-7755.
- 129.Nirouman H., Mehrizi M., and Saaly M., (2016), "Application of mesh-free smoothed particle hydrodynamics (SPH) for study of soil behavior", July 2016, Geomechanics and Engineering 11(1):1-39.
- 130.Ivanov, V. (2010), "Analysis of Tire Contact Parameters Using Visual Processing", Advances in Tribology, vol. 2010, Article ID 491723, 11 pages, 2010. <https://doi.org/10.1155/2010/491723>.
- 131.Sabri M. and Abda S., (2018), "Grip Analysis of Road Surface and Tire Footprint Using FEM", IOP Conf. Ser.: Mater. Sci. Eng. 308 012018.

132. Loeb, J. S., Guenther, D. A. and Chen, H. F. (1990), "Lateral Stiffness, Cornering Stiffness and Relaxation Length of the Pneumatic Tire," SAE Paper 900129, February 1990.
133. Reid, A (2015), "Development and Optimization of a Wide Base FEA Truck Tire Model for Prediction of Tire-Road Interactions," University of Ontario Institute of Technology, Oshawa.
134. Cundall PA, Strack ODL. (1979), "A discrete numerical model for granular assemblies:", Geotechnique 29:47–65. <https://doi.org/10.1680/geot.1979.29.1.47>.
135. Bui HH, Fukagawa R, Sako K, Ohno S. (2008), "Lagrangian meshfree particles method (SPH) for large deformation and failure flows of geomaterial using elastic–plastic soil constitutive model". Int J Numer Anal Methods Geomech 32:1537–1570. <https://doi.org/10.1002/nag>.
136. Kaneda K., and Sawada T., (2019), "GRANULAR FLOW ANALYSIS CONSIDERING SOIL STRENGTH USING MOVING PARTICLE SIMULATION METHOD" VI International Conference on Particle-based Methods – Fundamentals and Applications PARTICLES 2019.
137. Rahman MA, Konagai K. (2017), "Substantiation of debris flow velocity from super-elevation: a numerical approach". Landslides 14:633–647. <https://doi.org/10.1007/s10346-016-0725-3>.
138. Gholami Korzani M, Galindo-Torres SA, Scheuermann A, Williams DJ. (2018), "SPH approach for simulating hydromechanical processes with large deformations and variable permeabilities". Acta Geotech 13:303–316. <https://doi.org/10.1007/s11440-017-0610-9>.
139. Zhao Lu, Zhuang Jin, Panagiotis Kotronis, (2021), "Numerical analysis of slope collapse using SPH and the SIMSAND critical state model", Journal of Rock Mechanics and Geotechnical Engineering, Volume 14, Issue 1, 2022, Pages 169-179, ISSN 1674-7755, <https://doi.org/10.1016/j.jrmge.2021.03.009>.
140. Ogbeche O., and Idowu M., (2016), "Design steps of narrow tillage tools for draught reduction and increased soil disruption-a review" March, 2016 AgricEngInt: CIGR Journal Open access at <http://www.cigrjournal.org> Vol. 18, No. 1 P: 91-102.
141. Collings, W., El-Sayegh, Z., and El-Gindy, M. (2021), "Phase XIX Task 3 Progress Report: Development of terramechanics mud characteristics for tire-terrain interaction", Volvo Group Trucks Technology, Göteborg, Sweden, XVIII-1, Aug. 30 2021.
142. Contreras, U. Li, G., Foster, C.D. Shabana, A.A. Jayakumar, P. and Letherwood, M.D., (2013), "Soil Models and Vehicle System Dynamics", Applied Mechanics Reviews, vol. 65, 040802-1.
143. El-Razaz, A., (1988), "Lateral tire forces on off-road surfaces" PhD thesis, September 1988.
144. Brantin, A., (2016), "Implementation of the Rigid Ring Tyre Model and Accompanying Soil Model in a Complete Vehicle Simulation Tool for Trucks" Master's Thesis, 2016.
145. Shakiba, M., Ozer, H., Ziyadi, M. et al. (2016), "Mechanics based model for predicting structure-induced rolling resistance (SRR) of the tire-pavement system", Mech Time-Depend Mater 20, 579–600 (2016).

- 146.Suyabodha, Apiwat; Abdul Amir, H.F , Khiew, P.S, (2017), "A Relationship between Tyre Pressure and Rolling Resistance Force under Different Vehicle Speed" MATEC web of conferences, 2017, Vol.108, p.12004.
- 147.Jiang k, Pavelescu A, Victorino A, Charara A. (2014), "Estimation of vehicle's vertical and lateral tire forces considering road angle and road irregularity", 17th International IEEE Conference on Intelligent Transportation Systems (ITSC 2014), Oct 2014, Qingdao, China. pp.342-347, 10.1109/ITSC.2014.6957714.
- 148.Schwanghart, H. (1981), "Measurements of forces on steered towed wheels". Proc. of the 7th Int. Conf. I. S. T. V. S. Calgary, Vol. 1, pp (335-356).
- 149.Longhouser, J.E. (1972), "Investigation of the cornering dynamics of a military tire". Tech. Rep. SIT-DL-72-1609, Davidson Lab, Stevens Institute of Technology, Hoboken, New Jersey, 1972.